A capacitive RF power sensor based on MEMS technology

Luis J. Fernandez

The research described in this thesis was carried out at the Transducers Science and Technology Group of the MESA$^+$ institute for nanotechnology, University of Twente, The Netherlands. It was performed within the framework of the IST European project 'Electro Mechanical Microcomponents for precision Applications' (EMMA, IST-2000-28261).

Promotiecommissie

Voorzitter:	prof.dr.ir. A.J. Mouthaan	
Secretaris:	prof.dr.ir. A.J. Mouthaan	Univ. Twente, EWI
Promotor:	prof.dr. M.C. Elwenspoek	Univ. Twente, EWI
Assistent promotor:	dr.ir. R.J. Wiegerink	Univ. Twente, EWI
Referent:	dr. H. Tilmans	IMEC Leuven
Leden:	prof.dr.ir B. Nauta	Univ. Twente, EWI
	prof. J.L. Tauritz	Univ. Twente, EWI
	prof. R. Puers	KU Leuven
	prof.dr J. Schmitz	Univ. Twente, EWI
	dr.ir. J. Flokstra	Univ. Twente, EWI

Fernandez, Luis J.
A capacitive RF power sensor based on MEMS technology
Ph.D. Thesis, University of Twente, Enschede, The Netherlands

ISBN 90-365-2294-3

Print: Wöhrmann Print Service, Zutphen, The Netherlands

A CAPACITIVE RF POWER SENSOR BASED ON MEMS TECHNOLOGY

DISSERTATION

to obtain
the doctor's degree at the University of Twente,
on the authority of the rector magnificus,
prof. dr. W.H.M. Zijm
on account of the decision of the graduation committee,
to be publicly defended
on Wednesday December 14, 2005 at 13:15

by

Luis Jose Fernandez

born on March 20, 1977
in Zaragoza, Spain

This dissertation has been approved by:

Prof. dr. M.C. Elwenspoek	Promotor
Dr.ir. R.J. Wiegerink	Assistant Promotor

Para Marta,

Contents

Chapter 1

General introduction

1.1 Introduction

Measuring radio frequency (RF) power is an important technique in many applications, ranging from wireless personal communication systems, to radar and satellite communications [1]. Especially telecommunication systems require a low weight, volume and power consumption and a high level of integration with electronics. It is expected that RF MEMS devices will be able to improve these characteristics. Up to now, RF power sensing is done mainly by thermistors, diodes and thermocouples [2-3]. These power sensors are used as terminating devices and therefore they dissipate the complete incoming signal. The research presented in this thesis is focused on exploring a new philosophy to sense in-line RF power in a way that the signal is not lost during RF operation: the 'through' mode of sensing. Such a 'through sensor' was first proposed by Seppä [4] and the realization of such a sensor was one of the aims of the EU project EMMA (Electro Mechanical Microcomponents for precision Applications) [5]. The research which resulted in this thesis was performed in the context of this project.

1.2 State of the art of RF power sensors

Basically an RF power sensor needs to convert microwave power into a quantity which is easy to measure. Nowadays, three different kinds of RF power sensors are usually distinguished:

a) Thermistors
b) Thermocouples
c) Diodes

Thermistors

Thermistors are used in the field of RF sensors in a way similar to bolometers. That is, the RF signal is converted into heat by dissipating it in a resistor and the resulting change of temperature is measured. The electrical resistance of a thermistor is directly dependent on temperature and therefore a thermistor can be used both as the dissipating resistor and as temperature sensor. In fact, the RF power is converted into a change of electrical resistance, which is much easier to measure.

In RF power measurement applications, a thermistor consists of an element with a semi-conductor behavior (often a metallic oxide), with a negative temperature resistivity coefficient, a = (1/R)(dR/dT), is negative. In order to obtain an accurate measurement, a very good matching between the transmission line (which carries the RF signal) and the absorbing load is needed, since all the power has to be dissipated in the load.

However, thermistor characteristics of resistance as a function of power are highly non-linear, and vary considerably from one thermistor to another. To solve this problem, DC or AC low frequency bias is used to maintain the resistance of the thermistor constant. As RF power is dissipated in the thermistor, tending to lower R, the bias power is withdrawn by an equal amount to keep R at the same value. The required decrease in bias power is exactly the same as the dissipated RF power.

Nowadays, companies like EMC Technology Inc., Gigatronics or Dorado International Corporation offer a variety of RF power sensors based on thermistors. Their frequency range may extend from 200 MHz to 6 GHz, and the dynamic range from -10 dBm to +30 dBm.

Thermocouples

The operation principle of the thermocouples is based on the Seebeck effect: a voltage appears when there is a temperature gradient in a closed circuit created by different metals.

A simple way to explain the physics involved is illustrated by Figure 1. This figure shows a long metal rod that is heated at the left end. As a consequence of the heat, many electrons get enough energy to become free from the atoms to which they belong. The resulting increased density of free electrons at the left causes diffusion

towards the right, while positive charges are fixed since they are locked into the metallic structure. However, the positive charges created at the left side of the rod attract the migrated electrons. Equilibrium is reached when these two opposite forces are in balance. As a result, an electric field is created in the metal, which gives a voltage difference called Thomson electromotive force (emf).

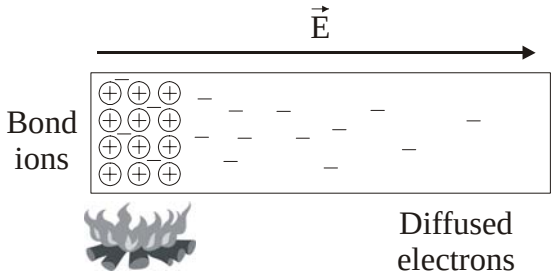

Figure 1: Illustration of the Thomson effect on metals.

The same principle can be applied at the junction of different metals with different free electron densities. The name of this phenomenon is the Peltier effect. Figure 2 illustrates a typical thermocouple created by the junction of two different metals. As can be observed, by placing a voltmeter at the cold side of the metals, the Thomson emf (V_1, V_2) and Peltier emf (V_h) effects are used to produce the net thermoelectric voltage (V). The total effect is also known as the Seebeck emf.

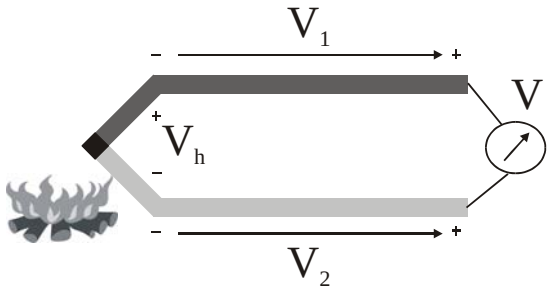

Figure 2: Illustration of the Seebeck effect used in thermocouple based RF power sensors.

There are many commercially available thermocouple-based RF power sensors (Agilent, Anritsu Ltd., Boonton Electronics Corporation, Oritel, Dorado International Corporation, Gigatronics, Rohde & Schwarz, etc.). Thermocouple RF power sensors have a wider dynamic range than thermistors, typically from -30 dBm to +20 dBm, and their frequency range may extend up to 20 GHz.

Diodes

Diodes can be used for direct RF power detection when they are operated in their square law region [2]. In this way, the DC voltage obtained is simply proportional to the RF power level of the signal. Of course we have to use a special RF diode

that is fast enough, has very little capacitance and is housed in a very small package to keep the series inductance as small as possible. For that reason, Schottky diodes are used exclusively as RF power sensors.
For a typical packaged diode, the square-law detection region exists from the noise level (typically -70 dBm) up to approximately -20 dBm. For measuring up to +20 dBm, two solutions are proposed. The first one consists of placing an attenuatior before the diode. Nevertheless, this reduces the accuracy of the measurement. The second one is based on correcting the measured signal by calibrating the diode and using digital signal processing circuitry. However, this results in a very complex and expensive device. The frequency range of diode RF power sensors can be from 10 MHz up to 18 GHz.
Diodes are the most widely used commercially available RF power sensors. Some examples are Agilent, Anritsu Ltd., Boonton Electronics Corporation, Oritel, Dorado International Corporation, Gigatronics, Rohde & Schwarz, or Wandel & Goltermann.

1.3 Motivation

As mentioned before, detecting radio frequency (RF) power is an important technique in many applications, ranging from wireless personal communication systems, to radar and satellite communications [1]. Although various techniques as presented in the previous section are available, it is expected that a MEMS device could result in a smaller sensor with lower weight, lower power consumption and much lower RF losses. In fact, the thermistors, thermocouples and diodes discussed in the previous section are basically terminating devices, i.e. the sensed RF power is completely dissipated in the sensor. The only way to realize a ‘through’ sensor with these devices is to use a power splitter and feed a certain fraction of the total signal power to the sensor. Nevertheless, not only part of the signal is inevitably lost, but frequency range and insertion loss of the complete system is heavily limited by the splitter performance. The MEMS power sensors presented in this thesis are based on a completely different measurement principle, namely the measurement of the attractive force between the two plates of a charged capacitor, where one of the plates is moveable. When a voltage difference is applied to the plates, the electrostatic force will pull the moveable plate towards the fixed plate. When an ac voltage is applied, this will result in a time dependent, but always attractive, electrical force. For frequencies well above the mechanical resonance frequency, only the average force is important, which is proportional to the square of the rms voltage amplitude. Thus, by sensing the displacement of the moveable capacitor plate or by sensing the force needed to keep the plate in its initial position, the square of the rms voltage amplitude of the ac signal can be obtained. Using this measurement principle a true ‘through’ sensor can be realized with very low RF losses. The principle has already been exploited to realize

micromechanical rms-to-dc converters [6–9], however no attempt was made to exploit the principle for signals in the GHz range. In this case, the sensor design becomes more challenging, because one of the capacitor electrodes has to be inserted in a high-frequency transmission line, and careful study of the RF signal response is needed since changes in the impedance of the line will result in reflection losses. Furthermore, the currents running in the transmission line will introduce an extra magnetic force, which opposes the electric force[1].

1.4 Technological challenges and scientific questions

It is very important to understand how the RF signal is affected by the insertion of the capacitive sensor itself. Furthermore, a careful study of the RF signal behavior is needed in order to create a place on the transmission line where the magnetic force doesn't oppose the electric force without inducing relevant mismatch losses.

The realization of a capacitive power sensor for RF signals with negligible insertion losses represents a challenge from the design point of view. On one hand, the capacitance introduced by the sensor should be as small as possible in order to minimize the impedance on the transmission line and minimize reflection losses. But on the other hand, the sensitivity of the sensor is directly proportional to the capacitance value introduced by the sensor. Therefore, a careful study of the sensor design is needed in order to try to solve the trade off between sensitivity and bandwidth.

We will see how RF dedicated glass wafers will be required in order to minimize insertion losses and meet the specifications required by the EMMA project (Apendix A). Therefore, a fabrication process based on surface micromachining is needed where low spring constant movable capacitors should be possible to realize with the use of no high temperature steps.

In order to reach the sensitivity requirements mentioned by the EMMA project (Apendix A), special care needs to be taken with respect to the capacitive read out electronics. The optimum situation corresponds to the case where CMOS electronics are place next to the sensor. Nevertheless, this is totally unpractical due to the enormous amount of losses introduced by CMOS substrate. The possibility of transform a CMOS wafer into a suitable substrate for RF signals will not only optimize the capacitive read-out by CMOS, but also would allow the use of high temperature steps during the fabrication of the sensor.

[1] In fact, as will be explained in Section 2.2.4, some losses are inevitable since in a perfect lossless transmission line the electric force is exactly compensated by the magnetic force and there is no net resulting force that can be measured.

1.5 Thesis outline

The research results obtained in this thesis are presented in 7 chapters. The basic theory for RF signals is presented at the beginning of Chapter 2. Then, the analysis of the forces and the force balance in a transmission line are studied. The operation principle and basic design for a capacitive RF MEMS power sensor are then presented. The presence of inevitable trade-off between sensitivity and bandwidth is discussed, and a solution to release such a trade-off based on the redesign of the transmission line proposed. Finally, the study of theoretical limitations of the sensor results in an ultimate RF power resolution level in the order of nanoWatt.

In Chapter 3, the design of the transmission line used as support for the RF signal is presented and discussed. Furthermore, two different RF power sensor designs based on the fabrication of a free standing 'bridge' on top of the transmission line (grounded and floating bridge) are proposed in this chapter. The theoretical frequency performance of the different RF power sensors are calculated by modeling the sensor to a shunt capacitor. Results show that a power sensor which introduces less than 80 fF to the transmission line should fulfill the target specifications up to 4 GHz requested by the EMMA project (Apendix A). The sensitivity of the RF power sensors are calculated by estimating the spring constant of the 'bridge'. A strong dependence between stress on the structural layer of the 'bridge' and sensitivity of the sensor is observed.

Chapter 4 will show in detail the different fabrication flows used for the realization of the two different RF MEMS power sensors presented in chapter 3 (grounded and floating bridge). Aluminum surface micromachining on top of a glass substrate with photoresist as a sacrificial layer is used for the fabrication of the sensors. Aluminum was chosen because of its good electrical and mechanical properties since very small displacements are required (nm range), RF dedicated glass substrates because of their good RF performance, and photoresist because of its round edges ensuring mechanical stability of the aluminum 'bridge'. Successful fabrication results of 300 μm long grounded 'bridge' power sensors are reported. Nevertheless, a pattern is observed on the 'bridge' due to the presence of the transmission lines underneath. This pattern could cause physical connection between the bridge and the transmission line for longer 'bridge' dimensions. Therefore, a new fabrication flow, where the transmission lines are embedded into the substrate, is used for the fabrication of the 'floating' bridge power sensors. The successful fabrication of very flat (within 200 nm) and 900 μm long 'bridges' is reported.

In Chapter 5, the measurement results obtained on the different RF MEMS power sensors are presented and discussed. Measurement of the S-parameters for the

grounded ‘bridge’ sensors reveal a very good agreement with respect to the expected behavior presented in chapter 3. For the case of the floating ‘bridge’, lower gap between the ‘bridge’ and the transmission line is observed (600 nm), resulting in higher reflection losses than expected. Nevertheless, measurement obtained from the sensors where the transmission line was redesigned in order to increase the bandwidth resulted on an improvement of the RF performance. As a result, very successful reflection (<-30 dB) and insertion losses (<0.14 dB) are obtained up to 4 GHz. The power detection of an RF signal using a capacitive MEMS sensor is reported for the first time. Sensitivity in agreement with the expectations presented in chapter 3 is found, being 100.5 fF/Watt for the 3600x300 μm grounded sensor, and 91.48 and 180.58 fF/W for the 110x900 and 220x900 μm floating sensor respectively. As expected, the floating sensors resulted in a better resolution (mWatt).

In Chapter 6, a new process technology which allows the fabrication of an RF MEMS sensor on low-resistivity silicon wafers without the high losses associated with such a substrate is presented. It consists in the local replacement of the silicon substrate by silicon-rich silicon nitride (SiRN), which has very good RF properties. It is realized by the etching of deep trenches on the substrate and refilling these trenches by LPCVD SiRN. As a result, alternating plates of SiRN and monocrystalline Si are obtained. Improvement of the RF performance was obtained by increasing the SiRN plate width, and varying orientation of the plates. As a result, 0.7 dB/mm insertion loss is measured at 4 GHz on a 1 μm thick transmission line placed on top, which represent a large improvement in comparison to the 3.5 dB/mm measured for the case of low-resistivity silicon substrate. A complete replacement of the silicon substrate can be realized by etching the remaining silicon in between the SiRN plates, and refilling the cavities with LPCVD SiRN. S-parameters measurements report further improvement of the RF characteristics (0.2 dB/mm at 4 GHz), reaching very similar performances to dedicated glass substrates (0.1 dB/mm at 4 GHz).

Chapter 7 presents general conclusions and gives recommendations for future work.

1.6 References

[1] Harrie A C Tilmans, Walter De Raedt and Eric Beyne.: “MEMS for wireless communications: ‘from RF-MEMS components to RF-MEMS-SiP’“, *J. Micromech. Microeng.* 13 (2003) S139–S163.

[2] Daulle A., Xavier P., Rauly D.: "A power sensor for fast measurement of telecommunications signals using substitution method", *IEEE Transactions on Instrumentation and Measurement*, Volume: 50 Issue: 5 , Oct.2001, pp. 1190 –1196.

[3] Hewlett-Packard, “Fundamentals of RF and microwave power measurements”, Application note 64-1, 2001.

[4] Seppä H., Kyynäräinen J., Oja A.: "Microelectromechanical systems in electrical metrology", *IEEE Transactions on Instrumentation and Measurement*, Volume: 50 Issue: 2 , April 2001, pp. 440-444.

[5] http://www.vtt.fi/tte/research/tte7/research/emma/index.html.

[6] B. P. Drieënhuizen and R. F. Woffenbuttel, “Integrated electrostatic true RMS-to-DC converter”, *IEEE Transactions on Instrumentation and Measurement*, 44, 1995, pp. 370-373.

[7] M. Suhonen, H. Seppä, A.S. Oja, M. Heinilä and I. Näkki, "AC and DC Voltage Standards Based on Silicon Micromechanics", *Proceedings CPEM*, Washington DC, 1998, pp. 23-24.

[8] M. Bartek, Z. Xiao, C. van Mullem and R.F. Wolffenbuttel, “Bulk-micromachined electrostatic RMS-to-DC converter: Design and fabrication”, *Proceedings MME*, Uppsala, Sweden, October 1-3, 2000.

[9] J. Kyynäräinen, A.S. Oja and H. Seppä, “A Micromechanical RMS-to-DC Converter”, *Proceedings CPEM*, Sydney, 2000, pp. 699-700.

Chapter 2

Theory and operating principle

2.1 Introduction

In this chapter, all basic theory involved in the realization of an RF power sensor based on MEMS will be presented. First, the theory needed to deduce and define the most relevant phenomena and parameters which describe an electromagnetic wave traveling through a transmission line will be introduced. This theory can also be found in many textbooks (e.g. [1]) and it is summarized here for those who are not familiar with RF design. Readers familiar with the theory of electrodynamics and transmission lines may want to go directly to Section 2.2.2, where the forces present on a matched transmission line are discussed. Next, in Section 2.3 the basic structure and operation principle of an RF-MEMS power sensor will be presented. In this way, all theoretical aspects and limitations regarding the development of an RF power sensor based on MEMS technology are covered.

2.2 Electromagnetic wave on a transmission line

2.2.1 Basic theory

We can define a high frequency transmission line as the path design to carry electromagnetic waves whose wavelengths are shorter or comparable to the length of the line. In order to introduce the transmission line concept lets consider an electromagnetic wave propagating in the *z*-direction and having an *x*-component only of the electric field and a *y*-component only of the magnetic field, which is

$$\begin{aligned} \vec{E} &= E_x(z,t)\hat{x} \\ \vec{H} &= H_y(z,t)\hat{y} \end{aligned} \qquad (1)$$

between two parallel, perfect conductors as shown in Figure 2.1.

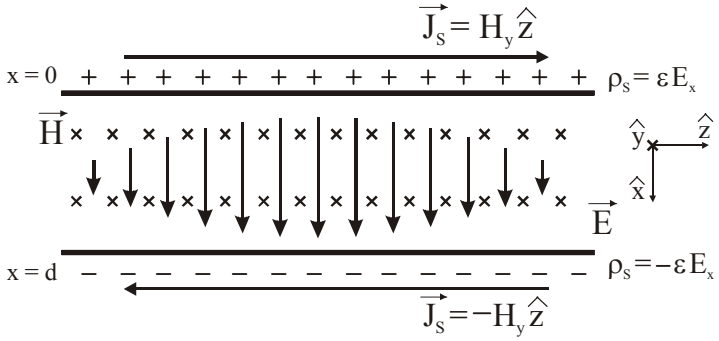

Figure 2.1: Uniform plane electromagnetic wave propagating between two perfectly conducting sheets supported by charges and current on the sheets.

Since the conducting sheets are made of perfect conductors, the electric field is completely normal and the magnetic field is completely tangential to the sheets, and the wave will propagate as if the sheets were not present, being guided by the sheets. We now have a simple example of a transmission line, namely the parallel-plate transmission line. Let's assume that the medium between the plates is a perfect dielectric so that the waves propagate without attenuation and the line is lossless.
Because of the presence of the traveling electromagnetic waves, charges and currents are induced at the surface of the conductors. The charge densities, ρ_s, on the two plates can be calculated applying boundary conditions, resulting:

$$\begin{aligned} [\rho_S]_{x=0} &= \left[\hat{n}\cdot\vec{D}\right]_{x=0} = \hat{x}\cdot\varepsilon E_x\,\hat{x} = \varepsilon E_x \\ [\rho_S]_{x=d} &= \left[\hat{n}\cdot\vec{D}\right]_{x=d} = -\hat{x}\cdot\varepsilon E_x\,\hat{x} = -\varepsilon E_x \end{aligned} \qquad (2)$$

where ε is the permittivity of the medium between the two plates, and $\hat{n}$ is a unitary vector normal to the metal sheets surface. In the same way, the current densities on the two plates can be expressed as:

$$\begin{aligned} [J_S]_{x=0} &= \left[\hat{n} \times \vec{H}\right]_{x=0} = \hat{x} \times H_y \, \hat{y} = H_y \, \hat{z} \\ [J_S]_{x=d} &= \left[\hat{n} \times \vec{H}\right]_{x=d} = -\hat{x} \times H_y \, \hat{y} = -H_y \, \hat{z} \end{aligned} \qquad (3)$$

The charge and current densities are functions of *z* and *t*, as are E_x and H_y. Thus, the wave propagation along the transmission line is supported by charges and currents on the plates, varying with time and distance along the line.
Let's consider now finitely sized plates having width *w* in the *y*-direction, as shown in Figure 2.2(a), and neglect fringing of the fields at the edges or assume that the structure is part of a much larger-sized configuration.

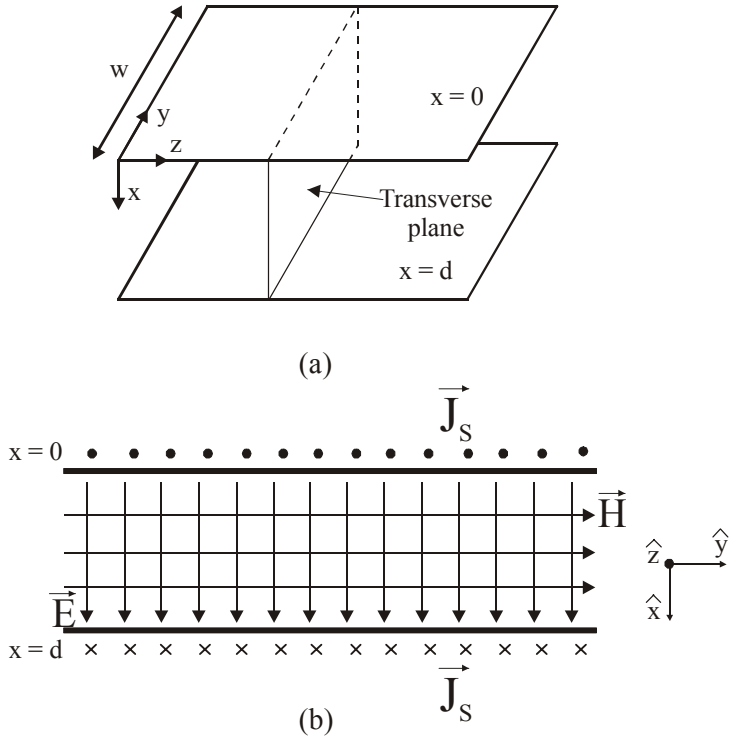

Figure 2.2: (a) Parallel-plate transmission line (b) Transverse plane of the parallel-plate transmission line

By considering a constant-*z* plane, that is, a plane transverse to the direction of propagation of the wave, as shown in figure 2.2(b), we can find the voltage between the two conductors in terms of the line integral of the electric field intensity evaluated along any path in that plane between the two conductors. Since

the electric field is directed in the *x*-direction and since it is uniform in that plane, this voltage is given by

$$V(z,t) = \int_{x=0}^{d} E_x(z,t)\,dx = E_x(z,t)\int_{x=0}^{d} dx = d\,E_x(z,t)\,. \tag{4}$$

Thus, each transverse plane is characterized by a voltage between the two conductors, which is related simply to the electric field, as given by (4). Each transverse plane is also characterized by a current I flowing in the positive z-direction on the upper conductor and in the negative z-direction on the lower conductor. From Figure 2.2(b), and using equation (3), we can deduce that this current is given by

$$I(z,t) = \int_{y=0}^{w} J_S(z,t)\,dy = \int_{y=0}^{w} H_y(z,t)\,dy = H_y(z,t)\int_{y=0}^{w} dy = w\,H_y(z,t)\,, \tag{5}$$

since H_y is uniform in the cross-sectional plane. Thus, the current crossing a given transverse plane is related simply to the magnetic field in that plane, as given by (5).
Proceeding further, we can find the power flow down the line by evaluating the surface integral of the Pointing vector over a given transverse plane. Thus,

$$\begin{aligned} P(z.t) &= \int_{\substack{transverse\\plane}} (\vec{E}\times\vec{H})\cdot d\vec{S} = \int_{x=0}^{d}\int_{y=0}^{w} E_x(z,t)H_y(z,t)\hat{z}\cdot dx\,dy\,\hat{z} = \\ &= \int_{x=0}^{d}\int_{y=0}^{w} \frac{V(z,t)}{d}\frac{I(z,t)}{w}\,dx\,dy = V(z,t)I(z,t) \end{aligned} \tag{6}$$

which is the familiar relationship employed in circuit theory.

Lossless transmission line equations

Using the two curl Maxwell equations for the case of $\vec{E}$ and $\vec{B}$ expressed as equation (1), we can arrive to the following two differential equations

$$\frac{\partial E_x}{\partial x} = -\frac{\partial B_y}{\partial t} = -\mu\frac{\partial H_y}{\partial t} \tag{7.a}$$

$$\frac{\partial H_y}{\partial z} = -\sigma E_x - \varepsilon\frac{\partial E_x}{\partial t} = -\varepsilon\frac{\partial E_x}{\partial t} \tag{7.b}$$

where we have assumed a perfect dielectric medium, that is, $\sigma = 0$. Making now use of equations (4) and (5) in (7.a) and (7.b) respectively, we obtain two differential equations for voltage and current along the line

$$\frac{\partial V}{\partial z} = -\left(\frac{\mu d}{w}\right)\frac{\partial I}{\partial t}, \qquad (8.a)$$

$$\frac{\partial I}{\partial z} = -\left(\frac{\varepsilon w}{d}\right)\frac{\partial V}{\partial t}. \qquad (8.b)$$

These equations are known as the transmission-line equations. Making use of equations (8.a) and (8.b), we can characterize the propagation of a microwave along the line in terms of voltage and current.
Equation (8) can be further simplified by introducing the inductance L and capacitance C per unit length of the transmission line in the z-direction. The inductance per unit length is defined as the ratio between the magnetic flux per unit length at any value of z and the line current at that value of z, having the unit Henry per meter (H/m). From Figure 2.2 we can easily see that the magnetic flux per unit length is given by $\mu H_y d$. Since the current is given by $H_y w$ (equation (5)) we have:

$$L = \frac{\mu H_y d}{H_y w} = \frac{\mu d}{w}. \qquad (9)$$

The capacitance per unit length is defined as the ratio between the amount of charge per unit length on either plate at any value of z and the line voltage at that value of z, having the unit Farad per meter (F/m). The charge per unit length is $\rho_s w$, or $\varepsilon E_x w$, and the voltage is $E_x d$ (equation (4)), so we find for the capacitance per unit length:

$$C = \frac{\varepsilon E_x w}{E_x d} = \frac{\varepsilon w}{d} \qquad (10)$$

Both L and C are purely dependent on the dimensions of the line and independent of E_x and H_y. Furthermore, we see that

$$LC = \mu\varepsilon \qquad (11)$$

Thus, only one of the two parameters L and C is independent and the other can be obtained from the knowledge of ε and μ.
Inserting (9) and (10) in (8) gives the transmission line equations in terms of L and C:

$$\frac{\partial V}{\partial z} = -L\frac{\partial I}{\partial t} \qquad (12.a)$$

$$\frac{\partial I}{\partial z} = -C\frac{\partial V}{\partial t} \qquad (12.b)$$

Using these equations we can discuss wave propagation along the line in terms of circuit quantities instead of in terms of field quantities.

Lumped element equivalent

A transmission line is often represented by its circuit equivalent that can be derived from the transmission line equations (12.a) and (12.b). To do this, we consider a section of infinitesimal length Δz along the line between z and $z + \Delta z$. From (12.a), we find

$$\lim_{\Delta z \to 0} \frac{V(z+\Delta z,t) - V(z,t)}{\Delta z} = -L\frac{\partial I(z,t)}{\partial t} \qquad (13)$$

when $\Delta z \to 0$ we have

$$V(z+\Delta z,t) - V(z,t) = -L\,\Delta z\frac{\partial I(z,t)}{\partial t} \qquad (14.a)$$

This equation can be represented by the circuit equivalent shown in Figure 2.3(a), since it satisfies Kirchhoff's voltage law written around the loop abcda. Similarly, from (12.b) we find

$$\lim_{\Delta z \to 0} \frac{I(z+\Delta z,t) - I(z,t)}{\Delta z} = \lim_{\Delta z \to 0}\left[-C\frac{\partial V(z+\Delta z,t)}{\partial t}\right]$$

when $\Delta z \to 0$ we have

$$I(z+\Delta z,t) - I(z,t) = -C\,\Delta z\frac{\partial V(z+\Delta z,t)}{\partial t} \qquad (14.b)$$

This equation can be represented by the circuit equivalent shown in Figure 2.3(b), since it satisfies Kirchhoff's current law written for node c. Combining the two equations, we obtain the equivalent circuit shown in Figure 2.3(c) for a section Δz of the line.

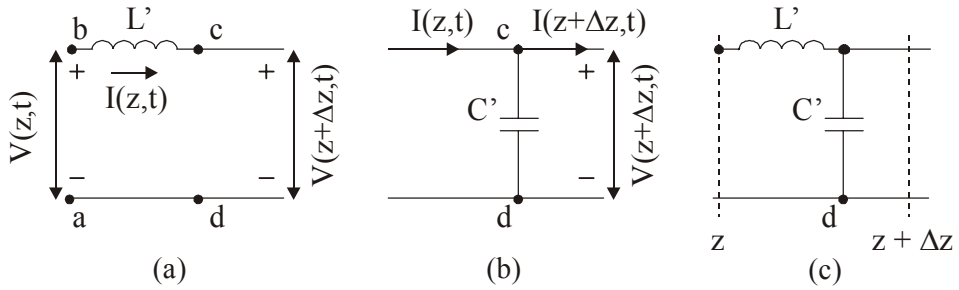

Figure 2.3: Development of circuit equivalent for an infinitesimal length Δz of a transmission line

L' and C' represent the inductance and capacitance for a section Δz of the line. It then follows that the circuit representation for a portion of length *l* of the line consists of an infinite number of such sections in cascade, as shown in Figure 2.4.

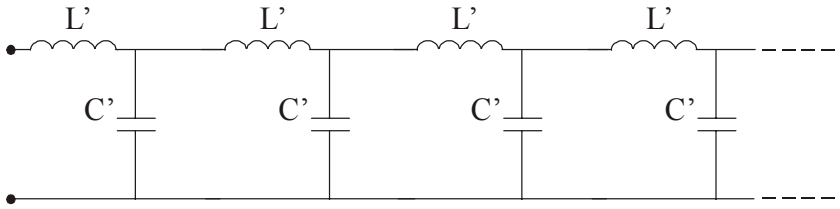

Figure 2.4: Distributed circuit representation of a transmission line

We can also calculate the energy stored in the electric and magnetic field for each section Δz of the line as a function of L' and C'.

$$W_e = \frac{1}{2}\varepsilon E_x^2 (d\, w\, \Delta z) = \frac{1}{2}\frac{\varepsilon w}{d}\left(E_x d\right)^2 \Delta z = \frac{1}{2} C\, \Delta z V^2 = \frac{1}{2} C' V^2 \qquad (15.a)$$

$$W_m = \frac{1}{2}\mu H_y^2 (d\, w\, \Delta z) = \frac{1}{2}\frac{\mu d}{w}\left(H_y w\right)^2 \Delta z = \frac{1}{2} L\, \Delta z\, I^2 = \frac{1}{2} L' I^2 \qquad (15.b)$$

From equations (15.a) and (15.b) we can conclude that L' and C' are elements associated with energy storage in the magnetic field and energy storage in the electric field, respectively.

Most relevant parameters in a lossless transmission line

We will use now the theory explained in the previous sections in order to deduce the most relevant parameters for the characterization of a radio frequency wave traveling on a transmission line.

- ***Characteristic impedance***

We can write the voltage and current in a phasor form as follows:

$$v(z,t) = \mathrm{Re}\left[V(z)\, e^{j\omega t}\right] \qquad (16.a)$$
$$i(z,t) = \mathrm{Re}\left[I(z)\, e^{j\omega t}\right] \qquad (16.b)$$

Inserting (16) in (12) gives:

$$-\frac{dV(z)}{dz} = j\,\omega L\, I(z) \qquad (17.a)$$
$$-\frac{dI(z)}{dz} = j\,\omega C V(z) \qquad (17.b)$$

Combining these two equations we obtain the wave equation for $V(z)$:

$$-\frac{d^2V(z)}{dz^2} - \gamma^2 V(z) = 0 \qquad (18)$$

where γ is called the complex propagation constant of the transmission line and can be expressed as:

$$\gamma = \sqrt{-\omega^2 L C} = j\,\omega\sqrt{LC} \qquad (19)$$

Similarly we can obtain the wave equation for $I(z)$:

$$\frac{d^2I(z)}{dz^2} - \gamma^2\, I(z) = 0 \qquad (20)$$

Solving equations (18) and (20), we arrive to the traveling wave solutions of the following form:

$$V(z) = V_0^+ e^{-\gamma z} + V_0^- e^{\gamma z} \qquad (21.a)$$
$$I(z) = I_0^+ e^{-\gamma z} + I_0^- e^{\gamma z} \qquad (21.b)$$

where the $e^{-\gamma z}$ term represents wave propagation in the +z-direction and the $e^{\gamma z}$ term represents wave propagation in the –z-direction. The solutions presented in (21.a) and (21.b) contain four unknown quantities, which are the wave amplitudes of the +z propagating wave (V_0^+, I_0^+) and the –z propagating wave (V_0^-, I_0^-). We can easily relate the current wave amplitudes, I_0^+ and I_0^-, to the voltage wave amplitudes, V_0^+ and V_0^-, by inserting (21.a) in (17.a) and then solving for the current $I(z)$ to get:

$$I(z) = \frac{\gamma}{j\,\omega\,L}\left[V_0^+ e^{-\gamma z} - V_0^- e^{\gamma z}\right]. \tag{22}$$

Comparison of each term with the corresponding term in (21.b) leads to the conclusion that

$$\frac{V_0^+}{I_0^+} = Z_0 = \frac{-V_0^-}{I_0^-} \tag{23}$$

where

$$Z_0 = \frac{j\,\omega\,L}{\gamma} = \sqrt{\frac{L}{C}} \tag{24}$$

is defined as the characteristic impedance of the line.

- ***Phase velocity***

Since V_0^+ and V_0^- are complex magnitudes, we can express them using their magnitude and phase as shown in (25.a) and (25.b).

$$V_0^+ = \left|V_0^+\right| e^{j\Phi^+} \tag{25.a}$$

$$V_0^- = \left|V_0^-\right| e^{j\Phi^-} \tag{25.b}$$

We can now introduce them into (21.a), obtaining:

$$\begin{aligned} v(z,t) &= \mathrm{Re}(V(z)\,e^{j\omega t}) = \mathrm{Re}\left[(V_0^+\,e^{-\gamma z} + V_0^-\,e^{\gamma z})e^{j\omega t}\right] = \\ &= \left|V_0^+\right|\cos(\omega t - \beta z + \Phi^+) + \left|V_0^-\right|\cos(\omega t + \beta z + \Phi^+) \end{aligned} \tag{26}$$

where β is the imaginary part of γ. As can be observed from (26), two different terms are obtained for the total voltage of the signal. The first term represents a wave traveling in the +z-direction (the coefficients of *t* and *z* have opposite signs) and the second term represents a wave traveling in the –*z*-direction (the coefficients of *t* and *z* are both positive). Finally, we can now deduce the expression for the phase velocity:

$$u_p = f\,\lambda = \frac{\omega}{\beta} = \frac{1}{\sqrt{L\,C}} = \frac{1}{\sqrt{\mu\,\varepsilon}} = \frac{1}{\sqrt{\mu_0\,\varepsilon_r\varepsilon_0}} = \frac{1}{\sqrt{\mu_0\,\varepsilon_0}}\frac{1}{\sqrt{\varepsilon_r}} = \frac{c}{\sqrt{\varepsilon_r}} \tag{27}$$

- ***Voltage reflection coefficient***

Making use of (24), (22) can be rewritten in terms of Z_0 in the form

$$I(z) = \frac{V_0^+}{Z_0} e^{-\gamma z} - \frac{V_0^-}{Z_0} e^{\gamma z} \qquad (28)$$

We can now write the expressions for the voltage (21.a) and current (28) of the signal using $\gamma = j\,\beta$, obtaining

$$V(z) = V_0^+ e^{-j\beta z} + V_0^- e^{j\beta z} \qquad (29.a)$$

$$I(z) = \frac{V_0^+}{Z_0} e^{-j\beta z} - \frac{V_0^-}{Z_0} e^{j\beta z} \qquad (29.b)$$

In order to determine the voltage amplitudes of the incident and reflected waves (V_0^+ and V_0^-) from (29.a) and (29.b), we need to consider the total system. The complete circuit includes a generator circuit at its input terminals and a load at its output terminals, as shown in Figure 2.5.

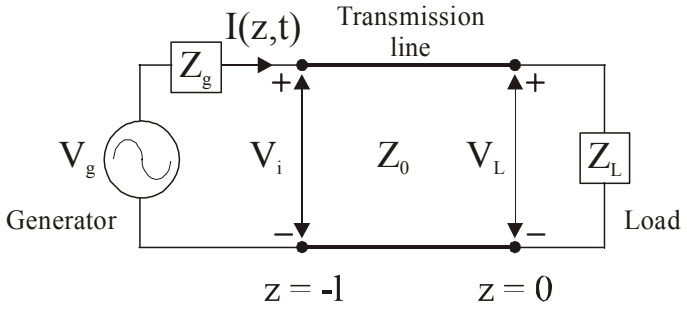

Figure 2.5: Transmission line of length *l* connected at one end to a generator circuit and at the other end to a load Z_L.

For convenience, the origin is chosen at the coordinate *z* which corresponds to the location of the load, Z_L. Therefore, $z = -l$ is the location where the sinusoidal voltage source with phasor V_g and an internal impedance Z_g is placed. The impedance of the load, Z_L, can be expressed as a function of the phasor voltage across it, V_L, and the phasor current running through it, I_L, as follows:

$$Z_L = \frac{V_L}{I_L} \qquad (30)$$

We can now calculate V_L and I_L by estimating the total voltage (29.a) and current (29.b) of the line at z=0:

$$V_L = V(z=0) = V_0^+ + V_0^- \qquad (31a)$$

$$I_L = I(z=0) = \frac{V_0^+}{Z_0} - \frac{V_0^-}{Z_0} \qquad (31.b)$$

Using (31) and (30), the load impedance can be rewritten as:

$$Z_L = \left(\frac{V_0^+ + V_0^-}{V_0^+ - V_0^-} \right) Z_0 \qquad (32)$$

and therefore, V_0^- can be expressed as a function of V_0^+ as:

$$V_0^- = \left(\frac{Z_L - Z_0}{Z_L + Z_0} \right) V_0^+ \qquad (33)$$

The voltage reflection coefficient is defined as the ratio between the amplitude of the reflected voltage wave, V_0^-, and the amplitude of the incident voltage wave at the load, V_0^+. Using (33), this definition can be expressed as a function of characteristic impedance of the line, Z_0, and load impedance, Z_L, as:

$$\Gamma = \frac{V_0^-}{V_0^+} = \frac{Z_L - Z_0}{Z_L + Z_0} \qquad (34)$$

And using (23), in terms of the current amplitudes:

$$\frac{I_0^-}{I_0^+} = -\frac{V_0^-}{V_0^+} = -\Gamma \qquad (35)$$

Although Z_0 of a lossless line is a real number, Z_L is in general a complex quantity. Therefore, Γ needs to be expressed as a complex magnitude:

$$\Gamma = |\Gamma| e^{j\theta_r} \qquad (36)$$

where $|\Gamma|$ is the magnitude of Γ and ϑ_r is its phase angle. For a matched load, $Z_L = Z_0$, and therefore, $\Gamma = V_0^- = 0$.

- ***Voltage Standing Waves Ratio***

The standing wave ratio, VSWR, is defined as the ratio between the maximum and minimum voltage of the signal along the line. We need to obtain then the

expression for the magnituge of the voltage, $|V(z)|$. Inserting the relation $V_0^- = \Gamma V_0^+$ in (29.a) and (29.b) gives the expressions

$$V(z) = V_0^+ (e^{-j\beta z} + \Gamma e^{j\beta z}), \tag{37.a}$$

$$I(z) = \frac{V_0^+}{Z_0} (e^{-j\beta z} - \Gamma e^{j\beta z}). \tag{37.b}$$

We can now deduce an expression for the magnitude of the voltage $|V(z)|$ from (37.a)

$$\begin{aligned} |V(z)| &= \left\{ \left[V_0^+ \left(e^{-j\beta z} + |\Gamma| e^{j\theta_r} e^{j\beta z} \right) \right] \cdot \left[\left(V_0^+ \right)^* \left(e^{j\beta z} + |\Gamma| e^{-j\theta_r} e^{-j\beta z} \right) \right] \right\}^{1/2} = \\ &= \left| V_0^+ \right| \left[1 + |\Gamma|^2 + |\Gamma| \left(e^{j(2\beta z + \theta_r)} + e^{-j(2\beta z + \theta_r)} \right) \right]^{1/2} = \\ &= \left| V_0^+ \right| \left[1 + |\Gamma|^2 + 2|\Gamma| \cos(2\beta z + \theta_r) \right]^{1/2} \end{aligned} \tag{38}$$

where we have used the identity

$$e^{jx} + e^{-jx} = 2\cos x \tag{39}$$

Therefore, since $|\Gamma| \le 1$, maximum and minimum voltage can be easily identified, obtaining the following expression for the VSWR:

$$VSWR = \frac{|V|_{\max}}{|V|_{\min}} = \frac{1 + |\Gamma|}{1 - |\Gamma|} \tag{40}$$

From (38) we can deduce that the variations of $|V(z)|$ and $|I(z)|$ follow a sinusoidal pattern as a function of *z*. This pattern is called standing wave, and it is caused by the interference of the two waves as a consequence of the presence of a mismatch load. The maximum voltage value of the standing-wave pattern, $|V|_{max,}$ corresponds to the position in the line at which the incident and reflected waves are in phase, and the minimum voltage value, $|V|_{min}$, corresponds to destructive interference, which occurs when the incident and reflected waves are in opposite phase. Therefore, the repetition period of the standing-wave pattern is the half of the wavelength from the incident and reflected waves.

- ***Average power***

From (37.a) and (37.b) we can consider the time-average power flow along the line at the point *z* as:

$$P_{av} = \frac{1}{2}\mathrm{Re}\left[V(z)I(z)^*\right] = \frac{1}{2}\frac{\left|V_0^+\right|^2}{Z_0}\left(1-\left|\Gamma\right|^2\right) \qquad (41)$$

Which shows that the average power flow is constant at any point on the line, and that the total power delivered to the load is equal to the incident power ($\left|V_0^+\right|^2 / 2Z_0$), minus the reflected power ($\left|V_0^+\right|^2 \left|\Gamma\right|^2 / 2Z_0$).

- ***Scattering parameters***

A commonly used way for accounting for the losses due to a mismatch is by introducing the so-called scattering parameters. The *s*-parameters matrix relates the voltage waves incident on the ports to those reflected from the ports. For the case of two port networks we have:

$$\begin{bmatrix} V_1^- \\ V_2^- \end{bmatrix} = \begin{bmatrix} s_{11} & s_{12} \\ s_{21} & s_{22} \end{bmatrix} \begin{bmatrix} V_1^+ \\ V_2^+ \end{bmatrix} \qquad (42)$$

A specific element of the [S] matrix can be determined as:

$$s_{ij} = \left.\frac{V_i^-}{V_j^+}\right|_{V_k^+ = 0 \text{ for } k \neq j} \qquad (43)$$

Equation (42) says that s_{ij} is found by driving port *j* with an incident wave of voltage V_i^+, and measuring the reflected wave amplitude, V_i^-, coming out of port *i*. Thus, s_{ii} is the reflection coefficient seen looking into port *i*, and s_{ij} is the transmission coefficient from port *j* to port *i*. Notice that in the case of a symmetric circuit:

$$s_{11} = s_{22} = \Gamma \qquad (44)$$

Therefore, using (41), we can define the magnitude of the *s*-parameters related to the power level of the RF signal in dB as:

$$S_{11} = S_{22} = 10\log\left(\left|\Gamma\right|^2\right), \qquad (45)$$

$$S_{12} = S_{21} = 10\log\left(1-\left|\Gamma\right|^2\right). \qquad (46)$$

In the case of a perfect match, S_{11}=S_{22}=-∞ and S_{12}=S_{21}=0. While for a circuit with a short or open, S_{11}=S_{22}=0 and S_{12}=S_{21}=-∞.

For the cases where an element with certain transmission losses is included in the transmission line, *S*-parameters can be measured directly with a vector network analyzer. Therefore, reflection and transmission losses of the line can be deduced.

2.2.2 Forces in a matched transmission line

As we saw in equations 15.a and 15.b, the energy of a microwave traveling on a transmission line is stored in magnetic and electric energy, and using equation 24 we can also say that it is equally stored between the two. In the case of a parallel plate transmission line (see figure 2.1), electric force attracts the metal sheets towards each other due to the different of its voltage, and magnetic force repel them from each other due to the currents traveling through the sheets in opposite directions. To know the total net force we will estimate the ratio between the electrical and magnetic force per unit area suffered by one of the metal plates of a parallel plate transmission line when a microwave is traveling through it.
First of all we assume that the dielectric between the metal plates is vacuum, and therefore the solution from the Maxwell equations can be written in the form [1]

$$\vec{E}(x,t) = E_0 \cdot \hat{x} \cdot e^{i(\omega t - kz)} \tag{47.a}$$

$$\vec{B}(x,t) = B_0 \cdot \hat{y} \cdot e^{i(\omega t - kz)} \tag{47.b}$$

where E_0 and B_0 satisfy

$$E_0 = c \cdot B_0 \tag{48}$$

being *c* the speed of light. We now estimate the expression of the electrical and magnetical force per unit area using the calculation of the surface charge and current density done in equations 2 and 3.

$$\frac{F_E}{A} = \rho_s \vec{E} = \frac{\rho_s^{\,2}}{\varepsilon_0} \tag{49.a}$$

$$\frac{F_B}{A} = \frac{q}{A}\vec{v} \times \vec{B} = \frac{q}{A} vB = \rho_s vB = J_s B = \frac{J_s^{\,2}}{\varepsilon_0 c^2} = \frac{\rho_s^{\,2} v^2}{\varepsilon_0 c^2} \tag{49.b}$$

If we now proceed to calculate the ratio between the two forces in two different ways as shown in equations 50.a and 50.b

$$\frac{F_E}{F_B} = \frac{\rho_s^{\,2}}{\varepsilon_0} \Big/ \frac{\rho_s^{\,2} v^2}{\varepsilon_0 c^2} = \frac{c^2}{v^2} \tag{50.a}$$

$$\frac{F_E}{F_B} = \frac{\rho_s E}{\rho_s v B} = \frac{\rho_s E c}{\rho_s v E} = \frac{c}{v} \qquad (50.b)$$

we can conclude that the velocity of the wave is *c* (as corresponds to a microwave guided by a transmission line with perfect conductors and vacuum as a dielectric), giving as a consequence that the ratio between electrical and magnetic forces is one. Therefore, we can conclude that the total force felt by the metal sheets which constitute a matched waveguide when a RF signal is present is zero.

2.3 Operating principle and basic theory of a RF MEMS power sensor

2.3.1 Operating principle

We have seen from the previous section that the electric force generated by the voltage difference between the lines is compensated by the magnetic force generated by the opposite currents running in the metal sheets, resulting in an equilibrium situation. As a consequence we can conclude that, by using only a matched transmission line with movable metal sheets, a microwave power sensor based on the movement detection that could be created from the attractive electrical force can not be realized. Nevertheless, a net force can arise when a capacitive discontinuity, small enough to be treated as lumped element, is introduced in the transmission line, because a region is created where the balance between electric and magnetic force is broken. In this case, it can be considered that electrical force is the only force present on that specific region of the circuit.
Assuming that we are within the lumped element approximation, we can treat the capacitance discontinuity as a discrete element. Therefore, for a movable capacitor plate as shown in figure 2.6, the force can be expressed as [2]

$$\vec{F}_{el} = \frac{1}{2}\frac{q^2}{\varepsilon A}\hat{x} = \frac{1}{2}\frac{\varepsilon A}{(d-x)^2}u^2\hat{x} \qquad (51)$$

In this equation, ε is the dielectric constant of the medium, d is the initial gap between the plates, x is the displacement of the movable plate, A is the area of the plates, q is the amount of charge on each plate and u is the voltage between the plates. The voltage and charge are of course related by the capacitance of the structure:

$$C = \frac{q}{u} = \frac{\varepsilon A}{d-x} \qquad (52)$$

Figure 2.6: Schematic drawing of a parallel plate capacitor with one moveable plate.

If we now assume that the voltage applied between the capacitor electrodes is coming from a microwave signal, this will result in a time-dependent, but always attractive, electrical force. And due to its high frequency, well above the mechanical resonance frequency, only the average force is important, and the voltage u in equation (51) is replaced by the RMS voltage amplitude of the microwave signal. Thus, by measuring the displacement of the moveable capacitor plate or by measuring the force needed to keep the plate in its initial position, the (square of the) RMS voltage amplitude of the microwave signal can be obtained. Finally, when the effect caused on the rf signal is small enough to be able to consider the impedance of the transmission line constant, the power of the signal can be deduced by the well known equation (53)

$$P = \frac{V^2}{Z} \qquad (53)$$

The development of a rf power sensor described in this thesis is based on the implementation of such a movable capacitor as a lumped-element discontinuity on the transmission line.

2.3.2 Coplanar Waveguide

In a Coplanar Waveguide all the conductors are in the same plane and on top of a dielectric material, being open to the air at the top [3]. Therefore, this type of structure allows both series and shunt elements be integrated into the line without the need to drill holes into the substrate, being this the most important reason why it was chosen for the realization of the RF power sensor. The configuration of a CPW structure is presented in Figure 2.7. It consists of center electrode with width *W* and two ground planes with widths *GW*. The gap between center conductor and ground plane is *G*. The thickness of the substrate is *h* and the thickness of the transmission line is *t*. If the substrate thickness, h, is large compared to the gap between the center and ground conductors, G, the existence of a ground electrode under the substrate has a negligible influence on the CPW impedance.

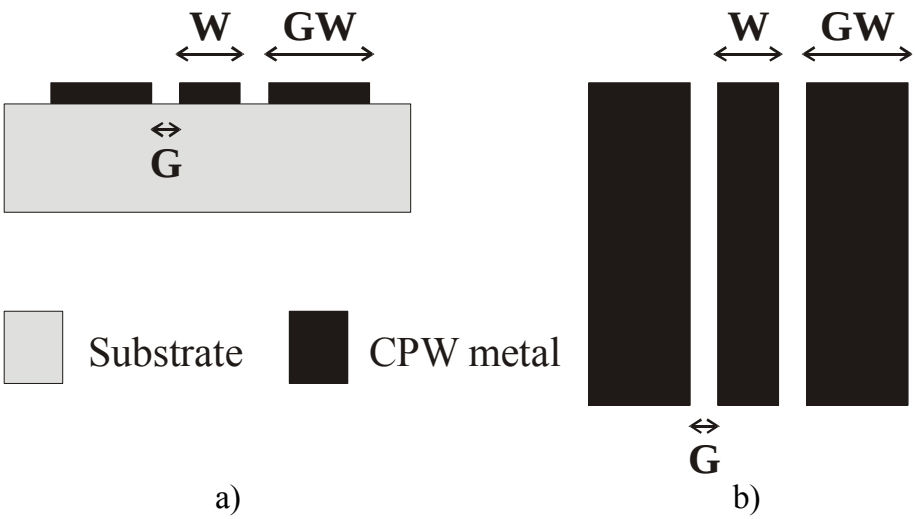

Figure 2.7: Schematic of a Coplanar Waveguide. a) Cross section b) Top view.

In order to calculate analytically the parameters of this kind of transmission line the quasi-static assumption is made, allowing us to use the conformal mapping method [4]. In this method, the capacitance C is divided into two parts: C_1, which is calculated by assuming that all the space is homogeneously filled with air, and C_2, where it is assumed that all the space is homogeneously filled with the substrate material with permittivity (ε_r - 1). Hence, the total capacitance is $C = C_1 + C_2$. The capacitances can be calculated from

$$C_1 = 4\varepsilon_0 \frac{K(k)}{K'(k)} \qquad (54.a)$$

$$C_2 = 2\varepsilon_0(\varepsilon_r - 1)\frac{K(k_1)}{K'(k_1)} \qquad (54.b)$$

where $K(k)$ is the elliptic integral of the first kind and

$$k = \frac{W}{W + 2G} \qquad (55.a)$$

$$k_1 = \frac{\sinh\left(\frac{\pi W}{4h}\right)}{\sinh\left(\frac{\pi(W + 2G)}{4h}\right)} \qquad (55.b)$$

$$K'(k) = K(k') \qquad (55.c)$$

$$k' = \sqrt{(1 - k^2)} \qquad (55.d)$$

Elliptic functions can be calculated using approximations [5]:

$$\frac{K(k)}{K'(k)} \approx \frac{2}{\pi}\ln\left(2\left(\sqrt{\frac{1+k}{1-k}}\right)\right) \quad for \ \frac{1}{\sqrt{2}} \le k \le 1 \qquad (56.a)$$

$$\frac{K(k)}{K'(k)} \approx \frac{\frac{\pi}{2}}{\ln\left(2\left(\sqrt{\frac{1+k'}{1-k'}}\right)\right)} \qquad for\ 0 \le k < \frac{1}{\sqrt{2}} \qquad (56.b)$$

The effective dielectric constant can be now written as

$$\varepsilon_{reff} = \frac{C}{C_1} = \frac{C_1 + C_2}{C_1} = 1 + \frac{e_r - 1}{2}\frac{K(k_1)}{K'(k_1)}\frac{K'(k)}{K(k)} \qquad (57)$$

and using equation 27 we can then calculate the phase velocity, and deduce the expression for the characteristic impedance, which is given by

$$Z_0 = \frac{1}{(C_1 + C_2)v_p} \qquad (58)$$

After substitutions we obtain the characteristic impedance of the line as

$$Z_0 \approx \frac{30\pi}{\sqrt{\varepsilon_{reff}}}\frac{K'(k)}{K(k)} \qquad (59)$$

To take into account the thickness of the transmission lines, extra correction factor is needed [6]:

$$\Delta = \frac{1.25t}{\pi}\left(1 + \ln\left(\frac{4\pi W}{t}\right)\right) \qquad (60)$$

The width of the center conductor comes $W + \Delta$, the gap between the center and the ground conductor comes $G - \Delta$, and k is changed to k_Δ:

$$k_\Delta = \frac{W + \Delta}{[(W + \Delta) + 2(G - \Delta)]} \qquad (61)$$

Accordingly, the effective dielectric constant becomes

$$\varepsilon_{reff\Delta} = \varepsilon_{reff} - \frac{\varepsilon_{reff} - 1}{\frac{W}{0.7 \cdot t} \cdot \frac{K(k)}{K'(k)} + 1} \qquad (62)$$

Up to here, the analysis has been done under the conditions of a CPW with infinitely wide ground lines (i.e. $GW = \infty$). If the ground lines have finite width the equations for k_1 and k_1' change to [7]:

$$k_1 = \sqrt{\frac{1+a_1+a_2}{(1+a_1)(1+a_2)}} \qquad (63.a) \qquad k_1' = \sqrt{(1-k_1^2)} \qquad (63.b)$$

$$a_1 = \frac{\sinh\left(\frac{\pi \cdot GW}{2h}\right)\sinh\left(\frac{\pi(GW+W+2G)}{2h}\right)}{\sinh\left(\frac{\pi \cdot G}{2h}\right)\sinh\left(\frac{\pi(W+2G)}{2h}\right)} \qquad (63.c)$$

$$a_2 = \frac{\sinh^2\left(\frac{\pi \cdot W}{4h}\right)}{\sinh\left(\frac{\pi \cdot G}{2h}\right)\sinh\left(\frac{\pi(W+2G)}{2h}\right)} \qquad (63.d)$$

But if the ground conductor width GW is 3 times wider than W then its effect on Z_0 and ε_{reff} can be ignored [7].

2.3.3 Bridge design

In figure 2.8 we show the so called 'bridge design', where the rf power sensor is composed of a clamped-clamped beam placed on top of the coplanar waveguide. Extra electrodes are fabricated under the 'bridge' in order to measure its deflection due to the presence of microwave signals capacitively. By fabricating the structure small enough with respect to the wavelength of the signal to be measured, it can be considered as a lumped element. Therefore, such a capacitive element can be treated as a regular movable capacitor in order to characterize it.

Bandwidth

The insertion of a capacitor in the transmission line changes its characteristic impedance and inevitably results in reflections and transmission losses, since a new capacitance (C_S) is added to the line (see figure 2.8).

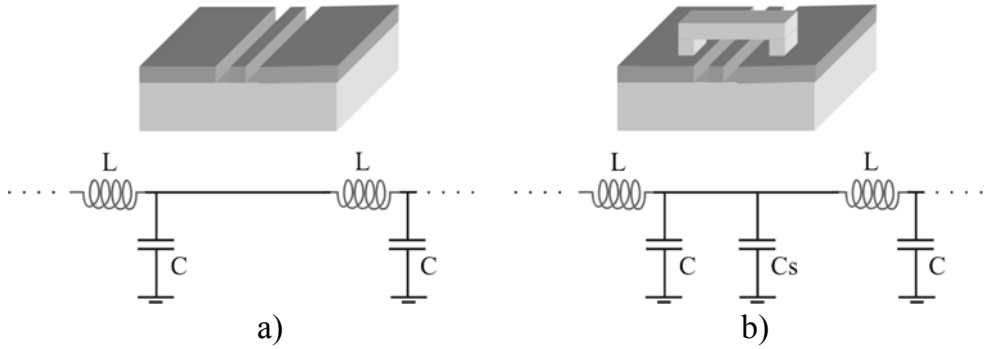

Figure 2.8: CPW and lumped element model (a) and CPW with a movable capacitor model (b).

As a consequence of the new added capacitance, the new characteristic impedance of the transmission line becomes

$$Z_L = Z_C \| Z_0 = \frac{1}{j\omega C_S + 1/Z_0} \qquad (64)$$

where Z_0 is the nominal impedance of the line, Z_L is the impedance seen at the discontinuity at the position of the capacitance and ω is the angular frequency. Now, using equation 34, the voltage reflection coefficient can be calculated, giving as a result

$$\Gamma = \frac{Z_L - Z_0}{Z_L + Z_0} = \frac{\dfrac{1}{j\omega C_S + 1/Z_0} - Z_0}{\dfrac{1}{j\omega C_S + 1/Z_0} + Z_0} = \frac{1}{\dfrac{2}{j\omega Z_0 C_S} + 1} \qquad (65)$$

Thus, the reflection losses increase with frequency and the maximum frequency for which the sensor can be used, i.e. the bandwidth of the sensor, is defined by the capacitance value. Nevertheless, a readjustment of the CPW impedance can be realized by introducing new elements directly before and after the sensor capacitance, increasing the bandwidth [8]. In particular, redesign of the CPW dimensions in order to make the transmission line more inductive and less capacitive can retune the waveguide when the treated area is small enough to be still considered as a lumped element. Figure 2.9 shows how an extra series inductance (L_1=L_2>L) and a lower ground capacitance (C_1=C_2<C) implemented in the CPW surrounding the sensor can be used to retune the characteristic impedance of the waveguide to the desired 50 Ohm.

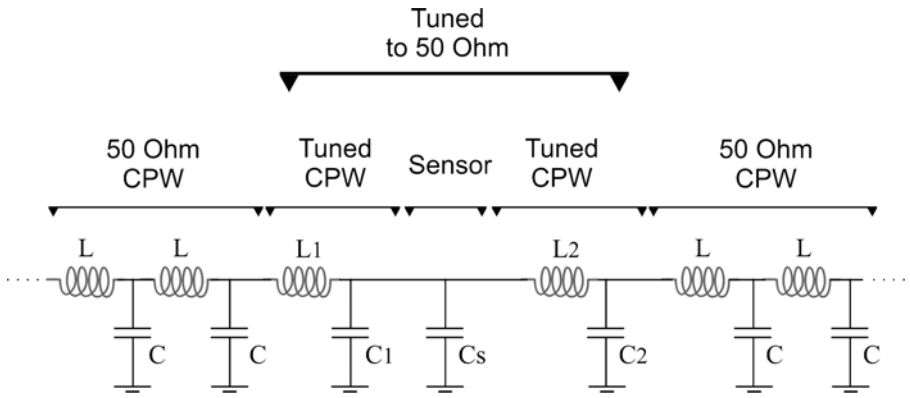

Figure 2.9: Schematic based on lumped elements theory showing the operation principle for the matching optimization of a capacitive power sensor.

As a consequence, larger bandwidth than the expected from the presence of the extra capacitance can be obtained by a careful design of the transmission line for those frequencies which wavelength is much smaller (ten times) than the total length of the treated area.

Sensitivity

The sensitivity of an RF capacitive MEMS power sensor is determined by its capability of transfer the electrical force induced by the microwave signal into displacement of the movable capacitance which acts as a sensor. Therefore, a minimization of the spring constant is needed in order to optimize the power readout. For a clamped-clamped beam configuration of the capacitive MEMS sensor, a change in dimensions could already give a very wide range of spring constant values, since for a clamped-clamped beam the spring constant as a function of the geometry can be describe as a first approximation by [9]

$$K = \frac{16\,E\,a^3\,B_W}{B_L^{\,3}} \qquad (66)$$

where 'E' is the Young modulus of the material used to fabricate the membrane, 'a' the thickness, 'B_w' the length of the beam along its two free sides, and 'B_L' the beam length in between its clamped regions (see figure 2.10).

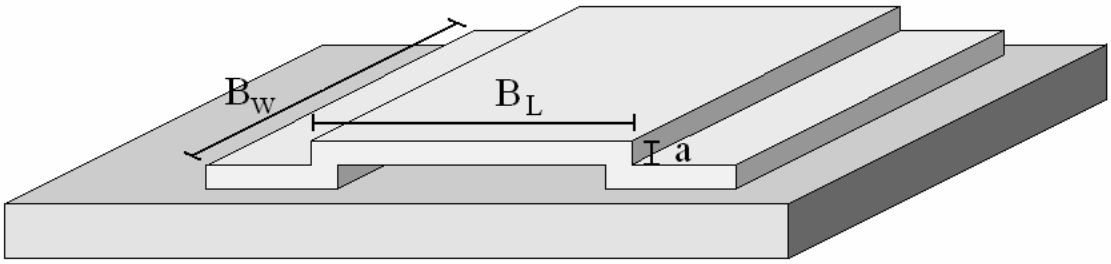

Figure 2.10: Schematic drawing of a clamp-clamp beam.

As can be noticed, w and a are very interesting parameters to vary since their relation to the spring constant goes with the third power. However, special care needs to be taken with respect to the tensile stress of the material used [9]. As an example, figure 2.11 shows spring constant values for an aluminum beam where the distance between the clamp areas is changed with different residual stress values in the structural material. Although we can clearly see that a factor of 29 is obtained when the length change from 300 μm to 900 μm if no nominal stress is added to the sensor, the calculation of the spring constant with a residual stress of 10 MPa, using numerical techniques [10], lowers that factor to 4.

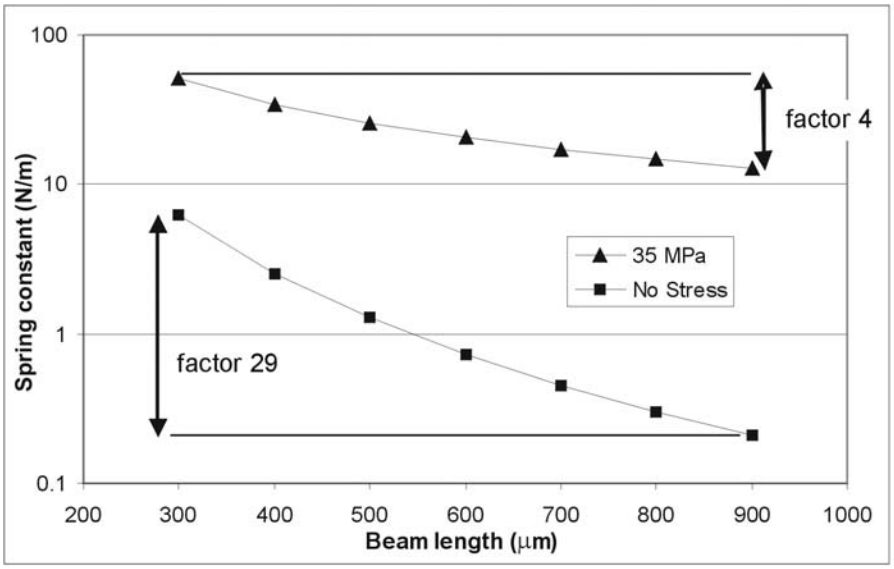

Figure 2.11: Comparison of spring constant estimation for clamp-clamp beams with different lengths, with and without taking into account stress in the structural material.

Therefore, special care has to be taken not only on the geometry but also in the residual stress of the material used for the realization of the beam in order to understand its behavior.
Another important aspect is the effect of the mismatch caused by the sensor on the voltage across the bridge. In equation 53 we have related power and voltage

considering a perfect match. But when the signal is delivered by a power source, and a shunt capacitance is present, C_S, the voltage felt on the capacitor related to the power delivered from the source, P_s, is given by [11]:

$$V_c = \sqrt{\frac{4Z_0 P_s}{4 + Z_0^{\,2}\omega^2 C_S^{\,2}}} \qquad (67)$$

In this way, the sensitivity could be affected by the extra capacitance introduced from the sensor and the frequency of the signal to be detected. Nevertheless, this effect is only relevant for very high capacitance and/or frequency values as illustrated in the graph shown in figure 2.12.

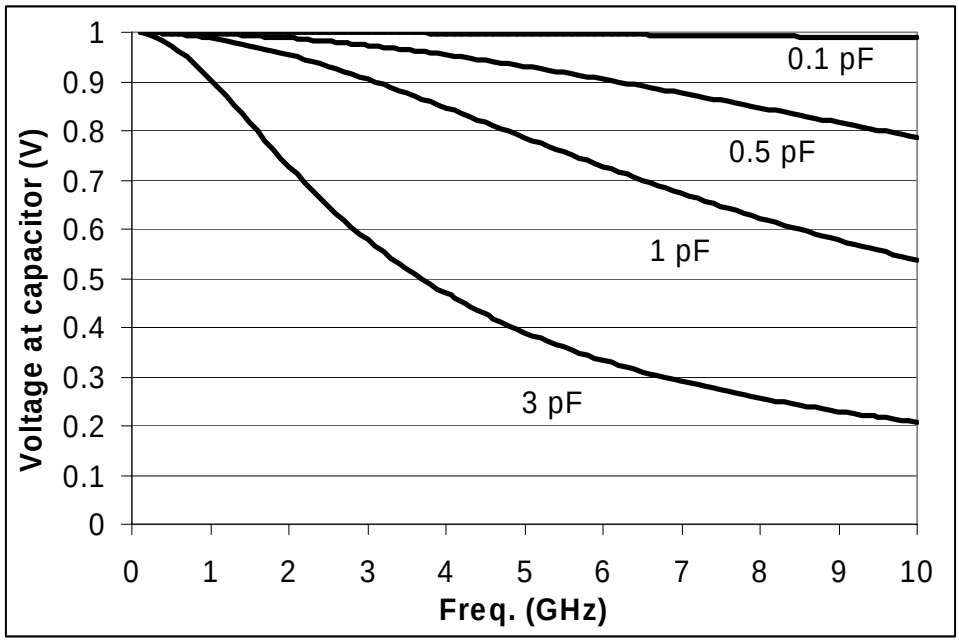

Figure 2.12: Voltage across a shunt capacitance, V_c, due to the presence of an RF signal for different capacitance and frequency values.

Resolution and noise

The ultimate power resolution will be limited by the thermomechanical noise of the moveable membrane. An estimate for the amount of noise can be obtained by considering the membrane as a second order spring-mass system. In that case the mechanical noise force density acting on the mass is given by [12]:

$$\frac{\overline{F_n^2}}{\Delta f} = \frac{4K\,k_B T}{\omega_0 Q} = \frac{4\sqrt{KM}\,k_B T}{Q} \qquad (68)$$

where k_BT is the thermal energy, Δf is the readout bandwidth, and K, M, ω_0 and Q are the spring constant, mass, mechanical resonance and quality factor. This noise force is shaped by the force-to-displacement transfer function of the system, just like the "signal" force given by (51). Combining (51) and (68) gives the attainable power resolution. For the case of 1 Hz readout bandwidth, the minimum detectable power is:

$$S_p = \frac{u_{RMS,m}{}^2}{Z_0} = \frac{2d}{CZ_0}\sqrt{\frac{4\sqrt{KM}\,k_B T}{Q}} \qquad (69)$$

In this equation C is fixed by the required high frequency bandwidth. Thus, to improve the power resolution we should decrease the air-gap d, spring constant K and mass M or increase the quality factor Q. The latter can be accomplished by operating the sensor in vacuum. Inserting some reasonable values it can be shown that a power resolution in the order of nanoWatts should be feasible.

2.4 Conclusions

The basic theory of a microwave traveling through a transmission line has been described, and the most relevant parameters deduced. The operation principle of the RF MEMS power sensor, based on the introduction of a capacitive element on the transmission line, was presented. The so called 'bridge design' was then proposed. Finally, theoretical limitations of the sensor regarding bandwidth and sensitivity are discussed and estimated.

2.5 References

[1] Jackson J. D.: “Classical Electrodynamics”, John Wiley & Sons, Inc., 1999.

[2] Elwenspoek M., Wiegerink R.: “Mechanical Microsensors”, Springer, 2001.

[3] Wen C. P.: "Coplanar waveguide: A surface strip transmission line suitable for nonreciprocal gyromagnetic device applications," *IEEE Transaction on Microwave Theory and Techniques,* vol. MTT-17, Dec. 1969, pp. 1087-1090.

[4] Veyres C., Fouad-Hanna V.: "Extensions of the application of conformal mapping techniques to coplanar lines with finite dimensions," *Int. J. Electronics*, vol. 48, no.1, 1980, pp. 47-56.

[5] Hilberg W.: "From approximations to exact relations for characteristic impedances," *IEEE Transaction on Microwave Theory and Techniques*, vol. MTT-17, no. 5, May 1969, pp. 259-265.

[6] Bachert P. S.: "A coplanar waveguide primer", *R.F. Design*, vol.11, no.7, July 1988, pp. 52-57.

[7] Hoffman R. K.: "Handbook of Microwave Integrated Circuits," Artech House Inc., Norwood, 1987.

[8] T. Vähä-Heikkilä, J. Kyynäräinen, A. Oja, J. Varis, and H. Seppä, “Capacitive MEMS Power Sensor”, *The 3rd Workshop on MEMS for Millimeterwave Communication*, Crete, June 26th-28th, 2002.

[9] James M. Gere, Stephen P. Timoshenko, ”Mechanics of materials”, PWS Pub. Co., 1997.

[10] Sayanu Pamidighantam, Robert Puers, Kris Baert and Harrie A C Tilmans, “Pull-in voltage analysis of electrostatically actuated beam structures with fixed–fixed and fixed–free end conditions”, *J. Micromech. Microeng*. 12 (2002) 458–464

[11] X Rottenberg, S Brebels,W De Raedt, B Nauwelaers and H A C Tilmans, “RF-power: driver for electrostatic RF-MEMS devices”, *J. Micromech. Microeng.* 14 (2004) S43–S48.

[12] Nguyen C.T.-C., "Micromechanical Signal Processors," Ph.D. Thesis, Berkeley University, December 1994.

Chapter 3

Design and simulations

3.1 Introduction

In this chapter, the design of the so-called 'bridge-type' RF power sensor is presented, and theoretical and simulated results are presented and discussed. The design basically consists of an electrode, the "bridge", suspended above the signal line of a coplanar waveguide (CPW). Obviously, the overall response of the sensor depends largely on the performance of the CPW. Reflection and transmission losses of the complete sensor can never be better than those of the basic CPW. Therefore, in the next section we will first focus on the CPW. Next, in Section 3.3, two different types of bridge sensor will be presented having a grounded and a floating bridge electrode. The theoretical response will be calculated and an estimate is given regarding their RF performance and sensitivity. Finally, in Section 3.4, the compensation method needed to obtain a larger bandwidth, which was discussed in Chapter 2, will be applied to the sensor with floating bridge electrode and simulation results will be presented and discussed.

3.2 Coplanar Waveguide

The coplanar waveguide (CPW) is one of the most commonly used RF circuits and was chosen for the transmission of the signals to be measured by the RF

power sensor. This choice was made for two reasons. Firstly, a CPW structure is easy to fabricate since only one metal layer is required. Secondly, both the ground and signal line are easily accessible for measurements since they are on the same side of the substrate.
Figure 3.1 shows a cross-sectional drawing of a CPW, indicating the most important dimensions, i.e. the width of the center (signal) line W, the gap distance between the center line and the ground lines G, the thickness of the metal layer t, and the permittivity ε_r and thickness h of the substrate material.. Together with the thickness and permittivity of the substrate material these dimensions define the characteristic impedance of the CPW.

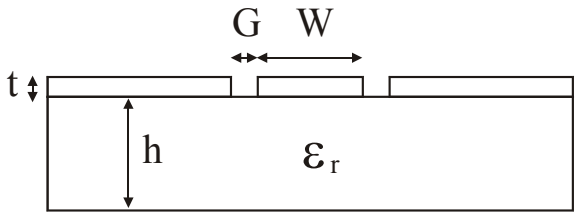

Figure 3.1: Cross-sectional view of a CPW.

Metal thickness
First of all, let's consider the choice for the metal lines thickness. In principle, the metal should be as thick as possible in order to reduce resistive losses. However, in the case of RF signals most of the current flows in the thin outer layer of the conductor and decreases exponentially with the distance from the surface [1, 2]. Thus, at RF frequencies the effective thickness of the metal may be much smaller than the actual physical thickness. In order to estimate the thickness used by the RF signal, a parameter called skin depth, δ_s, is introduced [1, 2]. The skin depth characterizes how well an electromagnetic wave can penetrate into a conducting medium, and it is defined as the distance from the surface at which the wave magnitude has decreased by a factor of $e^{-1} \approx 0.37$. The value of the skin depth is only dependent of the material properties and the frequency of the signal running through it as shown in equation (1):

$$\delta_S = \frac{1}{\sqrt{\pi f \mu \sigma}} \qquad (1)$$

In practice it does not make much sense to increase the metal thickness to more than about 3 times the skin depth. Figure 3.2 shows the skin depth as a function of frequency for three commonly used metals. We see that at 4 GHz the skin depth is in the order of 1 μm so that a CPW thickness of 3 μm would be enough. As will be shown in Chapter 4, a thickness of more than 1 μm is difficult to realize in the chosen fabrication process. Therefore, we will choose the metal thickness to be 1

μm although this is less than sufficient and will result in additional transmission losses.

Width of the signal line and gap distance

Another important aspect to be taken into account for the design of the CPW is the choice for the dimensions of the gap between the lines G and the signal line width W. They should be chosen such that standard 50 Ω characteristic impedance is obtained (which is supposed to be used in the circuit where the sensor will be inserted) and simultaneously the dimensions should be suitable for integration of the sensor bridge. Figure 3.3 shows the values of G and W which result in 50 Ω characteristic impedance for two different metal thicknesses. These values were calculated using the expressions presented in Section 2.3.2. It is assumed that the ground lines are at least 3 times wider than the signal line so that the influence of the width of the ground lines can be ignored. Furthermore, a dielectric with thickness of 500 μm and relative dielectric constant of 6.2 (the case for AF45 glass [3]) is assumed.

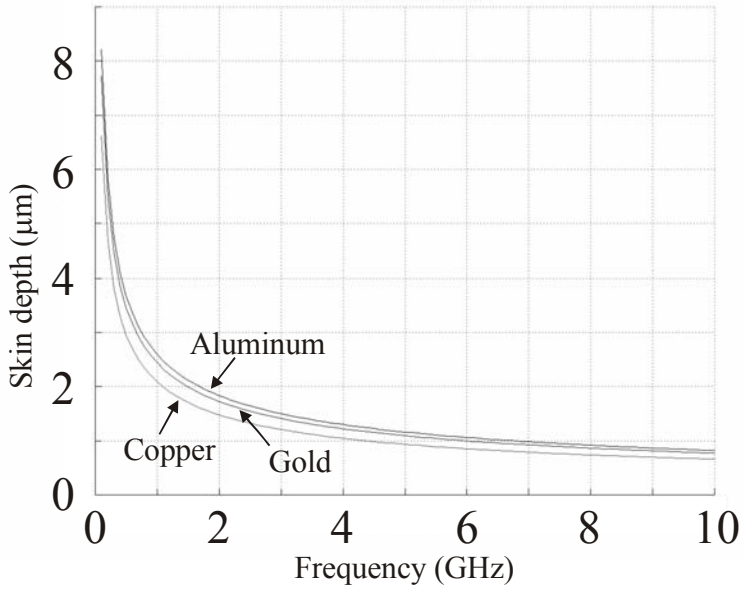

Figure 3.2: Skin depths for aluminum, gold, and copper transmission lines as a function of frequency.

As mentioned before, the thickness of the CPW is 1 μm although 3 μm would be optimal. The width W of the signal line needs to be compatible with the dimensions of sensor bridge that is suspended above the line, i.e. it should not be wider than the maximum feasible length of the bridge. Furthermore, a suitable value for the capacitance between bridge and signal line has to be obtained. Assuming a gap between bridge and signal line in the order of 1 μm and a desired capacitance in the range of 0.1 pF (see figure 3.6) we can conclude that the signal

line width should be at the order of 100 μm, leading to a gap distance of 25 μm. In fact, CPWs with the same combination of W = 100 μm and G = 25 μm are found also in other RF MEMS devices, see e.g. [4,5]

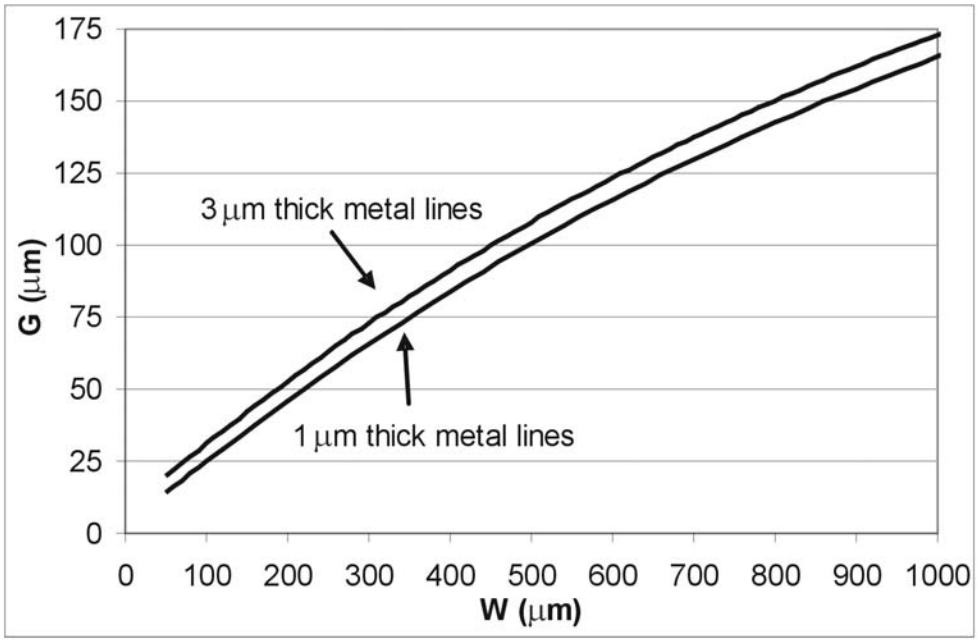

Figure 3.3: CPW dimensions in order to get the standard characteristic impedance 50 Ω for two different metal thicknesses, 1 and 3 μm.

3.3 Bridge design

We will now consider the various design aspects of the suspended bridge which is used as the capacitive sensing element of the sensor. We will do this for two different types of bridge designs, namely the 'grounded bridge' and the 'floating bridge'. In the first case the bridge is electrically connected to the ground lines of the CPW. This has the advantage that the RF behavior of the sensor is well-defined and easy to model. However, detecting the deflection of the bridge by means of a capacitance measurement becomes difficult because one side of the capacitor is connected to ground and parasitic capacitance cannot be distinguished from the sensor capacitance. In the case of the 'floating bridge' the bridge is not electrically connected to the ground lines. This improves significantly the accuracy of the capacitance measurement as is shown below, however it requires some additional considerations to ensure that for the RF signal the bridge can still be regarded as grounded. In both cases the length of CPW underneath the sensor bridge should not be more than a few millimeters so that the sensor capacitance can still be considered as a lumped element up to frequencies of 4 GHz

($\lambda = 7.5\,cm$). Only then the effect of the additional capacitance on the transmission line can be explained by using its lumped circuit equivalent.

3.3.1 Grounded bridge

Figure 3.4 shows a schematic overview of the grounded bridge design. The bridge is attached to the ground lines at both ends. The added capacitance to the transmission line can be calculated simply by considering the overlapping area between the bridge and the central line. Additional (sensing) electrodes are placed under the bridge between the signal and ground lines to measure the deflection of the bridge. In principle one could of course also use the bridge-to-signal line capacitance for this purpose, however this will be complicated by the presence of the RF signal. Slots are made in the ground lines under the bridge to make room for the sensing electrodes and connecting wires. The presence of the sense electrodes will not influence the RF performance since for the RF signal these electrodes can simply be regarded as being at ground potential. A potential problem is caused by the interruption of the ground lines, forcing the RF currents to flow through the bridge.
The grounded bridge configuration was chosen for the first realized prototypes because it allows the use of a relatively short bridge (it only has to extend over the signal line and sense electrodes), thus optimizing the chances for successful fabrication of the sensor. Measurement of the capacitance changes due to displacement of the bridge becomes of course more complicated in de grounded bridge design. The fact that the capacitance to be measured is at one side grounded makes that accurate 4-port impedance measurement techniques cannot be used. Furthermore, any parasitic capacitance between the sense electrodes and ground will be in parallel with the measurement capacitor. Changes in parasitic capacitance cannot be distinguished from changes in the measurement capacitance and will limit the obtained resolution.
It must be emphasized that the first prototype sensors were not designed for optimal performance. The primary goal was to demonstrate that an RF power sensor based on sensing the electric force is feasible. The design was chosen such that the chances for successful fabrication were optimal, i.e. the gap distance x and membrane thickness h were chosen relatively large and the length of the membrane B_L relatively short. Table 3.1 lists the dimensions of the parameters chosen for the design of a grounded bridge sensor related to the design shown in figure 3.4.

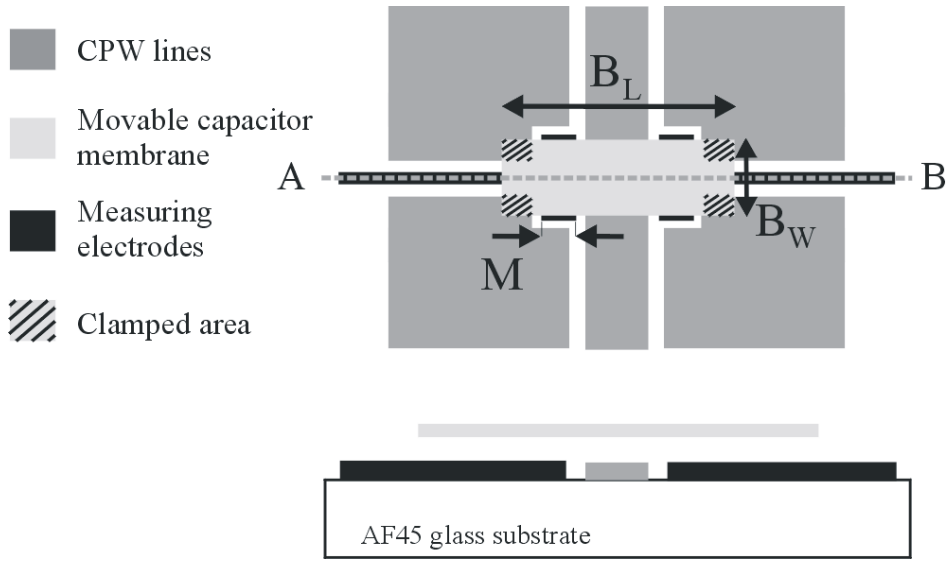

Figure 3.4: Schematic overview of a grounded RF power sensor design (top view and cross section).

B_W	M	B_L
3600 μm	50 μm	300 μm
1800 μm		
200 μm		

Table 3.1: Chosen dimensions for the bridge width (B_W) and length (B_M), and measuring electrode width (M). Other dimensions like the gap distance x and membrane thickness h can be adjusted during the fabrication of the devices and are in the order of 1 μm.

RF performance

For the three realized prototypes we can easily calculate the capacitance added to the transmission line by considering the overlap between the bridge and signal line. As discussed in chapter 2, this capacitance causes an impedance mismatch resulting in reflection losses. Assuming a gap distance of 1 μm the added capacitance for the three different bridge sizes is 0.18, 1.6, and 3.2 pF. Figure 3.5 shows a plot of the calculated reflection losses (magnitude of S_{11} parameter) as a function of frequency (equations 45 and 65 from chapter 2). We see that only the design with a bridge width W of 200 μm is really suitable for operation at GHz frequencies with reflection losses below -26 dB up to 2 GHz. The other two designs are meant for characterization purposes at lower signal frequencies since the small capacitance values in the high-frequency design will make accurate characterization very difficult.

The results illustrate very well the strong relation between capacitance and return losses introduced in the transmission line. We can clearly see that for the designs where large capacitor values are introduced in order to ensure successful readout of the sensor, also higher mismatch losses are obtained. There is a clear trade-off between sensitivity and bandwidth.

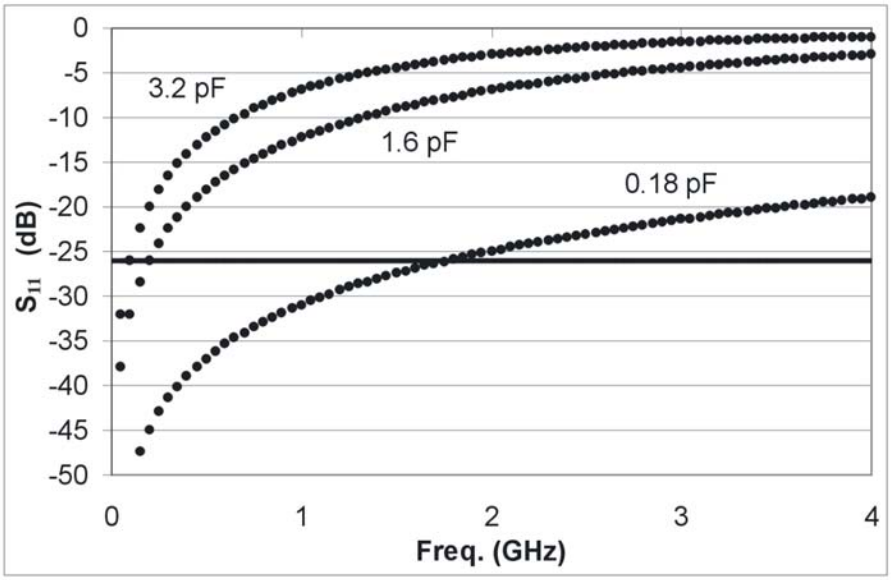

Figure 3.5: Calculated reflection losses for the three different grounded-bridge designs (solid lines) and target specifications of the sensor (dashed line).

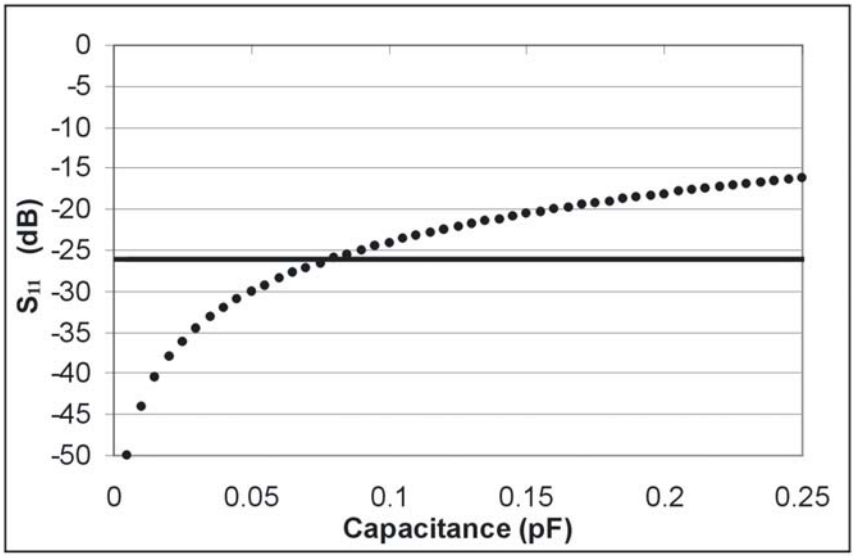

Figure 3.6: Calculated reflection losses at 4 GHz as a function of the extra capacitance introduced in the circuit (symbols) and target specifications of the sensor (solid line).

We can now calculate the maximum allowed capacitance in order to fulfill the specifications up to 4 GHz. Figure 3.6 shows the magnitude of the S_{11} parameter expressed in dB as a function of the extra capacitance introduced in the transmission line for a frequency of 4 GHz. As can be observed, no higher values than 0.08 pF can be added to the system if the target specifications are wanted to be achieved.

Mechanical behavior and sensitivity

In this section, we will derive an estimate for the sensitivity of the sensor by calculating the deflection of the grounded bridge design for a given voltage at the signal line. In order to do that, we need to estimate the effective stiffness of the bridge. As a first approximation, we will consider our sensor as a clamped-clamped beam with immovable edges, subjected to a symmetrically distributed transverse load q_0 and an axial force N as indicated in Figure 3.7. A detailed analysis of such a configuration can be found in [6]

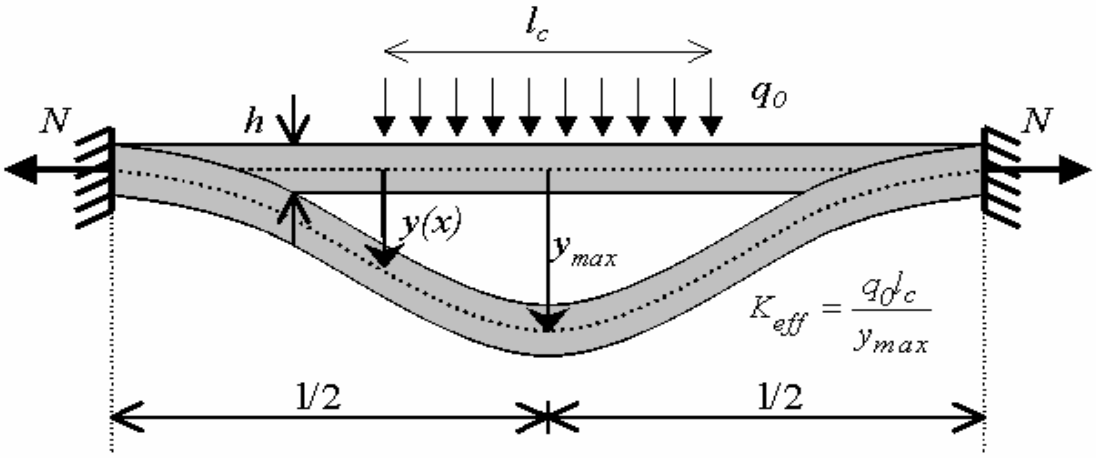

Figure 3.7: Schematic of a clamped-clamped beam under symmetrically distributed load (q_0) and axial force (N).

Following this analysis we can define an effective stiffness K_{eff} of our bridge as a function of the geometrical dimensions and estimated residual stress in the structural material:

$$K_{eff} = \frac{q_0 l_c}{y_{\max}} = \frac{-8k^2 l \lambda_r N \cosh\left(\frac{kl}{4}\right)}{\left(8 + k^2 l^2 (\lambda_r - 2)\lambda_r\right)\cosh\left(\frac{kl}{4}\right) - 8\cosh\left[\frac{kl}{4}(1 - 2\lambda_r)\right] + 4kl\lambda_r \sinh\left(\frac{kl}{4}\right)} \quad (2)$$

$$N = (\hat{\sigma}_0 + \sigma_{NL})bh \quad (3)$$

$$\lambda_r = \frac{l_c}{l} \tag{4}$$

$$k = \sqrt{\frac{12N}{\hat{E}bh^3}} \tag{5}$$

where y_{max} is the maximum deflection of the beam, h is the thickness, b is the width, $\hat{\sigma}_0 = \sigma_0(1-\nu)$ is the residual film stress and $\sigma_{NL} = \pi^2 E y^2_{max}/4l^2$ is an estimate of the induced axial stress due to the non-linear stretching [7, table 12]. The effective Young's modulus $\hat{E}$ is equal to E for $b \approx h$, and equal to the plate modulus $E/(1-\nu^2)$ for $b > 5h$.

Once the effective stiffness, K_{eff}, of the bridge is obtained, the mechanical force can be calculated for every displacement value. Therefore, we can estimate the maximum deflection of the beam at a given voltage by finding the displacement where electrical and mechanical forces are equal.

The read-out of the sensor consists in measurement of the capacitance between the bridge and the measuring electrodes placed below. In order to give an estimation of this capacitive change, the shape of the deformed bridge needs to be obtained and the geometrical distribution of the measuring electrodes has to be taken into account. A good approximation to the shape of the beam can be obtained by using the mode shape functions or eigenfunctions of the beam evaluated for zero axial load [8-11]:

$$y_i(x) = 1.259\left\{\cos(k_i x) - \cosh(k_i x) + \frac{\cos(k_i l) - \cos(k_i l)}{\sinh(k_i l) - \sin(k_i l)}\left[\sinh(k_i x) - \sin(k_i x)\right]\right\} \tag{6}$$

where k_i are constants determined by the order of the mode ($k_1 l \approx 4730$ for a clamped-clamped beam), and the coefficient 1.259 is introduced for scaling purposes, such that $y_1(l/2)=2$. As illustrated in figure 3.8, an effective gap of the beam at the area where the measurement electrodes are located, d, can be now calculated as a function of the maximum displacement of the beam ($x=l/2$). In this way, the capacitance change in the measuring electrodes can be obtained.

Figure 3.9 shows the calculated sensitivity, in fF per watt, for the three different bridge designs (left axis). The calculations were done as a function of the residual stress σ_0 in the bridge material. The thickness of the bridge and the gap between the bridge and the signal line were assumed to be 1 μm.

Since the amount of RF power level we can deliver to the sensor is limited by the RF power source used for the measurement, it is useful to calculate the maximum capacitance change which can be expected. Using the right y-axis from figure 3.9, we obtain the capacitance change for the different sensors at 0.08 W, which is the maximum power possible to deliver with the available equipment.

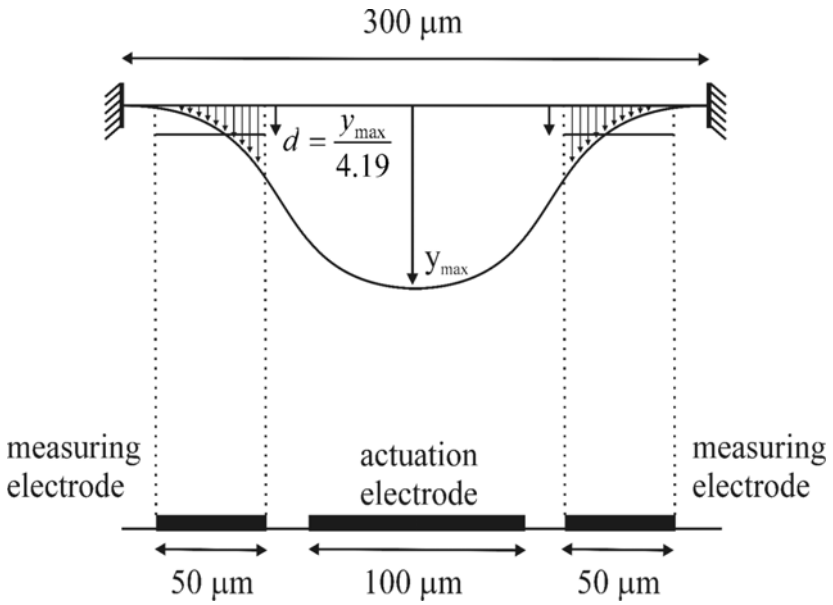

Figure 3.8: Drawing of the grounded bridge showing the relation between the effective deflection on top of the measuring electrodes (d) with respect to the maximum displacement (y_{max}).

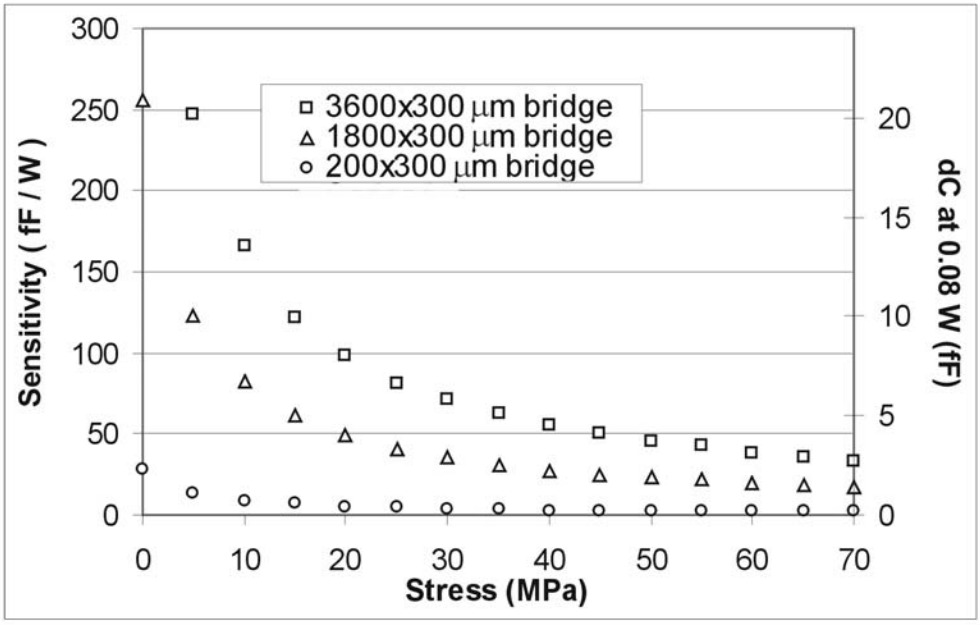

Figure 3.9: Calculated influence of the residual stress on: sensitivity of the sensors (left y-axis), and expected capacitance change at the maximum power delivered by the power source, 0.08 W (right y-axis).

The minimum capacitance change we will be able to measure is in the order of fF, and therefore we can conclude that, even for the largest bridge, higher values of stress than 20 MPa start to compromise the RF resolution of the sensor.

3.3.2 Floating bridge

Figure 3.10 shows the schematic overview of a floating bridge design. The bridge now extends over the entire CPW including the ground lines. Therefore, the capacitance added to the transmission line needs to be estimated by considering three different capacitances: from the central line to the bridge, and from the bridge to the ground lines and measuring electrodes. The electrical connection to the sense electrodes should be made such that for the RF signal they can be regarded either as floating or as being grounded.
The measuring electrodes are placed in between the ground lines and the clamp area of the bridge so that the connecting wires do not need to cross the ground lines as in the grounded-bridge configuration.

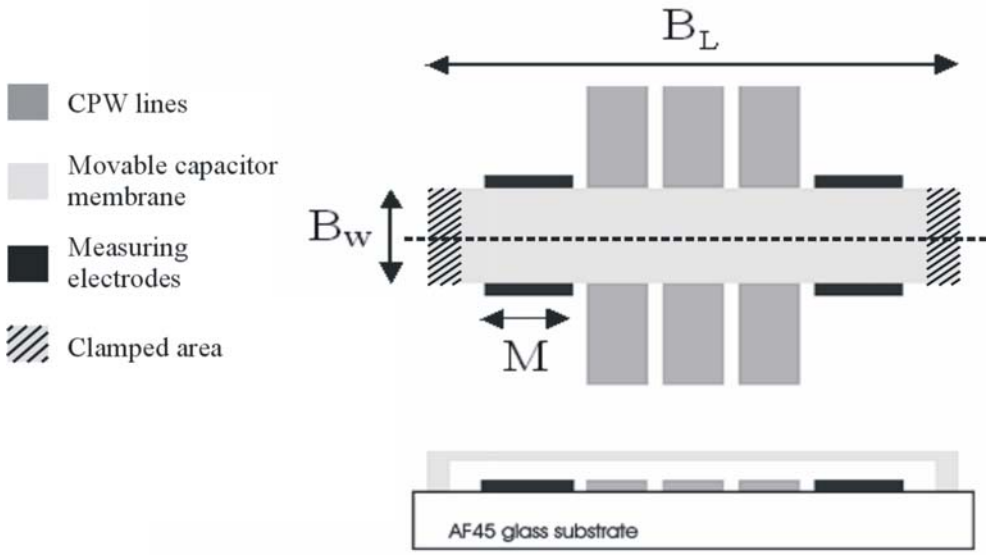

Figure 3.10: Schematic overview of a floating rf power sensor design: a) top view, b) cross section.

For the floating-bridge design the aim was to obtain significantly higher sensitivity and better RF performance, compared to the grounded-bridge design. As a consequence of the design, long distance between the clamped areas is needed (B_L), increasing the risk of failure during fabrication and decreasing the fabrication yield. The longer bridge also results in a lower spring constant and increased sensitivity. Furthermore, since the bridge is now floating, accurate 4-port impedance measurement techniques can be used to measure the capacitance between bridge and sense electrodes. Therefore, lower capacitance is required in

order to get similar or even better sensitivity compared to the grounded bridge design, increasing the bandwidth of the sensor. Table 3.2 lists the dimensions of the bridge and sense electrodes used in the floating bridge design.

B_W	M	B_L
220 μm	200 μm	900 μm
110 μm		

Table 3.2: Different dimensions chosen for the floating bridge design.

RF performance

Again, the RF performance is mainly defined by the capacitance that is added to the transmission line. This capacitance now consists of a series connection of the capacitance from the signal line to the bridge and the capacitance from the bridge to the ground lines and measuring electrodes. Since measuring electrodes are at ground potential (the low potential of an impedance analyzer), the capacitance from the bridge to ground can be considered much larger than the capacitance to the signal line (see figure 3.12). Due to that, we can assume that the total added capacitance can be calculated by the overlapping area between bridge and signal line.

For the two designs with bridge widths of 110 and 220 μm and a gap distance of 1 μm, the calculated extra capacitance is 0.095 and 0.19 pF respectively. Figure 3.11 shows the calculated reflection losses (magnitude of S_{11} in dB) for these capacitance values as a function of frequency. As can be observed, as a consequence of the dimensions of the bridge, results very close to the specifications are obtained.

Mechanical behavior and sensitivity

We can proceed now, as we did for the grounded bridge, with the estimation of the sensitivity of the sensor using capacitive readout. As can be observed from figure 3.12, the distribution of the measuring electrodes along the bridge length ends with a higher effective deflection, d, with respect to the grounded design.

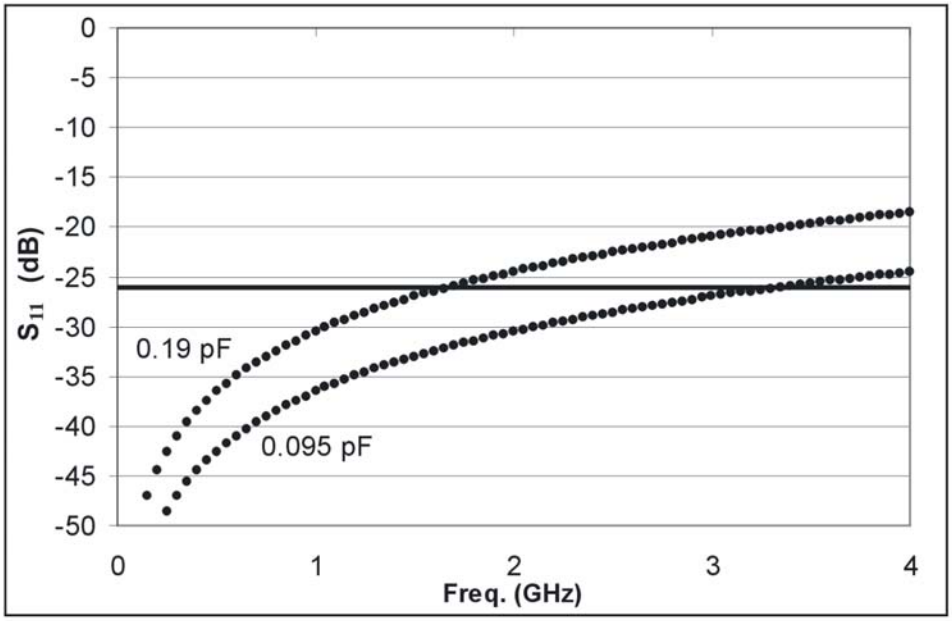

Figure 3.11: Calculated reflection losses for the two floating-bridge designs.

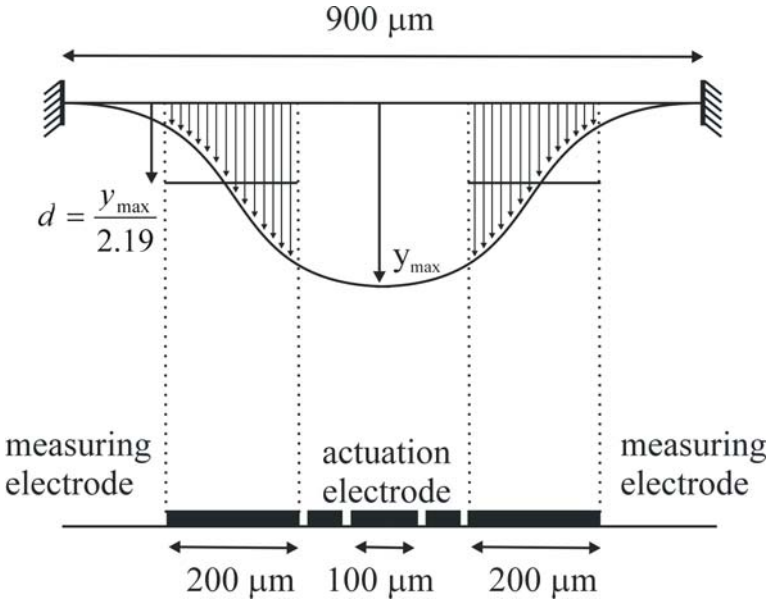

Figure 3.12: Drawing of the floating bridge showing the relation between the effective deflection on top of the measuring electrodes (d) with respect to the maximum displacement (y_{max}).

Figure 3.13 shows the calculated sensitivity for the two different floating bridges as a function of the residual stress on the structural material (left y-axis). The thickness of the bridge and the gap between the bridge and the signal line were

assumed to be 1 μm. As we did for the case of the grounded bridges, a secondary axis has been added showing the expected capacitance change at the maximum RF power level possible to deliver by the equipment used (0.08 W).
As can be observed, the sensors are rather sensitive with capacitance changes in the order of several fF ever for the higher values of residual stress. Measurement of such relatively large changes in a floating capacitor should be no problem.

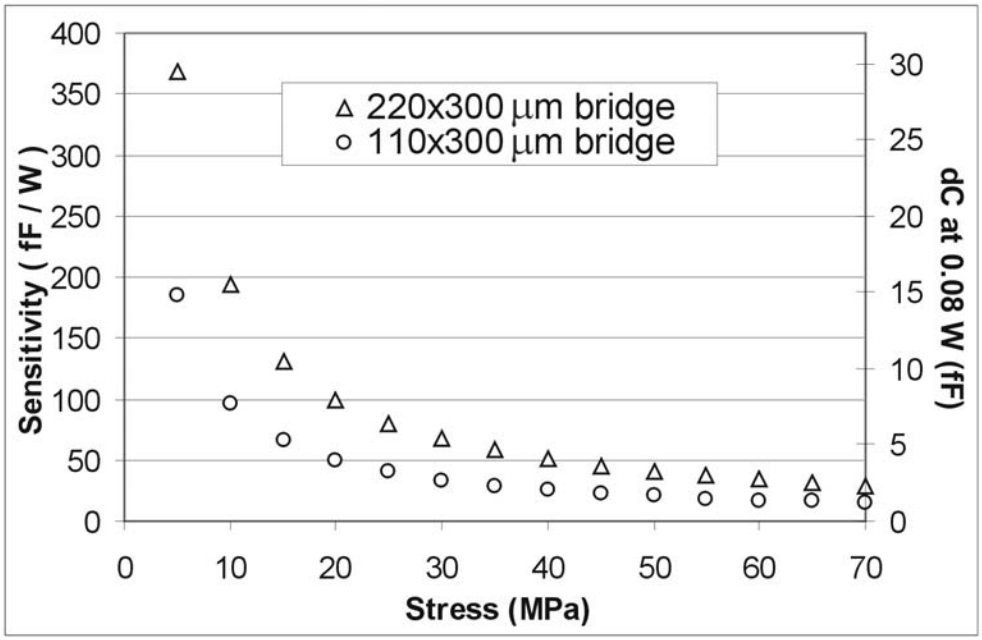

Figure 3.13: Calculated influence of the residual stress on: sensitivity of the sensors (left y-axis), and expected capacitance change at the maximum power delivered by the power source, 0.08 W (right y-axis).

3.4 RF compensation to increase the bandwidth

As discussed in Chapter 2, the RF performance of the sensor can be improved by tuning the dimensions of the CPW lines around the sensor within an area much smaller than the wavelength of the frequencies of interest. In this way, lower reflection losses than those expected from the extra capacitance value introduced by the sensor can be achieved.
In this section we will introduce two different ways of impedance compensation.

a) Reducing the width of the signal line
b) Partly removing ground lines

In both cases, the gap distance of the CPW is increased. As a result, lower capacitance and higher inductance are obtained in that region, thus compensating for the extra capacitance added by the sensor.

3.4.1 Reducing the width of the signal line

Figure 3.14 shows the detailed design and dimensions chosen for the realization of this impedance matching method. In this case, the central line width of the CPW is reduced over a distance d, resulting in a larger gap distance g. As a consequence, total shunt capacitance on the transmission line is reduced over a certain length, and series inductance is increased.

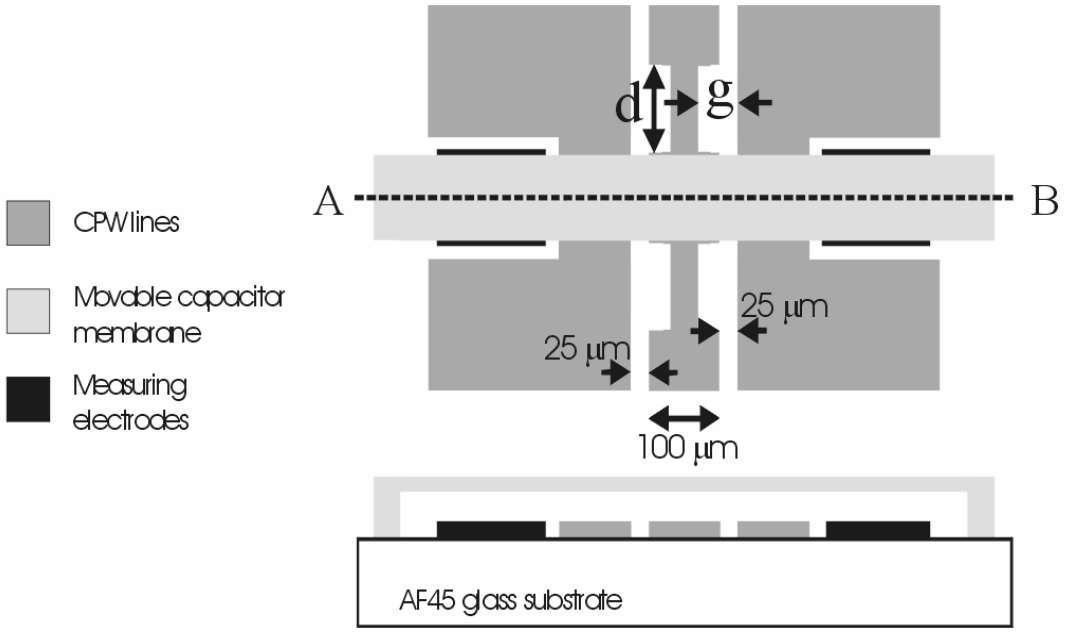

Figure 3.14: Schematic overview of a compensated floating rf power sensor design by reducing the width of the signal line (top view and cross section).

In order to verify the correct operation of this method, simulations were performed using SONNET v10.52 [12]. The results are shown in Figure 3.15. As can be observed from the simulation results for the magnitude of the S_{11} parameter shown, closer impedance to the desired 50 Ohm, and therefore a better match, is obtained when the width of the central line of the CPW is reduced. This confirms that the technique really results in a compensation for the extra capacitance. As a drawback, we can also observe that although reflections are lowered, the transmission losses (magnitude of S_{21}) increase when the signal line becomes too narrow (W=30 µm). This is as a consequence of the higher resistance introduced into the line, since the dimensions of the metal line which carries the RF current have been considerably reduced. Nevertheless, the magnitude of the S_{21} parameter

remains rather low, making it worthwhile to use this technique as a compensation method.

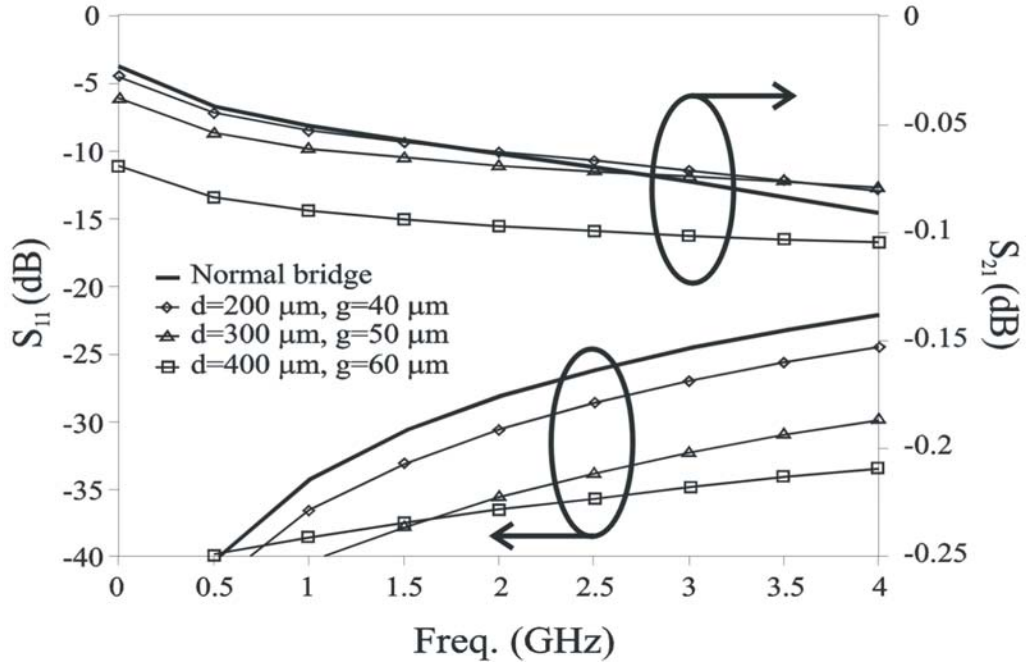

Figure 3.15: SONNET v10.52 simulation results for different designs of a compensated bridge sensor changing the width of the central line.

3.4.2 Partly removing ground lines

Figure 3.16 shows the detailed design and dimensions chosen for the realization of this impedance matching method. In this case, the ground lines are partly removed starting from the closest edge to the central line of the CPW along a distance d, giving a new gap distance g. Similar to the previous case where the width of the central line is changed, the shunt capacitance on the transmission line is reduced and series inductance is increased, and a better match is obtained. The larger gap distance also provides ample room for the sensing electrodes, so in this design the electrodes are again positioned between the signal line and ground lines.
Simulations performed with SONNET v10.52 show that also this method provides good compensation and reflections losses are reduced significantly as can be seen in Figure 3.17. Moreover, it can be seen that the transmission losses decrease too. Only in the case where the ground lines become extremely narrow (g=250 µm) the transmission losses do not show any further improvement due to the extra resistance induced. In summary, results indicate that not only reflection but also transmission losses can be optimized with this impedance matching method.

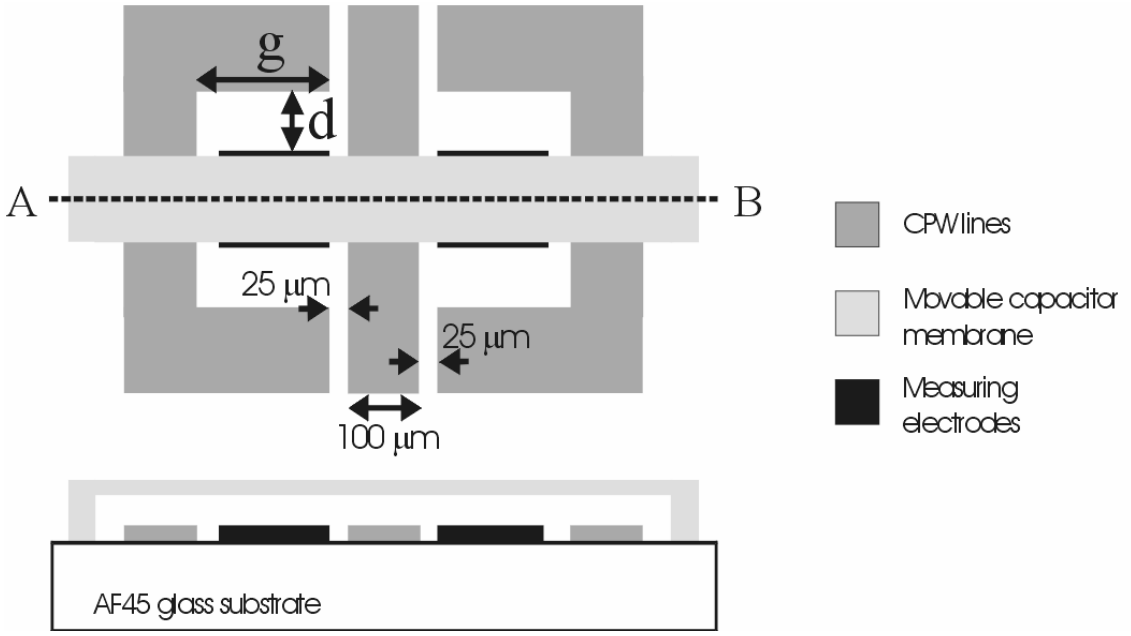

Figure 3.16: Schematic overview of a compensated floating rf power sensor design by moving ground lines apart (top view and cross section).

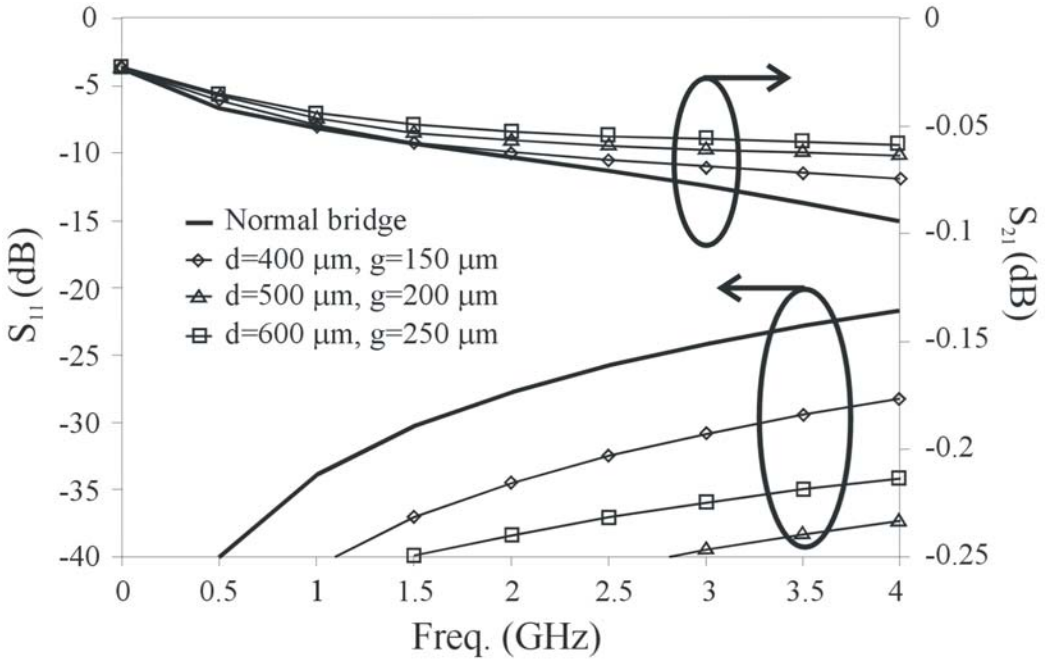

Figure 3.17: Simulation results for different designs of a compensated bridge sensor changing the width of the central line.

3.5 Conclusions

Most relevant aspects regarding the final design of a transmission line were discussed, and chosen dimensions where shown. For the realization of the bridge, two different types regarding its connection to the CPW (grounded and floating) were treated separately. Final dimensions of the sensors were presented, and expected RF and mechanical behavior were estimated and discussed. Results indicate that an RF power sensor based on a bridge design with capacitive readout up to 4 GHz is feasible. Finally, the design of two compensation techniques on the CPW (reducing width of the signal line and partly removing ground lines) in order to increase the bandwidth of the sensor were presented and discussed. Simulated results from SONNET v10.52 confirmed the operation of these methods, indicating a further improvement in the frequency bandwidth of the sensor.

3.6 References

[1] Jackson J. D., *Classical Electrodynamics*, John Wiley & Sons, Inc., 1999.

[2] Pozar D.M., *Microwave engineering*, 3rd ed., John Wiley & Sons, Inc., 2005.

[3] http://www.schott.com/fpd/english/products/fpd/af45.html

[4] Henri Jansen, Sayanu Pamidighantam, Walter De Raedt, Giuseppe Beccarini, Orsola Dimonaco, Kris Baert, and Harrie A. C. Tilmans, "Micromachined Devices for Space Telecom Applications", *Proc. 3rd Round Table on Micro/Nano-Technologies for Space*, ESTEC, Noordwijk, The Netherlands, May 15-17, 2000, pp. 135-140. (http://www.techonline.com/community/ed_resource/feature_article/8077).

[5] X. Rottenberg, H. Jansen, P. Fiorini, W. De Raedt and H. A. C. Tilmans, "Novel RF-MEMS capacitive switching structures", *proc. 32nd European Microwave Conference*, 23-27 September 2002, Milan, Italy, pp. 809-812.

[6] Sayanu Pamidighantam, Robert Puers, Kris Baert and Harrie A C Tilmans, "Pull-in voltage analysis of electrostatically actuated beam structures with fixed–fixed and fixed–free end conditions", *J. Micromech. Microeng.* 12 (2002) 458–464.

[7] Harrie A.C. Tilmans, Rob Legtenberg, "Electrostatically driven vacuum-encapsulated polysilicon resonators. Part II: Theory and performance", *Sensors and Actuators A*, 45, (1994), 67-84.

[8] Roark R.J. and Young W.C., *Formulas for Stress and Strain*, New York: McGraw-Hill, 1989.

[9] Harrie A.C. Tilmans, "Micromechanical sensors using encapsulated built-in resonant strain gauges", Ph.D. dissertation, Faculty of Electrical Engineering, University of Twente, 1993.

[10] I.H. Shames and C.L. Dym, "Energy Methods and Finite Element Methods in Structural Mechanics", McGraw-Hill, New York, 1985, Chs. 3 and 7.

[11] L. Meirovitch, "Elements of Vibration Analysis", McGraw-Hill, New York, 1975, Chs. 1 and 5.

[12] http://www.sonnetsoftware.com/

Chapter 4

Fabrication

4.1 Introduction

In this chapter, the fabrication process of the RF MEMS power sensors is presented. First, the reasons which made us choose for aluminum surface micromachining on an AF45 glass substrate [1] will be explained. Next, the suitability of different sacrificial layer materials will be discussed, and the choice for photoresist is explained. Finally, successful fabrication results for the two different RF MEMS power sensor designs will be presented together with the final process outlines.

4.2 General fabrication aspects

4.2.1 Substrate material

Of course for MEMS devices an obvious choice for the substrate material would be silicon. Silicon has several advantages. It is compatible with various well-developed fabrication processes, doped silicon can be used as electrode and it is even possible to have integrated electronics on the same substrate, which can be an advantage when sensing small capacitance changes. Nevertheless, an important

source of losses in a transmission line (apart from the resistive losses in the metal lines already treated in Chapter 3) is the so-called 'conductance' loss in the dielectric material. Up to now, we have considered the CPW using a perfect dielectric as a substrate, so that the capacitance between signal and ground lines did not introduce any loss mechanism. But real capacitors have losses, which depend on the frequency. Usually a complex capacitance $C' = C(1 - j\tan\delta)$ is defined (see Appendix B), where tan δ is called the *loss tangent* or *dissipation factor* of the capacitor. Now, the current between the lines can be written as $I = jwC'V = (jwC + wC\tan\delta)V$. The first term is the current through an ideal capacitor C, leading the voltage by 90°. The second term is in phase with the voltage, and gives an energy loss. Therefore, materials with low $\tan\delta$ should be used as substrate material in order to reduce this loss source.
To get an estimate of how important substrate-related losses would be for the power sensor designs, CPW transmission losses were measured with a vector network analyzer for different substrate materials: AF45 (special glass for microwave), p-doped silicon wafer (5-10 Ω cm) and p-doped silicon wafer with 1.5 μm silicon nitride layer on top. Figure 4.1 shows the experimental data from the $|S_{21}|$ parameter for the different materials. As expected, the highest losses are obtained for the highly-doped silicon substrate. A slightly better result is found when a layer of 1.5 μm silicon nitride (SiN) is deposited between the substrate and the metal lines, since SiN has very low tan δ (4-9 10^{-4}). Nevertheless, too high losses are obtained due to the low thickness of the SiN layer, so that the silicon is still dominant in the RF behavior of the substrate. The reason why deposition of thicker SiN was not tried is that this would result in very high tensile stress resulting in cracks in the SiN layer. In Chapter 6 we will present a technique to create thick 'SiN blocks' (in the order of tens of μm) in the surface of highly-doped silicon wafers. In this way, the fabrication of CMOS electronics and RF MEMS devices without high transmission losses in the same substrate is possible. Finally, it can be observed from Figure 4.1 that the AF45 glass substrate induces almost no transmission losses. Therefore, while the creation of thick SiN blocks on highly doped silicon wafers was not yet available, AF45 substrate was chosen for the fabrication of the RF MEMS power sensors.

4.2.2 Surface micromachining

Once the AF45 glass substrate was selected, a surface micromachining process was chosen for the fabrication of the movable capacitor. The next step is to select suitable materials for the movable plate and the sacrificial layer.

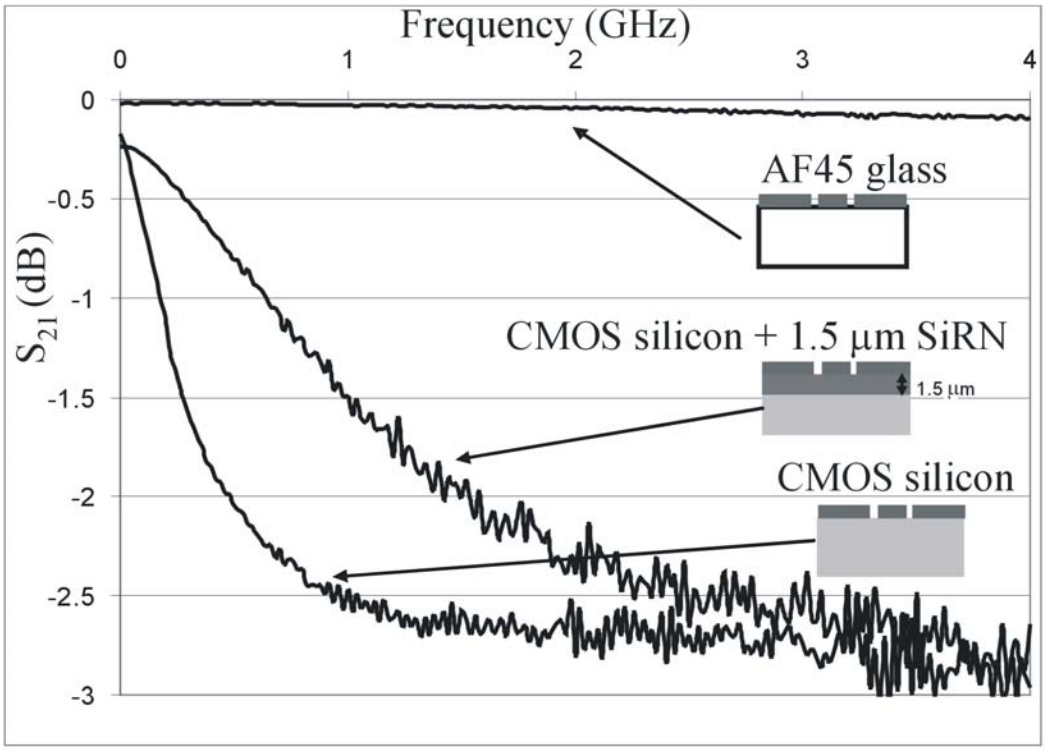

Figure 4.1: $|S_{21}|$ parameter measurements for 3 different substrate materials.

Structural material

Aluminum was the material chosen as the structural material for the movable plate. Using only aluminum for the fabrication of the bridge, instead of using a combination of two different materials (for mechanical support and for electrodes), we improve the temperature properties of the sensor. At the same time, Aluminum guarantees very good electrical properties, and, since the strain is very small, good mechanical behavior can be expected. Furthermore, RF MEMS switches have already been successfully fabricated with aluminum surface micromachining [2-5], where mechanical and electrical requirements are much higher than in the case of the realization of an RF MEMS power sensor. Therefore, aluminum as structural material is a good choice for the fabrication of the sensor.

Sacrificial layer

The main characteristics required for the sacrificial layer are the control of the thickness, stability to support the further process steps, and the selective etching with respect to the structural material. Two different materials were considered: sputtered amorphous silicon and photoresist.

Amorphous silicon

Figure 4.2 shows the basic process flow for the case of using amorphous silicon as the sacrificial layer material. First the silicon is sputtered on the wafer at the desired thickness (1). Then, patterning of the sacrificial layer is performed using the BOSCH process [6] using photoresist as a mask (2). Once the aluminum structural material is deposited and patterned (3), the amorphous silicon layer is removed selectively using SF_6 plasma etching (4).

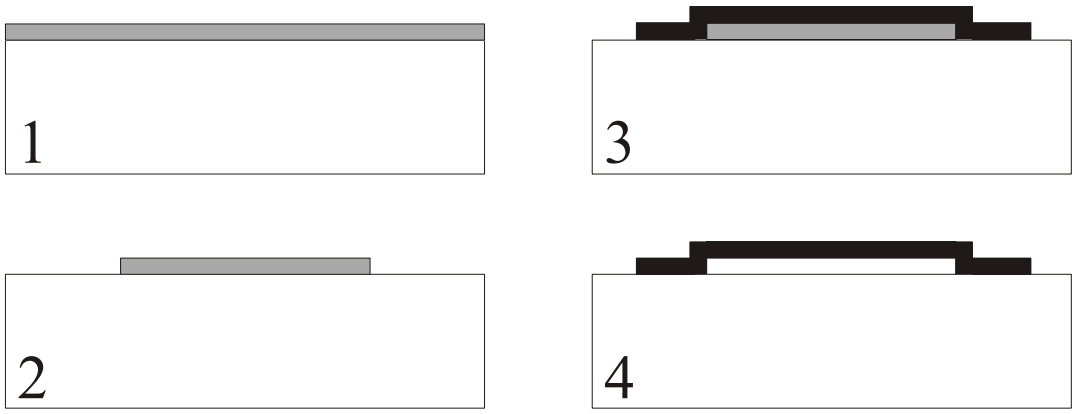

Figure 4.2: Process flow of the power sensor using amorphous silicon as sacrificial material using BOSCH process for patterning.

Figure 4.3 shows the fabrication results of bridge test structures. As can be observed, a rather rough aluminum layer is obtained most probably due to the high sputtering power parameters. This could be solved by optimizing the sputtering settings, however a much more concerning effect is obtained at the clamp points of the movable plate. As can be observed from Figure 4.3(b), a very bad connection between the two different levels of the structural material is obtained due to the sharp edges of the amorphous silicon. As a consequence, the beams from all bridge designs collapsed to the bottom substrate.

In order to decrease the sharpness at the edges of the sacrificial material, wet chemical isotropic etching (TMAH) could be used for the patterning of the amorphous silicon. The process flow in this case is shown in Figure 4.4.

It can be observed that edges are softer, and a better defined membrane is obtained. Nevertheless, as a consequence of the isotropic profile, you always end up with a 90 degrees slope at the top of the layer. Moreover, if the etching is slightly overdone, the isotropic profile disappears and again vertical edges are obtained [7]. In order to overcome these problems, photoresist as a sacrificial layer was considered.

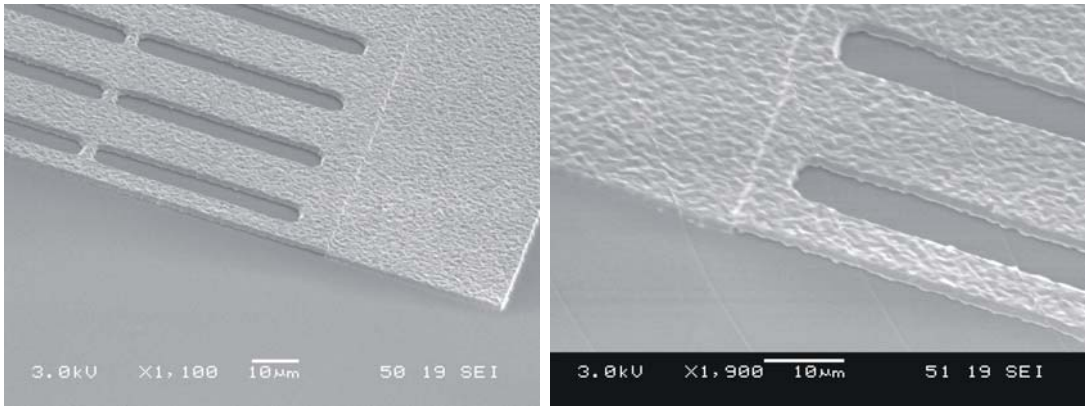

(a) (b)

Figure 4.3: SEM pictures of test bridges with amorphous silicon as sacrificial material.

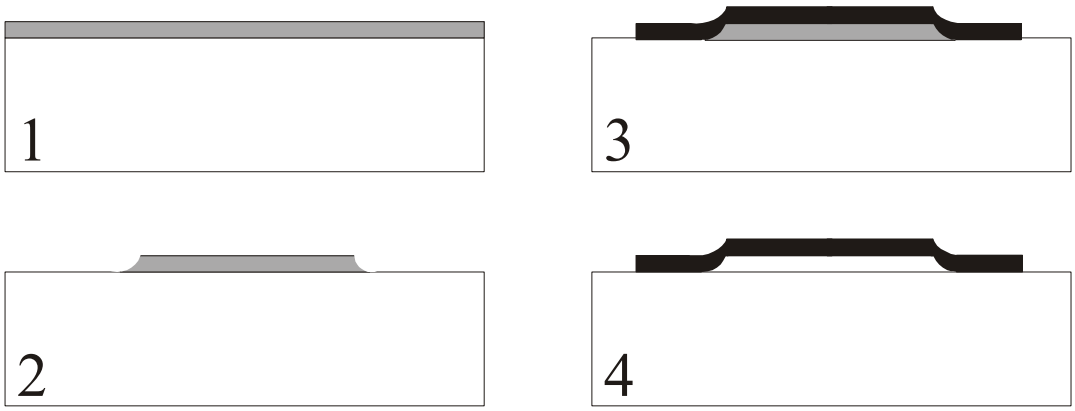

Figure 4.4: Process flow of the power sensor using amorphous silicon as sacrificial material using wet chemical etching for patterning.

Photoresist

Photoresist as a sacrificial layer was proposed in order to overcome the problem caused by vertical edges. Although sharp edges are also obtained when photoresist is patterned by a standard photolithography process, a smooth profile can be created by exposing the polymer to high temperatures (100-180 C). This process step is called postbake. Figure 4.5 shows SEM pictures of two photoresist layers deposited and patterned one after the other. The first one, placed at the bottom, was exposed at 150 ° C after the lithography process, while for the second polymer, placed at the top, the postbake step was omitted. A layer of 5 nm aluminum was deposited at the end to make the photoresist visible by SEM.

The photographs clearly show that the photoresist layer without the extra postbake step has a vertical profile at the edges, while the polymer which has been exposed

to the postbake step shows round edges. This effect is especially notable in Figure 4.5(b), where both edges can be compared with each other.

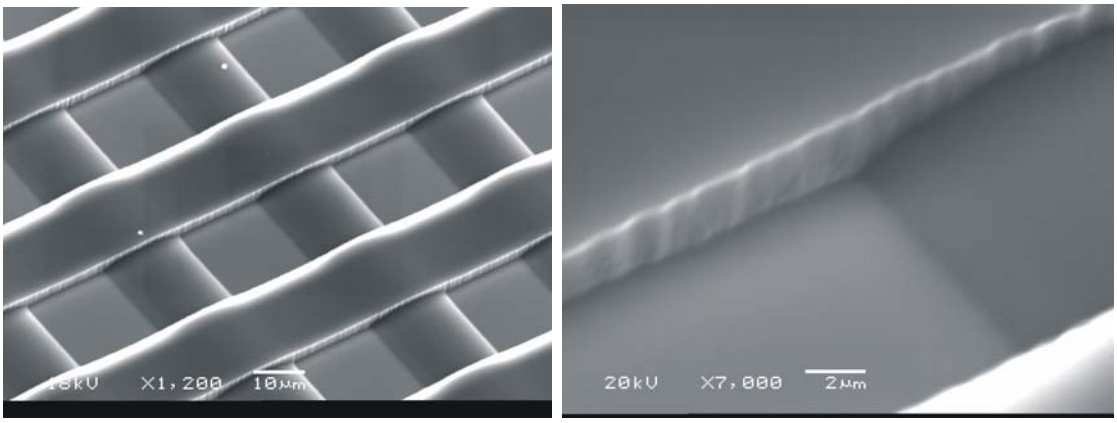

(a) (b)

Figure 4.5: SEM pictures of two different photoresist layers one deposited on top of the other. The first one (at the bottom) was exposed to a postbake, while that step was omitted in the second layer (at the top).

Figure 4.6 shows the different profiles obtained after an exposure at different temperatures during 5 minutes. Temperature values were tuned from 110 C until 170 ◦ C. It can be observed that there is a reflow of the photoresist, and that this reflow is temperature dependent.

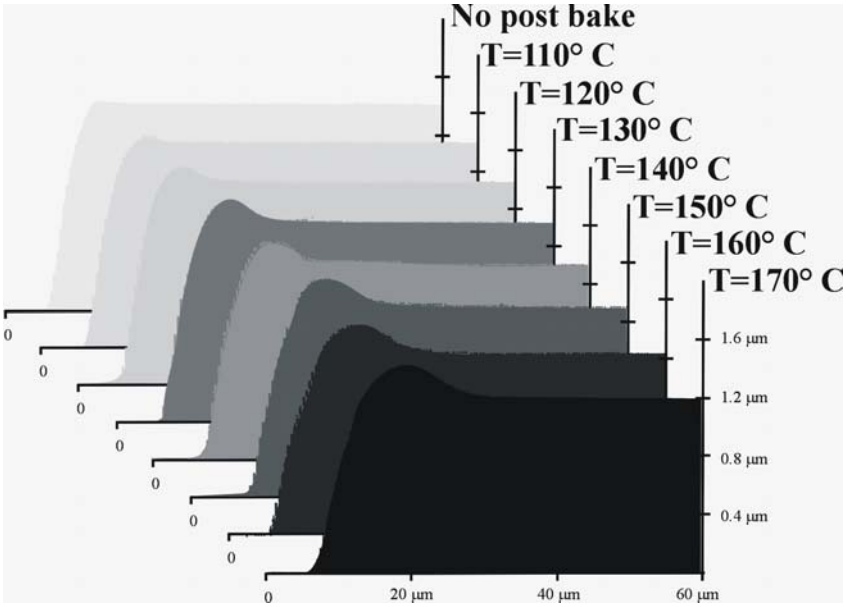

Figure 4.6: Measured profile of a photoresist layer with different postbake temperatures.

At lower temperatures (up to 130°C) a small bump appear at the edge of the polymer, which becomes larger when the temperature is increased (from 140°C) creating a soft profile. Another effect which is observed is the decrease in thickness of the polymer. Far from the edge, thinner photoresist can be clearly seen for postbake temperatures above 130°C. A possible explanation for this would be the evaporation of the solvents in the photoresist during the baking process. As a consequence, the sacrificial layer is expected to have the desirable edge profile and lower thickness.

The postbake exposure time was also studied. After applying a postbake step of 150 C during four different times, 2, 5, 10 and 30 min no change in the profile could be observed between them. With respect to the thickness, a decrease in thickness was found as time was increased. The thickness of the layer seems to be stable after 30 minutes, with a height difference of 200 nm compared to the profile obtained for only 2 minutes exposure time.

A temperature of 150°C was selected for the postbake step in our process, since no relevant changes were observed for higher temperatures. A duration of 30 minutes was chosen in order to be sure that all solvents would be evaporated and the photoresist would be hard enough to withstand the sputtering process which needs to be performed on top of it.

The process flow when photoresist is used as a sacrificial layer is shown in Figure 4.7. After patterning the sacrificial layer with standard lithography (1), a thermal reflow of the photoresist is performed as indicated previously (2). Then, the aluminum structural material was sputtered using the lowest power level available in the system (500 W), since otherwise photoresist becomes too hot, producing bubbles or even burning during the process. After patterning the bridge structural material using photoresist as a mask (3), oxygen plasma is used to remove selectively the photoresist sacrificial layer (4).

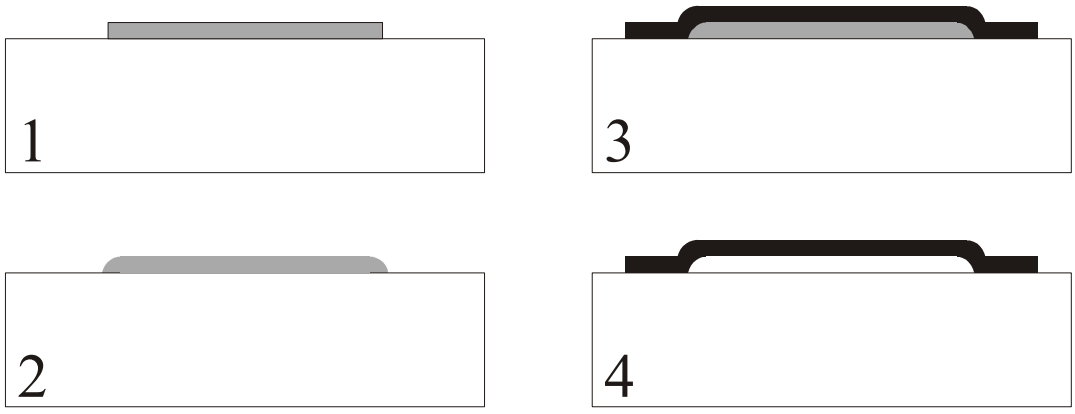

Figure 4.7: Process flow of the power sensor using photoresist as sacrificial material.

Figure 4.8 shows the fabrication results of bridge test structures. It can be observed that, as a consequence of the lower power used for the sputtering, the roughness of the aluminum was considerably reduced compared to the results shown in Figure 4.3. And more important, the smooth edges of the photoresist allowed a smooth transition of the aluminum layer from the wafer to the bridge, resulting in a strong mechanical connection of the two levels and successful fabrication of the beams. It can be also observed how the profile of the resist is transferred to the beam, decreasing the gap distance in the middle of the bridge related to the one at the edges. Nevertheless, this effect seems to be stronger than expected from the effect of the photoresist. Therefore, effects on the shape of the bridge caused by the stress will be studied in the next section.

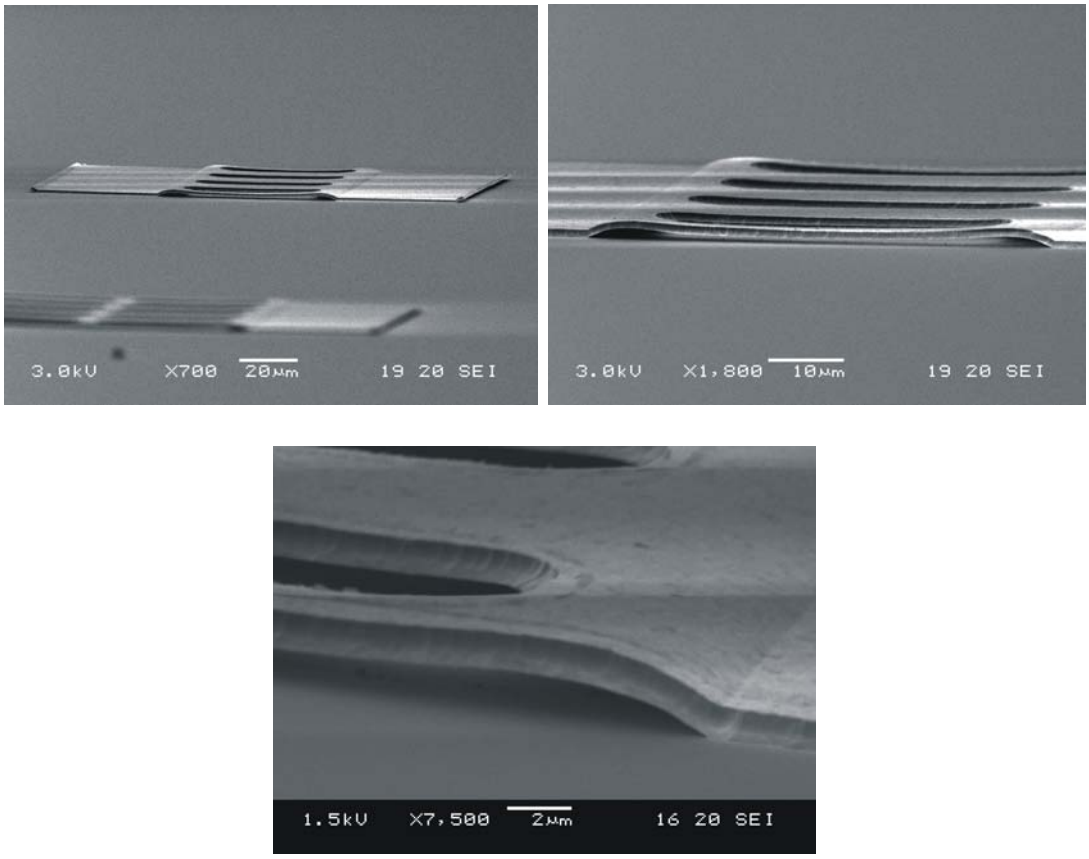

Figure 4.8: SEM pictures of the test bridges with photoresist as sacrificial material.

4.2.3 Residual stress

As said in the previous section, a lower gap than expected can be observed in the middle of the structure. A close look at Figure 4.8 reveals that a gap in the order of 1 µm is obtained, being even lower than expected from the effect of a postbake

step on the photoresist. A possible explanation could arise from the presence of a tensile stress on the aluminum layer. When a tensile stress is present at the clamp areas of a beam (see Figure 4.9(a)), a tilting of the vertical walls placed at the edges is produced, ending in a downwards deflection in the middle of the structure (see Figure 4.9(b)).
In order to eliminate the induced stress in the aluminum, we could tune the sputtering conditions until the optimum sputtering settings are found. Nevertheless, the use of photoresist as a sacrificial layer forced us to use an specific sputtering system where, although its minimum power deposition (500 Watt) does not damage the photoresist, no other parameters were allowed to be tuned. Therefore, no optimization of the deposition parameters could be done. An estimation of the induced stress is then required to know if the aluminum layers are acceptable for the fabrication of the power sensor.

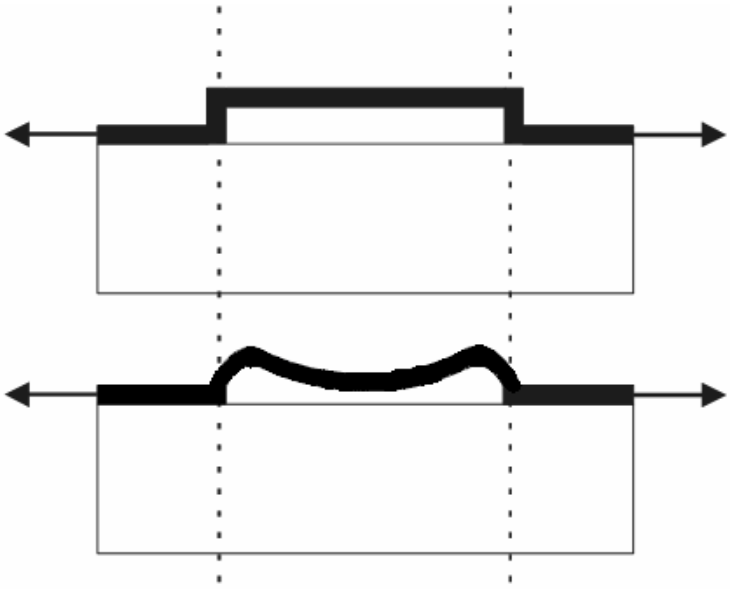

Figure 4.9: Schematic, exaggerated impression of the effect of tensile stress on a free standing bridge with steps at the edges.

To estimate the stress in our layer, measurements of the curvature of the substrate due to the presence of the layer were performed. The relation between the bending of the substrate and the stress of the deposited film can be found using Stoney's formula [8-9]:

$$\sigma = \frac{4}{3}\frac{E_s}{1-\nu_s}\frac{h_s^2\delta}{D^2 h_f} \qquad (1)$$

where σ and h_f are the residual stress and thickness of the aluminum layer, E_s, ν_s and h_s are the Young's modulus, poisson ratio and thickness of the substrate, and δ represents the deflection at the center for a surface scan of a distance D. Using this formula, two different ways of deposition were compared. The first one is by depositing the film on a single step. In this case, the continuous increase of temperature during deposition could induce higher values of stress on the layer. The second case is the deposition of the layer in multiple smaller steps, giving time to the substrate to cool down in between. In this way, better results could be expected caused by the lower and more homogeneous temperature of the structural layer during the sputtering process. Table 4.1 provides a summary of the results.

Layer thickness	Stress
1000 nm	+79.0 MPa
250 nm	+48.9 MPa
250 + 250 nm	+35.4 MPa
250 + 250 + 250 nm	+35.2 MPa
250 + 250 + 250 + 250 nm	+36.0 MPa

Table 4.1: Measured stress values of sputtered aluminum layer.

The measurements show an always tensile stress, which could explain the presence of lower gap values as explained in the beginning of this section. It can be also observed that lower values of stress are obtained when deposition is performed in four steps of 250 nm deposition each. Moreover, the similarity of the stress measured on the four different steps indicates that stress gradient keeps being low. Therefore, the sputtering of the aluminum structural layer in small steps was chosen for the fabrication of the bridge.

4.3 Fabrication of a grounded bridge

The process flow used for the fabrication of the grounded bridge is shown in Figure 4.10. As discussed, AF45 glass wafer was used as a substrate. As a first process step, 1 μm thick aluminum layer is sputtered and patterned, which creates the CPW lines and measuring electrodes (1). After that, 1.7 μm thick photo-resist (Olin 907-17) is deposited and patterned in order to use it as a sacrificial layer (2). A baking step at 150 C during 30 minutes is then performed in order to obtain smooth edges. At the same time, the polymer is prepared for the sputtering process which needs to be performed on top of it. A layer of 1 μm thick aluminum is then deposited by low power sputtering (500 Watt) in four steps of 250 nm each and patterned (3). The patterning of the aluminum is done using phosphoric acid after a layer of photoresist has been deposited and patterned on top by standard photo-

lithography, giving to the membrane the wanted shape and creating slits in order to help during the sacrificial layer etching (etching holes). Finally, the membrane is released by oxygen plasma etching of the resist (4).

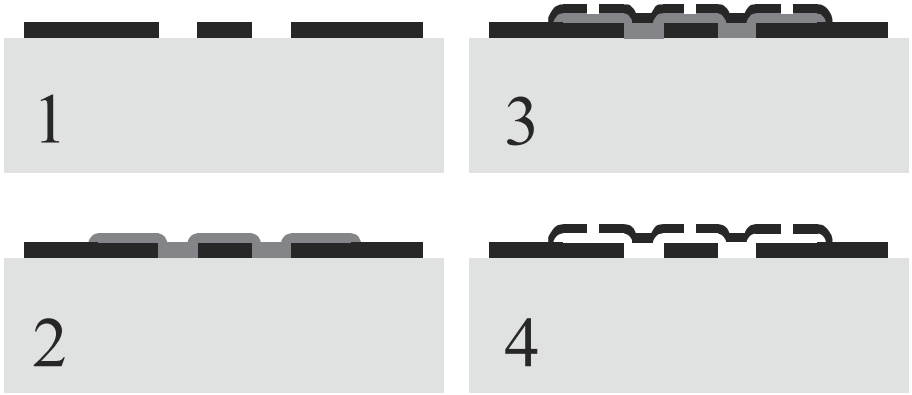

Figure 4.10: Outline of the fabrication process for the grounded-membrane sensor structure. In this case no attempt was made to obtain an extremely flat membrane.

Figure 4.11 shows SEM pictures of the fabrication results. Free standing bridges are obtained on top of the CPW as a consequence of the successful fabrication process. From Figure 4.11(b), we can see that the pattern of the CPW has been transferred into the bridge (see also figure 4.10.4), which could cause a physical connection between the bridge and the edges of the CPW lines. Nevertheless, no touching points were observed for the design parameters of the grounded bridges (300 μm long beams). But special attention in the planarization of the photoresist will be needed for the designs with longer beam dimensions, where initial deflection of the beam could be higher, ending with a short circuited structure.

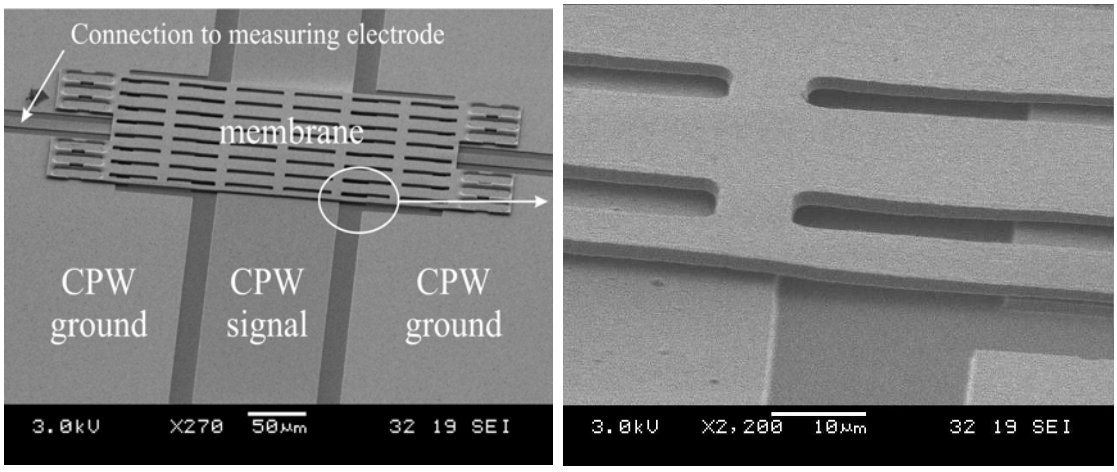

(a) (b)

Figure 4.11: SEM photographs of a fabricated grounded-membrane sensor. The close-up clearly shows the curvature of the membrane due to the underlying CPW structure.

4.4 Fabrication of a floating bridge

As discussed in Chapter 3, longer and more challenging designs of the bridge are going to be fabricated with the floating bridge sensor. Therefore, the development of a process outline to overcome the possible touching between the bridge and the CPW as illustrated in the previous section is required. Since the problem is caused due to the transfer of the CPW shape into the beam, a process where the transmission lines are embedded into the glass substrate is proposed as a solution. Figure 4.12 shows the process flow used for the floating bridge. First, photoresist is deposited and patterned, removing the polymer from the places where the CPW and measuring electrodes will be placed (1). Next, 1 μm deep recesses are etched into the glass substrate by 1% HF solution (2). Then, 800 nm of aluminum is deposited by sputtering (3). Removing the photo-resist results in lift-off of the aluminum layer, giving an almost flat substrate with the coplanar waveguide and sense electrodes embedded in the surface (4).

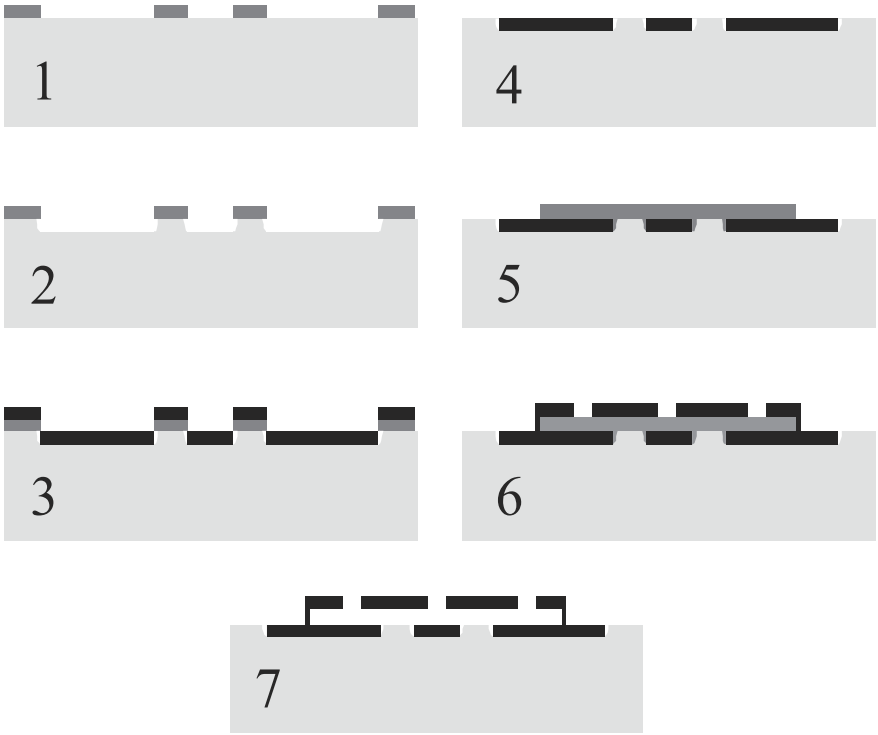

Figure 4.12: Outline of the fabrication process for the floating-membrane sensor structures. The CPW is embedded in the substrate to obtain a really flat membrane.

In this way, the same photoresist layer is used as a mask for the etching of the substrate and for the patterning of the material which needs to be placed in the cavities, resulting in a very simple and accurate process. A 200 nm difference

between the cavity depth and the aluminum thickness was taken to ensure no contact between the two metal levels, avoiding problems during the lift-off process. Then, a photoresist sacrificial layer is deposited and patterned (5). After a baking step of the polymer to obtain smooth edges, an aluminum layer of 1 μm thick is deposited in four steps of 250 nm each and patterned by phosphoric acid using an extra photoresist layer as a mask (6). Finally, the release of the bridge is performed by oxygen plasma etching. Microscope pictures with the fabrication results for the two different kinds of impedance matching techniques are shown in Figure 4.13.

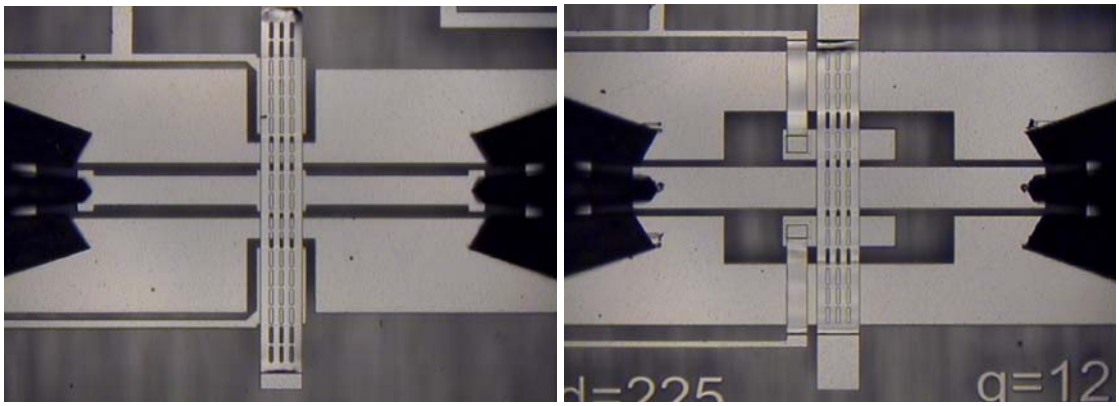

(a) (b)

Figure 4.13: Microscope pictures of fabrication results for a floating power sensor: a) sensor with central line dimensions of the CPW changed (see Figure 3.8), and b) sensor with ground planes moved away (see Figure 3.10).

As can be observed from the SEM picture presented in Figure 4.14 (a), a very flat bridge is created on top of the CPW as a result of the embedding of the lines. Figure 4.14 (b) shows the result of a white light interferometer measurement along the length of the beam. It can be observed that only 200 nm height difference is found within the bridge length. The peaks obtained were measured on top of the gap areas of the CPW. This is caused by the difference in high between the cavity depth (1000 nm) and the refilling aluminum layer (800 nm), which is transferred into the beam.

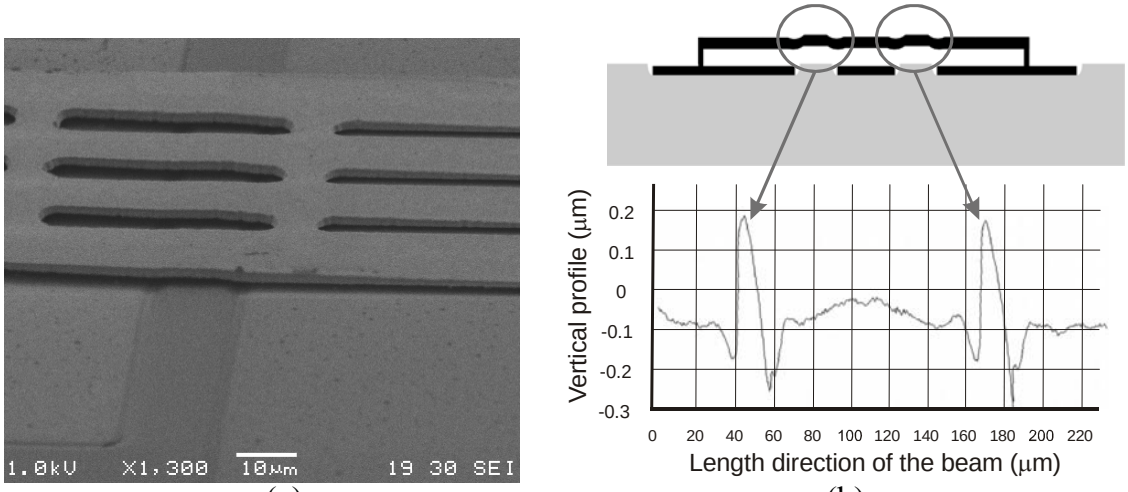

(a) (b)

Figure 4.14: a) SEM picture showing cross section of a floating sensor with embedded CPW, and b) white-light interferometer measurement showing the effectiveness of embedding the CPW in the substrate.

4.5 Conclusions

The fabrication of two different RF power sensors is presented in this chapter. Aluminum surface micromachining using AF45 glass as a substrate material was chosen because of the excellent RF properties that can be obtained. A problem with aluminum surface micromachining is the residual stress in the aluminum. The lowest stress ($\cong$ 35 MPa) in the aluminum structural material of the bridge was found for the case where the 1 µm thick layer was sputtered in four steps of 250 nm each. For the case of the grounded bridge, the different layers used for the fabrication of the sensor were directly deposited on top of the substrate (CPW lines - sacrificial layer – bridge). Successful fabrication of the 300 µm long grounded sensors is reported, although pattern transfer from the CPW lines to the bridge was observed. The topology observed in the bridge could result in a physical connection between the bridge and the CPW lines for longer bridge designs. Therefore, a new fabrication process was chosen for the fabrication of the floating bridge sensor, which involved a bridge design that was three times longer (900 µm). In the new process, embedding of the CPW lines into the glass substrate is performed, resulting in successful free standing bridges with very flat surfaces (height difference in the order of 200 nm).

4.6 References

[1] http://www.schott.com/fpd/english/products/fpd/af45.html

[2] Z. J. Yao, S. Chen, S. Eshelman, D. Denniston, and C. L. Goldsmith, "Micromachined low-loss microwave switches", *IEEE J. Microelectromech. Systems*, Vol. 8, pp 129-134, June 1999.

[3] S. Pacheco, C. T. Nguyen, and L. P. B. Katehi, "Micomechanical electrostatic K-band switches", *IEEE MTT-S International Microwave Symposium Digest*, Baltimore, MD, June 1998, pp. 1569-1572.

[4] J. B. Muldavin and G. M. Rebeiz, "High isolation MEMS shunt switches: Part 2: Design", *IEEE Trans. Mivrowave Theory Tech.*, Vol. 48, No. 6, pp. 1053-1056, June 2000.

[5] H.A.C. Tilmans, et al., "Wafer-Level Packaged RF-MEMS Switches Fabricated in a CMOS Fab", *IEEE IEDM Technical Digest*, Washington, pp. 921-924,2001.

[6] L'armer F and Schilp A Method of anisotropically etching silicon US Patent Specification 5501893, German Patent Specification DE4241045.

[7] Marvin Hutt and Walter Class, "Optimization and spacification of dry etching processes", *Solid State Technology*, March 1980.

[8] G. G. Stoney, Proc. R. Soc. London Ser A 82, 172 (1909).

[9] L. B. Freund and S. Suresh, "Thin film materials: stress, defect formation and surface evolution", *Cambridge University Press*, 2003.

Chapter 5

Measurement results

5.1 Introduction

The RF characterization and the RF power detection results are presented for the different designs of the grounded and floating bridge sensors. First, the *S*-parameters were measured in a frequency range up to 4 GHz. In this way, reflection and insertion losses coming from the sensor can be determined. Finally, the RF power sensitivity and resolution of the different sensor prototypes are presented. All measurements are compared to the theoretical expectations presented in previous chapters.

5.2 Transmission and reflection losses

In order to characterize the radio frequency behavior of the RF power sensor, *S*-parameter measurements up to 4 GHz were performed using a vector network analyzer (RF source: HP83651, Controller: HP8510C and test-set: HP8517B). Since aluminum was used for the fabrication of the CPW, measurements were performed using RF probes with sharp needle profile (G-S-G PICO probes 40A, CS-5 from GGB Industries Inc), capable of breaking the native aluminum oxide

layer, which typically grows at the surface of the metal. Therefore, stable and reproducible measurements could be obtained.
The calibration technique used was the so called SOLT (Short-Open-Load-Through) technique [1]. This method is known for its good performance in the frequency range of interest (up to 4 GHz). It consists of the measurement of short, open, 50 Ohm resistors and transmission lines on a calibration substrate (Agilent 85052B) in order to compensate for any non-idealities encountered in the setup.

5.2.1 Grounded bridge

As presented in the previous chapters, three different grounded bridge sensors were designed and fabricated. The only difference between them was the width of the beam, resulting in three different capacitance values of the sensor. Measurements of the S_{11} parameter magnitude expressed in dB for the three different sensors are shown in Figure 5.1, together with the results obtained on a simple CPW used as a reference (symbols). The results are compared with the expected behavior calculated in Section 3.3.1 and shown earlier in Figure 3.5 (lines).
In the case of the CPW alone, very low S_{11} parameter values were obtained for the whole frequency range. This confirms that the dimensions chosen for the transmission line resulted in an impedance which was slightly inductive and very close to the desired 50 Ohm (48.5 + 0.2 j Ω at 4GHz).
As can be observed from the measurement results shown in Figure 5.1, very high reflections are obtained for the two largest designs (3600x300 and 1800x300 μm bridge). These designs correspond to capacitances to the CPW in the order of 3.2 and 1.6 pF (see chapter 3). Reasonable reflection values are measured for the smallest sensor (200x300 μm bridge), which has a capacitance to the CPW of only 0.18 pF. The very good agreement between theory and measurement results shown confirms that the reflection characteristics of the grounded bridge power sensor can be modeled by using an equivalent shunt capacitor in the CPW. The capacitance value of this equivalent shunt capacitor can be deduced directly from the geometrical bridge dimensions of the sensor.
Figure 5.2 shows the measurement results of the S_{21} parameter magnitude measured on the smallest sensor and on a simple CPW used as a reference expressed in dB. As can be observed, the insertion losses for the simple CPW are in the order of -0.25 dB at 4 GHz, which means 0.045 dB/mm since the transmission line is 5.6 mm long. This value can not be explained by the reflection results shown in Figure 5.1, where only an effect of -0.0007 dB on the magnitude of the S_{21} parameter could be expected at 4 GHz. Therefore, we can conclude that resistive losses in the metal lines are the main source of the losses shown in Figure 5.2.

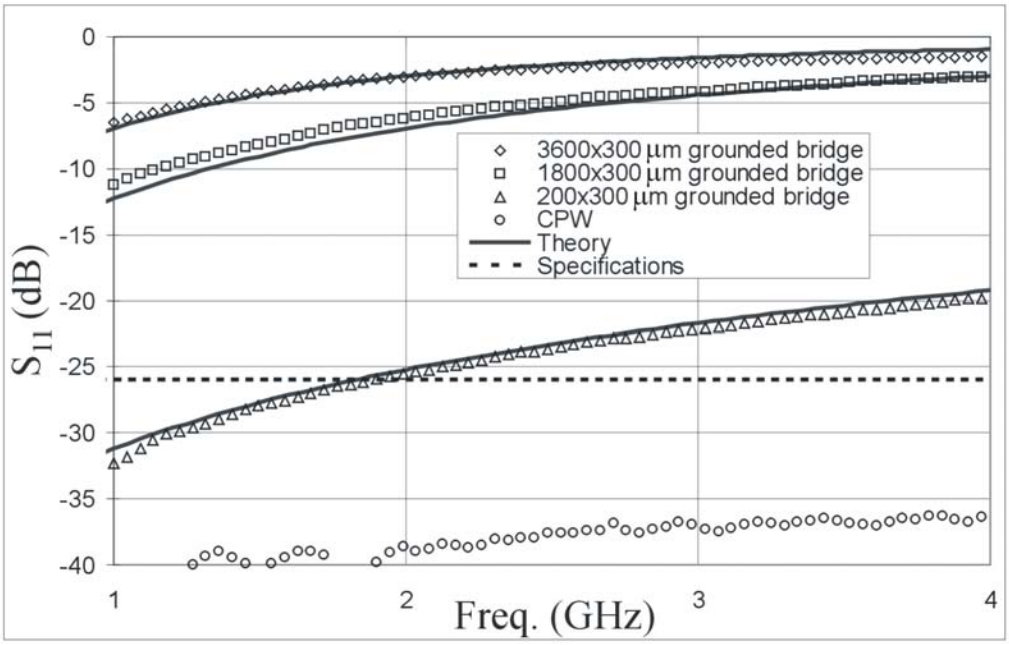

Figure 5.1: Measurements of the S_{11} magnitude expressed in dB on the three different grounded bridges designs compared to their theoretical expectations.

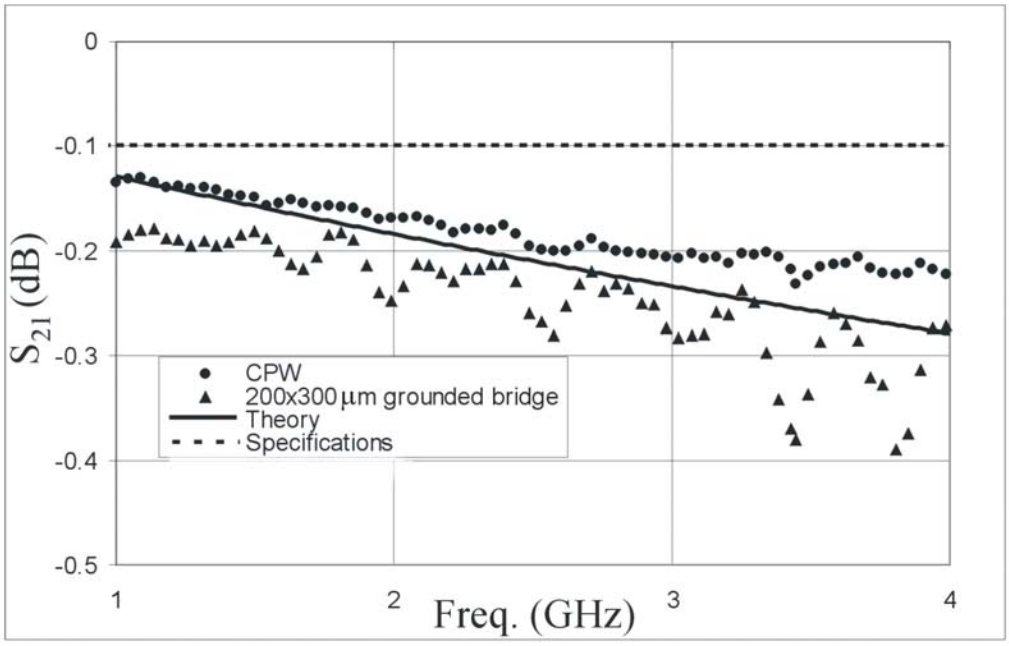

Figure 5.2: Measurements of the S_{21} magnitude expressed in dB on the CPW and the smallest bridge sensor (0.18 pF) compared to the theoretical expectations.

In Figure 5.2, only a small difference is observed between the insertion losses of the CPW and those of the smallest bridge. This is because the reflection losses of this specific design are small compared to the total transmission losses. The solid line in Figure 5.2 represents the sum of the measured insertion loss of the CPW and the theoretical contribution from the reflection losses caused by the smallest sensor shown in Figure 5.1. The measured losses are only slightly higher, showing a very good agreement between measurements and expected results. The wavy pattern obtained in the magnitude of the S_{21} values is due to difficulty of performing a perfect calibration when aluminum metal lines are used.
Figure 5.3 shows the measured values of the S_{21} magnitude expressed in dB for all three grounded bridge designs. As in the case of the smallest sensor shown in Figure 5.2, the lines represent the expected behavior calculated from the reflection losses of each specific sensor and the insertion losses measured on the CPW. Again, a very good agreement is observed; the measured losses are only slightly higher than expected. From Figure 5.3 we can observe that the deviation between theory and measurements increases with increasing bridge size. This effect is most probably due to the fact that most of the current will be running in the bridge instead of in the ground lines [2]. Therefore, the currents run along a longer path and, although the thickness of the metal is the same as in the CPW lines, higher resistance is expected as a consequence of the presence of etching holes in the bridge (see chapter 4).

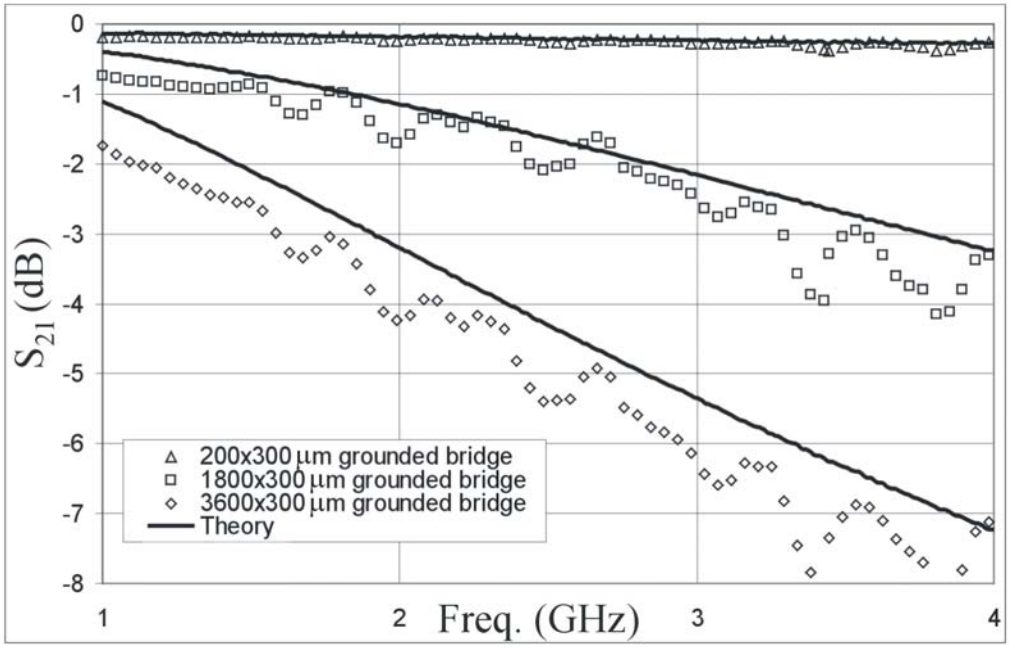

Figure 5.3: Measurements of the S_{21} magnitude expressed in dB on the grounded bridge sensors compared with the theoretical expectations.

From the measurement results we can conclude that a 6 dB decrease of the S_{11} parameter is still required in order to fulfill the target specifications of the sensor (see Figure 5.1). New sensor designs with lower capacitance introduced by the sensor, or the use of tuning techniques by the redesign of the CPW (see Chapter 2) are possible solutions to achieve the value of -26 dB for the S_{11} parameter specified in the target specifications.
Furthermore, a shorter CPW is needed in order to reduce the resistive losses, which are the main source of the total insertion loss of the sensor for a low reflection design (Figure 5.2). Since 0.04 dB/mm was measured for a simple CPW, the value of 0.1 dB for the S_{21} parameter mentioned in the target specifications should be reached by circuit lengths up to 2 mm.

5.2.2 Floating bridge

As presented in the previous chapters, two different floating bridge sensors were designed and fabricated in order to be able to improve the sensitivity of the capacitance read-out. Bridges with two different widths were fabricated, resulting in two different capacitance values which are related by a factor of two (see Figure 3.11). Smaller bridge dimensions were chosen in order to decrease reflections with respect to the grounded bridges, and the total length of the CPW was reduced to 1 mm in order to improve insertion losses.
Measurement results of the S_{11} parameter magnitude expressed in dB up to 4 GHz for the two different floating sensors are presented in Figure 5.4 together with a simple CPW used as a reference.
For the case of the CPW alone, it can be observed that slightly higher reflections are obtained compared to the previous results shown in Figure 5.1. The data obtained from the network analyzer indicates a slightly capacitive line, with an impedance of 51.4 - 0.5 j at 4 GHz. A slightly smaller gap than the targeted 25 μm would explain the impedance result of the CPW. Furthermore, since the CPW lines are now buried into the glass substrate, the relative amount of glass in between the signal and ground lines increases with respect to the case where metal lines are simple deposited on top of the substrate. As a consequence, an increase of the effective dielectric constant, and therefore of the shunt capacitance of the transmission line, is expected. Nevertheless, reflections are still quite low, although slightly higher than in the case of the CPW shown in Figure 5.1.

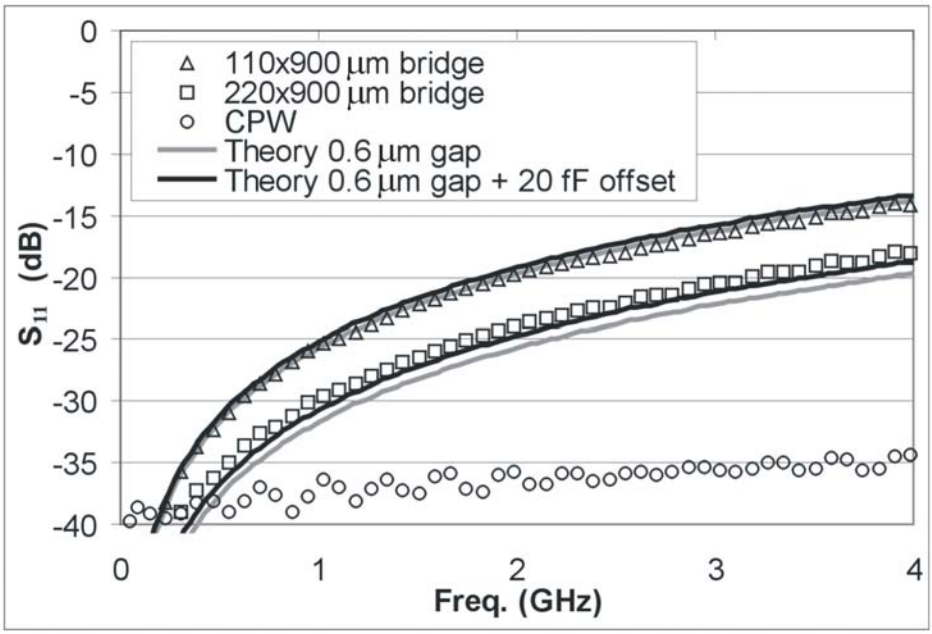

Figure 5.4: Measurements of the S_{11} expressed in dB on the CPW and the floating bridge sensors (symbols), compared with the theoretical expectations for a gap of 0.6 µm without any capacitance offset (black lines), and with 20 fF capacitance offset (gray lines).

For the case of the two different floating bridge sensors, measurements show considerable higher reflections than expected from Chapter 3, where a gap of 1 µm was assumed. Therefore, for the theoretical prediction shown in Figure 5.4 (black lines), a smaller gap of 0.6 µm was used. Then, a much better match between theory and experimental data is obtained, although for the smallest bridge (110x900 µm) a slight difference can still be observed. The fact that we need a smaller gap distance to obtain a good match can be explained from the increased length of the bridge. Due to the residual tensile stress in the bridge, the longer bridge with weaker spring constant will have a larger initial deflection than the shorter bridges used in the grounded bridge designs and a gap distance in the centre of the bridge in the order of 0.6 µm seems reasonable (see also Section 4.2.3 and Figure 4.9).
As indicated in Figure 5.4, an even better fit is obtained when 20 fF extra capacitance is added to the theoretical capacitance (gray lines). Such an additional capacitance improves the fit for the smallest bridge (110x900 µm) design but does not significantly change the RF behavior of the largest floating bridge (220x900 µm). It can be concluded that an offset of 20 fF capacitance added to the circuit gives a very good agreement between measurements and theoretical expectations. The origin of such an additional capacitance can be found in any parasitic

capacitance added to the signal line or in a deviation from the 50 Ω characteristic impedance due to non-optimal dimensions of the CPW.
Figure 5.5 shows the measured magnitude of the S_{21} parameter expressed in dB for the two sensor designs and a simple CPW. The result for a simple CPW shows that the insertion losses have been considerably reduced compared to the results obtained in the previous design (Figure 5.2). This is a direct consequence of the decrease in length of the circuit, which is now 1 mm long.
In the same graph, the insertion losses of the two different floating bridge sensor designs are shown together with the theoretically expected results, which are calculated based on the reflection losses already presented in Figure 5.4, and the measured insertion losses in the CPW. As in the case of the grounded bridge, slightly higher losses than expected are measured, probably due to the extra resistive losses caused by the currents in the bridge [3].

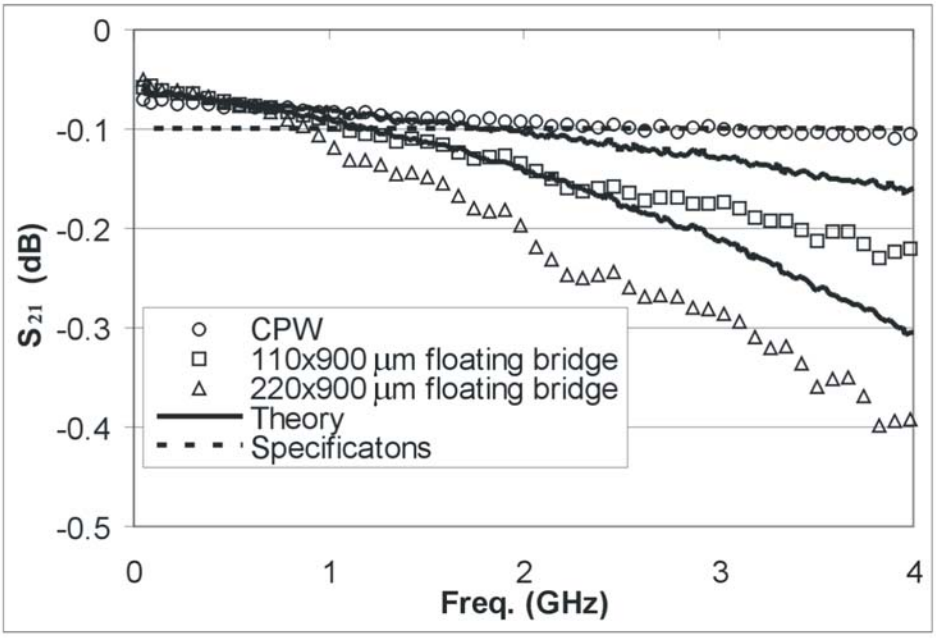

Figure 5.5: Measurements of the S_{21} parameter magnitude expressed in dB on the floating bridge sensors compared with the theoretical expectations.

Although slightly better results are obtained as a consequence of the new dimensions of the sensor and the CPW, still -0.2 dB insertion losses at 4 GHz for the smallest floating bridge sensor is obtained. Since 0.1 dB is the goal defined in the target specifications, further improvement is still required in the insertion losses of the sensor.
A new approach was presented in Chapters 2 and explained in detail in Chapter 3 based on changing the CPW dimensions just before and after the sensor bridge. The approach consists of tuning of the total impedance of the circuit by decreasing

the shunt capacitance and increasing the serial inductance of the CPW around the sensor device [4]. In this way, the extra shunt capacitance caused by the insertion of the floating bridge can be compensated. Two different approaches were tried, in both cases an increase of the gap distance between the signal and the ground lines of the CPW is realized in order to obtain the desired phenomena. In the first one, the width of the central line is reduced keeping the ground lines in the same position, while the other approach is based on removing part of the ground lines, moving them away from the signal line. The two different techniques were implemented on the small floating bridge designs (110x900 μm bridge).

Compensated circuit by reducing the width of the central line

In this approach the width of the central line is decreased, keeping the ground lines at their initial position. Figure 5.6 shows measured reflection losses for different width dimensions up to 4 GHz. The width of the central line is being reduced, increasing the distance to the ground lines from the initial 25 μm (100 μm wide signal line) up to 60 μm for the case of the smallest central line (30 μm wide signal line).
As can be observed, a lower S_{11} parameter is obtained when the gap of the CPW is higher, and/or the length for which the new gap is introduced increases. Therefore, it can be concluded that a better impedance match is obtained by decreasing the central line width of the CPW.

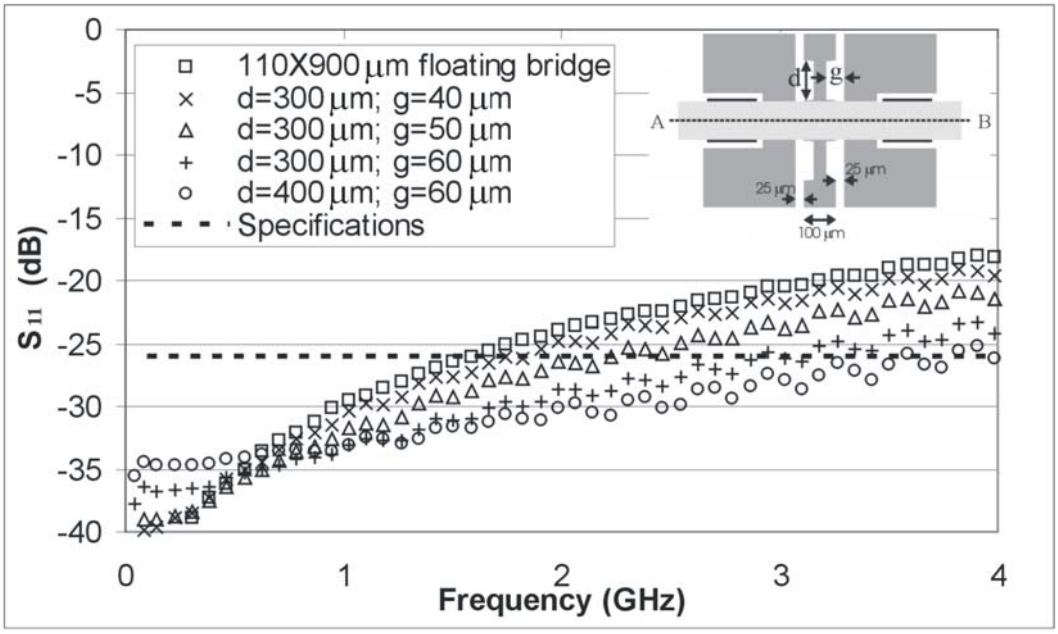

Figure 5.6: Measurements of the S_{11} on the floating bridge sensors with variations in the CPW dimensions for a better impedance match (reducing width of the central line).

The best match is obtained for the sensor where the maximum gap is created, (60 μm gap which corresponds to a 30 μm wide central line), for the longest distance (400 μm). In that case, the measured reflection losses are very close to the target specifications up to at least 4 GHz.
The measurement results of the insertion losses up to 4 GHz are shown in Figure 5.7. As can be observed, although lower reflections were obtained, higher insertion losses are measured. This response was already predicted by the simulations shown in Chapter 3. The smaller width of the signal line results in an increase of the resistance of the CPW, and therefore, in an increase of the insertion losses. The increase of the insertion losses of the different sensors is especially noticeable at the lowest frequencies, since at higher frequencies the increased insertion losses are compensated by lower reflection losses (which are the result of the better matching). As a consequence, the difference in the insertion losses between the different sensors reduces as frequency increases. From the measurement results we can conclude that, although further improvement seems to be possible in the reflections of the sensor by further decreasing the width of the central line, the extra resistance in the line makes it impossible to optimize both the reflection and insertion losses simultaneously. Therefore, the 0.1 dB insertion loss mentioned in the target specifications does not become feasible with this matching technique.

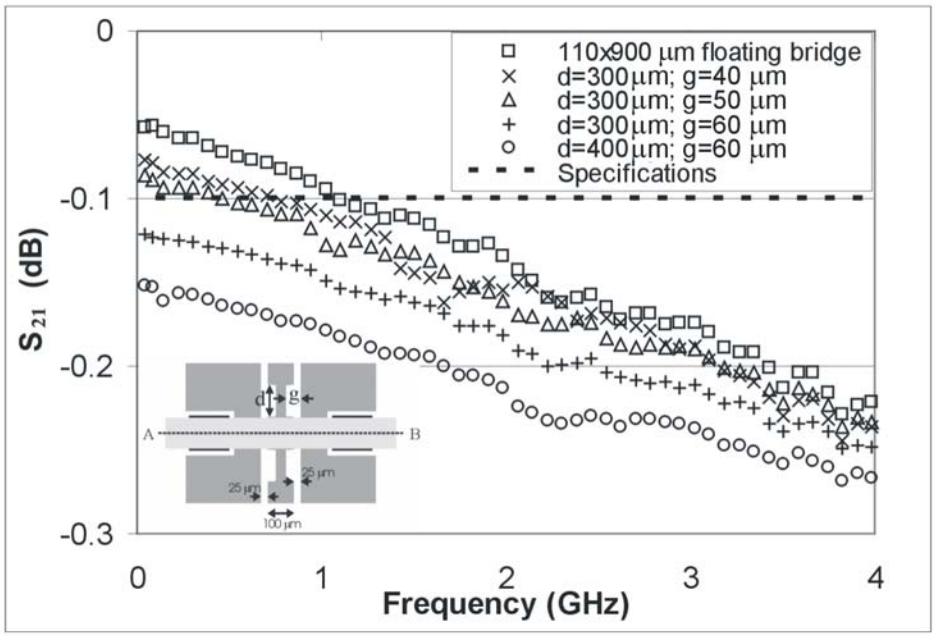

Figure 5.7: Measurements of the S_{21} on the floating bridge sensors with variations in the CPW dimensions for a better impedance match (partly removing of the ground lines).

Compensated circuit by partly removing of the ground lines

This approach consists of the matching of the total circuit by partly removing the grounded lines of the CPW. In this way the gap of the CPW is increased without narrowing the signal line. Thus, a decrease in the reflection losses is expected without the extra resistive losses observed in the previous design.
Figure 5.8 shows the measurement results for the magnitude of the S_{11} parameter up to 4 GHz for different gap dimensions of the CPW. As can be observed, reflections are being reduced as more distance is introduced between the central and the ground lines of the CPW. Furthermore, the matching improves by increasing the length over which the new gap is introduced. From the measurement results we can conclude that the changes in the CPW dimensions work in the desired way, reducing total shunt capacitance and increasing series inductance. The best results are obtained for the largest gap, 175 μm, over the longest distance, 250 μm. In this case, a very good RF behavior is obtained, with even lower reflection losses than required for the target specifications.

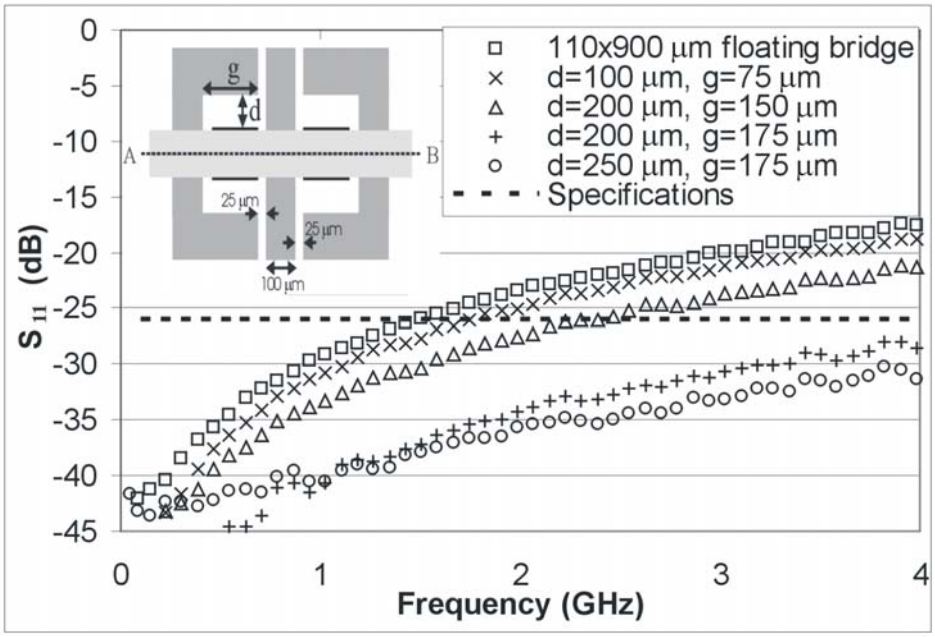

Figure 5.8: Measurements of the S_{11} magnitude on the floating bridge sensors with changing in the CPW dimensions for a better impedance match (partly removing of the ground lines).

In this design, no relevant extra resistive losses are expected to occur since, although the width of the grounded lines is being reduced, we can in most cases neglect the effect on the total conductance of the line. Only for the designs where as a result of the inserted gap the ground lines become extremely narrow, an

increase in the insertion losses could be noticed as observed in the simulation results presented in Chapter 3. Measurements results for the magnitude of the S_{21} parameter are shown in Figure 5.9. As can be observed, a slight decrease of the insertion losses is obtained as the gap area increases. This confirms that the extra resistive losses, which could arise as a consequence of the new design, can be neglected. Nevertheless, we can also see how the insertion losses for the case of the largest gap with the longest distance (g=175 μm and d=250 μm) increase with respect to the sensor with the same gap but with a shorter distance (g=175 μm and d=200 μm). This confirms that we are already at the limit where the resistance losses coming from the ground lines are becoming more relevant than the reduction of the reflection losses.

As expected, using this technique we can optimize the design for both reflection and insertion losses. The best RF characteristics are obtained for the sensor where the gap was changed to 175 μm over a distance of 200 μm. In this case the reflection losses are within the requirements given by the target specifications and the insertion losses are very close to the target specifications (0.04 dB more than required). Increasing the thickness of the aluminum layer used for the CPW lines, or using a better conductor like gold, could improve the design such that also the S_{21} parameter fulfills the target specifications.

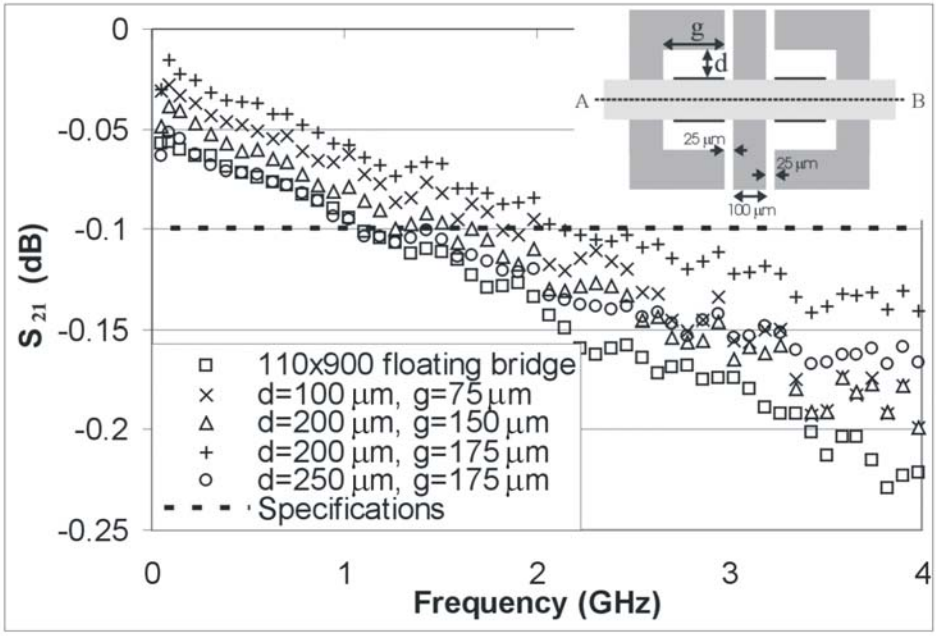

Figure 5.9: Measurements of the S_{21} magnitude on the floating bridge sensors with changing in the CPW dimensions for a better impedance match (partly removing of the ground lines).

5.3 RF power sensitivity and resolution

In order to perform capacitive RF power detection measurements with the bridge sensors, the setup illustrated in Figure 5.10 was used. An RF source supplies the signal that has to be detected. This signal is guided by a 50 cm long cable to an RF probe, which introduces the signal into our bridge sensor. After passing the sensor bridge, the signal travels to a second RF probe, which is again connected to a 50 cm long cable. Finally, the signal arrives at a commercially available RF power meter (HP) to verify the presence of the RF signal at the bridge sensor. At the same time, the capacitance between the sensing electrodes and the bridge is measured by an impedance analyzer (4194A). In this way we can measure the relation between the capacitance change due to movement of the bridge and the power level and frequency of the RF signal traveling through the sensor.

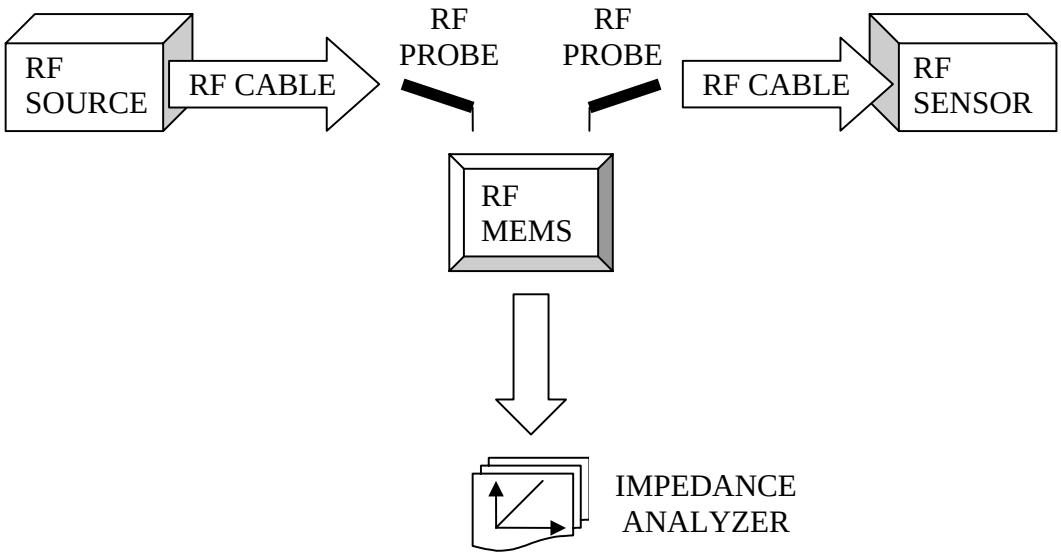

Figure 5.10: Scheme of the set-up used for the characterization of the rf power detection of the different bridge sensor designs.

One of the most difficult aspects of the measurement is to determine the power level of the signal which is present at the position of the bridge sensor. This uncertainty is caused by the reflections and transmission losses which occur not only in the bridge sensor, but also in the probes, cables and the connections with the other systems. As a consequence, the power readout at the end of the circuit differs from the power delivered by the source, and the response is even frequency dependent. As a first approximation, the power level present at the bridge sensor was estimated by taking the average between the readout of the RF source and the

power meter placed at the end of the circuit. Then, the mismatch effect caused by the extra sensor capacitance (Chapter 2, eq. (65)) is used to obtain the final approximation of the signal that is detected by the sensor.

5.3.1 Grounded bridge

Due to the design of the grounded bridge, the sense capacitors are at one side connected to ground. As a consequence, capacitance measurements suffer from parasitic capacitance and noise. As a result, only by using the biggest grounded bridge design (3.2 pF bridge capacitance) the sensitivity was high enough to be detected by the impedance analyzer.
Measurement results of the RF power detection for a 1 GHz signal are shown in Figure 5.11. A linear dependence between the power level of the RF signal and the sensing capacitance can be observed from the measurements.
The measurement results obtained from the DC voltage actuation of the bridge is also included in the graph. In this case, the power level for every point was estimated using the well known equation $P = V^2/Z$, assuming an impedance of 50 Ohm. From the comparison of the measurement results presented in Figure 5.11, we can observe how good DC and RF measurements agree with each other. Therefore, it can be concluded that the RMS voltage squared of the RF signal is detected by the capacitance change in the grounded bridge sensor.

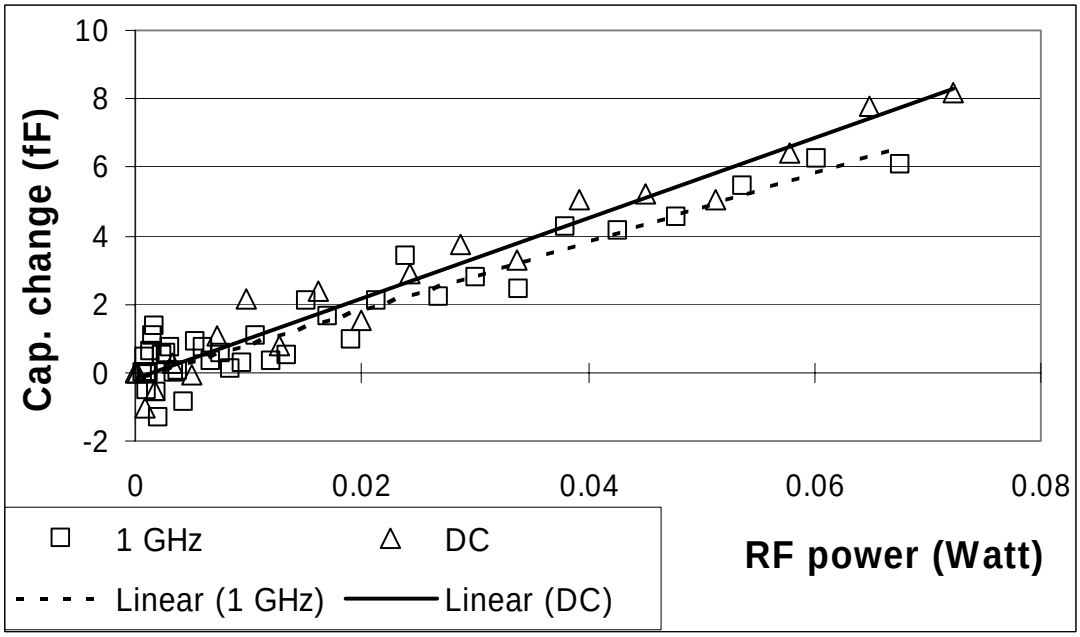

Figure 5.11: Measured capacitance change on the 3600x300 μm grounded bridge as a function of power for 1 GHz rf signal and DC actuation.

From Figure 5.11, a sensitivity of 100 fF/W and a resolution in the order of 10 mWatt can be deduced. Using the mechanical model described in Chapter 3, we can deduce that the measured sensitivity corresponds to a residual stress in the bridge of 20 MPa. This is lower than the stress measured for thin films of aluminum (see Section 4.2.3), which could be expected because part of the stress is relieved by the bending of the bridge and rotation at the suspension points.
Power detection of RF signals with different frequencies was performed in order to characterize the sensor. A constant response versus frequency was expected since the effect of the extra capacitance introduced by the bridge is already taken into account. Figure 5.12 shows the capacitance change measured as a function of frequency for a fixed power level (0.08 W). As can be observed, apart from two frequencies where the detected power is significantly higher (300 and 600 MHz), the difference in the power sensitivity is within the noise level observed in Figure 5.11. The strange behavior measured at the frequencies of 300 and 600 MHz (which correspond to a wavelength of 1 m and 50 cm in vacuum respectively) is most probably caused by standing waves present in the circuit due to impedance mismatch from the different connections between cables, probes and systems.

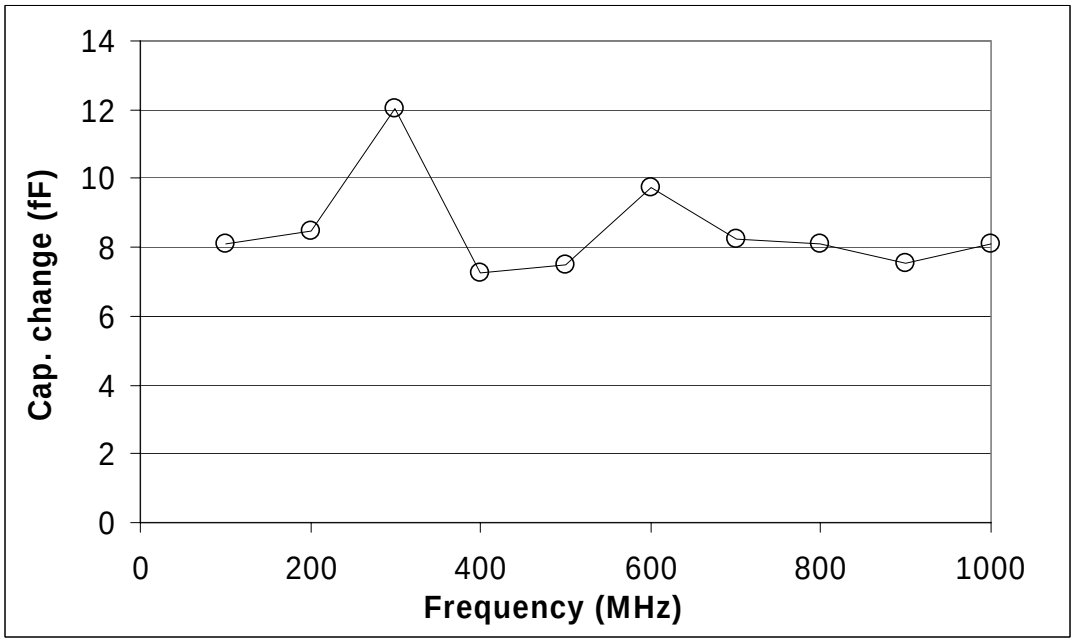

Figure 5.12: Measured capacitance change on the 3600x300 μm grounded bridge as a function of frequency for a fixed power level (0.08 W).

5.3.2 Floating bridge

The movement detection of the floating bridge design was performed by measuring the capacitance change between the floating bridge and the sensing electrodes placed below. Since the capacitance to be measured is not connected to ground, very low parasitic capacitance values and noise level were obtained, increasing the sensitivity and resolution of the measurement with respect to the grounded bridge [5].
Figures 5.13(a) and 5.13(b) show the capacitance change measured for the two different floating bridge sensors when an RF signal of 1 GHz is applied. The measurement results obtained for DC actuation are also included for reference. As expected, a linear relation between the sensing capacitance and the RF signal power was found. Furthermore, the response of the sensor for DC and RF actuation agrees with each other, confirming that the RMS voltage squared of the signal is detected.
As explained in Chapter 3, a factor of two is expected in the sensitivity of the two different floating designs, since one design was twice as big as the other. This is confirmed by the measurements presented in Figure 5.13, where the capacitance change measured by the two designs at a given power of the signal value is related by a factor of two. Comparing Figure 5.13 with Figure 5.11, it can be observed that the capacitance change has the same order of magnitude as in the case of the grounded sensor design. This is in agreement with the model presented in Chapter 3, where the same order of magnitude in the capacitance change was predicted for the floating sensors with respect to the grounded sensors in spite of the different design.

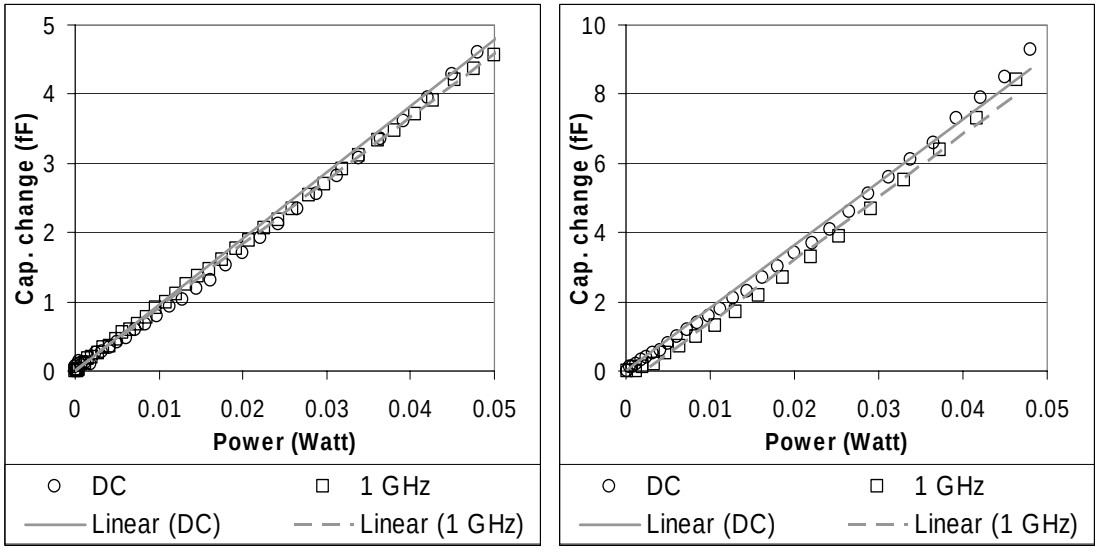

(a) (b)

Figure 5.13: Measured capacitance change on (a) the 120x900 μm and (b) the 210x900 μm floating bridge sensors as a function of power for a 1 GHz signal and DC actuation.

From Figure 5.13, a sensitivity of 91.5 fF/W for the 110x900 μm floating bridge sensor and 180.6 fF/W for the 220x900 μm floating bridge sensor can be deduced. Regarding the resolution of the RF power detection, it can be observed that differences in the order of 500 μW can be distinguished (see figure 5.14).

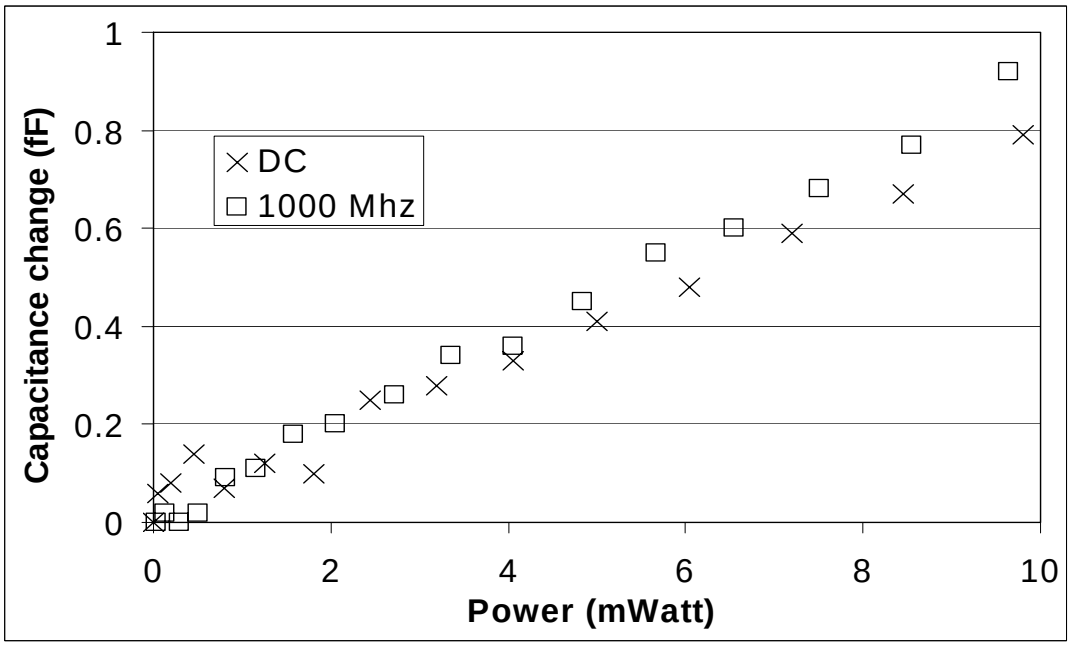

Figure 5.14: Measured response of the 110x900 μm floating bridge at low power levels.

The measured response of the two different floating sensors for different frequencies is shown in Figure 5.15. As can be observed, a flat response as a function of frequency is found apart from two peaks. The first peak is around 300 MHz. The grounded bridge showed the same behavior at this frequency (see Figure 5.12). The second peak appears at 700 MHz in the case of the big floating bridge and at 800 MHz for the small floating bridge, whereas for the grounded bridge this peak appeared at 600 MHz. The exact origin of these peaks is not yet known but it is expected that they are due to the measurement setup and not due to the sensor.

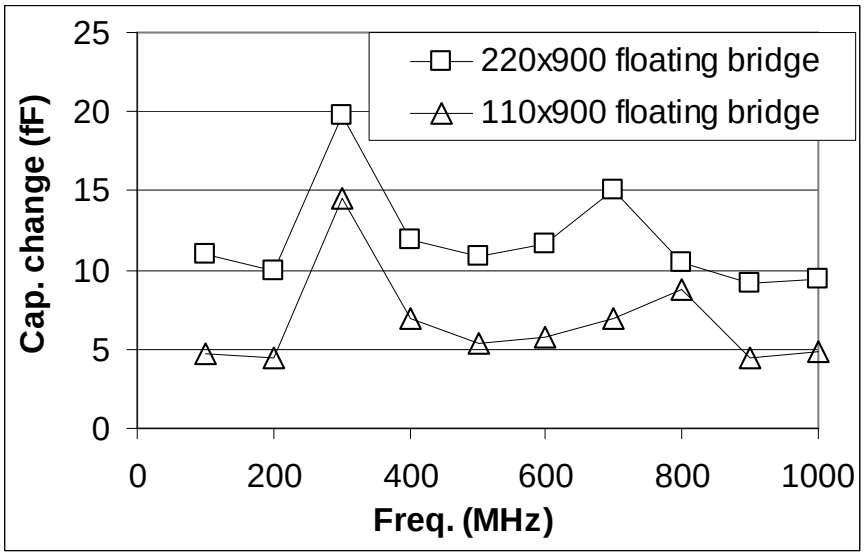

Figure 5.15: Measured capacitance change in the floating bridge designs as a function of frequency for a fixed power level (0.05 Watt).

5.4 Conclusions

Measurement results on the grounded and floating bridge power sensors have been presented. The *S*-parameter results obtained confirmed that the sensor behavior can be modeled by a shunt capacitance, where the capacitance value can be simply calculated from the geometrical dimensions of the bridge. Furthermore, measurements verified the working principle of the matching techniques based on change the CPW dimensions directly before and after the bridge. From the two different approaches, we can conclude that the reflection losses of the sensor can be decreased down to the level required to meet the target specifications presented in apendix A (-26 dB) and even further. The value of -0.1 dB for the S_{21} parameter required by the target specifications is much more difficult to reach. The best results were obtained by the matching technique illustrated by Figure 5.9, where a value of -0.14 dB for the S_{21} parameter is measured for one of the designs. In order to further improve this result, the resistive losses in the CPW lines need to be reduced. Thicker metal lines or the use of better conducting materials like gold are the best option, since the length of the CPW used by the sensor can not be reduced because of the space needed for the matching structure.

The power level of different RF signals was measured capacitively. Linear dependence between RF power and sensing capacitance was found for frequencies up to 1 GHz, and an agreement in the response with respect to DC actuation was observed. Therefore, it can be concluded that the RMS voltage squared of the RF signal is detected, confirming the working principle of the sensor and proving that a ‘through’-type power sensor based on sensing the electric force can be made.

Nevertheless, the resolution of the RF power measurement was worse than required by the target specifications presented in apendix A and further research is needed to improve the resolution and sensitivity.

5.5 References

[1] "On-wafer Vector Network Analyzer calibration and measurements", Cascade microtech.

[2] J.B. Muldavin and G. M. Rebeiz, "High isolations MEMS shunt switches; Part 1: Modeling", *IEEE Trans. Microwave Theory Tech.*, Vol. 48, No. 6, pp. 1045-1052, June 2000.

[3] Muldavin J.B., Rebeiz G.M.: "High-isolation CPW MEMS shunt switches. 1. Modeling", *IEEE Transactions on Microwave Theory and Techniques*, Volume: 48 Issue: 6 , June 2000, pp. 1045 –1052.

[4] L.J. Fernandez, J. Sesé, R.J. Wiegerink, J. Flokstra, H.V. Jansen, and M. Elwenspoek, "Radio frequency power sensor based on MEMS technology with ultra low losses," *MEMS-05*, Miami, Florida, Jan. 30 - Feb. 3, 2005.

[5] "Agilent technologies impedance measurements handbook", 2nd edition, Agilent technologies.

Chapter 6

SiRN trench refilling on Si substrates for RF applications

6.1 Introduction

As discussed in Chapter 4, the need for a low-loss substrate forced us to use AF45 glass. Still, using a silicon substrate could have some important advantages. Using an AF45 substrate implies the use of a low-temperature surface micromachining process since bulk micromachining in glass is complicated and high-temperature processing steps are not possible. A silicon substrate on the other hand allows bulk micromachining by well-developed techniques like deep reactive ion etching (DRIE) or anisotropic wet etching [1]. Furthermore, high-temperature processing is no problem, allowing low-pressure chemical vapor deposition (LPCVD) of low-stress poly-Si and silicon-nitride layers. When used as structural material in an RF power sensor these materials would result in much better mechanical properties than obtained with aluminum. Finally, a silicon substrate would allow monolithic integration of the power sensor with readout electronics. This could significantly improve the measurement resolution due to the absence of the parasitic capacitance associated with interconnecting (bond) wires.

In this chapter, different versions of the so called SiRN blocks are proposed in order to improve locally the RF performance of low-resistivity silicon. Measurements performed on coplanar waveguides fabricated on top of the SiRN blocks show considerably lower losses than on an untreated low resistivity silicon wafer. Furthermore, the best designs show a performance that is very close to that obtained with AF45 glass substrates.

6.2 Motivation

The enormous growth of wireless and portable applications has led to a strong demand for high-performance monolithic low-cost passive components in RF and microwave integrated circuits (ICs). However, some traditional microwave passive components like transmission lines and filters are difficult to integrate on the same chip with the RF and microwave circuits due to the high substrate losses associated with standard low-resistivity CMOS-grade silicon substrates. As a result, most RF and microwave components are realized on special substrates like AF45 glass [2, 3] or quartz [4]. Several techniques have been developed to allow the realization of low loss RF devices on standard silicon. These techniques include the use of dielectric layers like polyimide [5] and benzocyclobutene [6], the use of polysilicon patterned ground shields [7], the use of silicon bulk-micromachining to remove the substrate locally under the RF components [8–10] , and the use of surface-micromachined suspended metal structures at a distance of several tens of micrometers above the silicon surface [11, 12]. However, all these techniques impose restrictions on the device structures that can be realized. The best results are obtained with the freely suspended structures [8–12], but such free hanging structures are rather delicate, vulnerable to shocks and vibration and difficult to package. In this chapter we describe a new technique in which the silicon substrate is locally replaced by silicon-rich silicon nitride (SiRN) [13], which has very good RF properties ($\tan \delta = 5 \ldots 9 \cdot 10^{-4}$). The technique basically consists of etching deep trenches and refilling these trenches by LPCVD SiRN. This process could even be performed in a pre-CMOS process, i.e. before performing the regular CMOS process in order to obtain monolithic integration of RF devices with CMOS circuits.
Several test wafers have been processed with various depths of the trenches refilled by silicon nitride. Low-stress, silicon-rich silicon nitride [14, 15] (SiRN) is used in order to minimize curvature of the silicon wafer due to residual tensile stress. The effectiveness of the technique was evaluated by measuring the RF losses of 1 mm long coplanar waveguides (CPW), which were realized on top of the SiRN blocks. Two types of SiRN blocks can be distinguished as indicated in Figure 6.1: blocks consisting completely of SiRN and blocks consisting of alternating plates of SiRN and monocrystalline Si. As will be shown in this chapter, the latter already gives a significant improvement of the RF performance.

Blocks consisting entirely of SiRN are somewhat more difficult to fabricate but performance levels very close to dedicated RF substrates like AF45 are obtained.

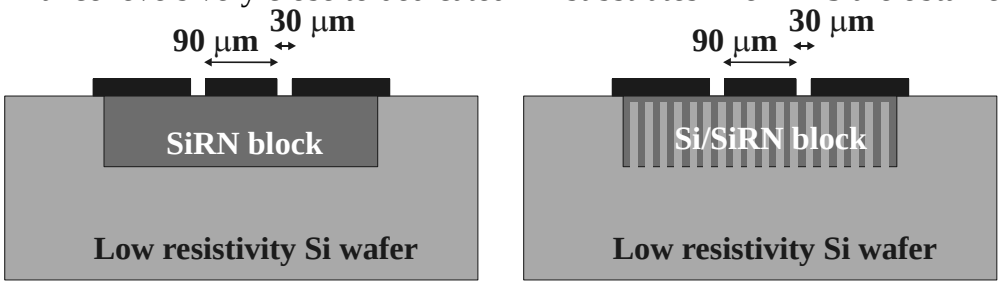

Figure 6.1: (a) Coplanar waveguide (CPW) on a solid SiRN block, and (b) CPW on a block consisting of alternating plates of SiRN and Si.

6.3 Fabrication

The deposition of dielectric materials like silicon nitride is limited to a few micrometers due to the insertion of stress on the substrate, being too thin for use as intermediate layer between RF components and the silicon substrate. As an alternative, a thick dielectric layer created by the refilling of deep trenches by silicon-rich nitride is proposed, exploiting the perfect conformal step coverage of low pressure chemical vapor deposition (LPCVD). By using this technique, a layer of dielectric material, with a thickness determined by the depth of the trenches (tens of micrometers), can be created. The process was successfully tested on two types of wafers: with <100> and <110> crystal orientation. The only difference is in the etching of silicon: in <110> wafers the silicon crystal orientation can be exploited to etch deep trenches by anisotropic wet chemical etching, e.g. by TMAH or KOH; in standard <100> wafers this is not possible and deep reactive ion etching (DRIE) was used.

6.3.1 Si/SiRN block

The Si/SiRN block can be considered as the first step for the substrate replacement. Nevertheless, it will be shown that optimization in the designs regarding the orientation with respect to the CPW and minimizing the thickness of the silicon between the SiRN plates already results in acceptable losses for many RF applications.
Figure 6.2 shows a summary of the fabrication process. The process starts with the deposition of a thin layer of silicon nitride (100 nm). This layer is patterned by DRIE using photoresist as a mask, creating a large number of parallel rectangles. The width and spacing between the rectangles are in the order of 2 μm. Next, deep trenches are created by anisotropic etching of the silicon substrate. Then, the

silicon nitride layer, which acted as a mask is removed using DRIE and a new silicon nitride layer is deposited by LPCVD.

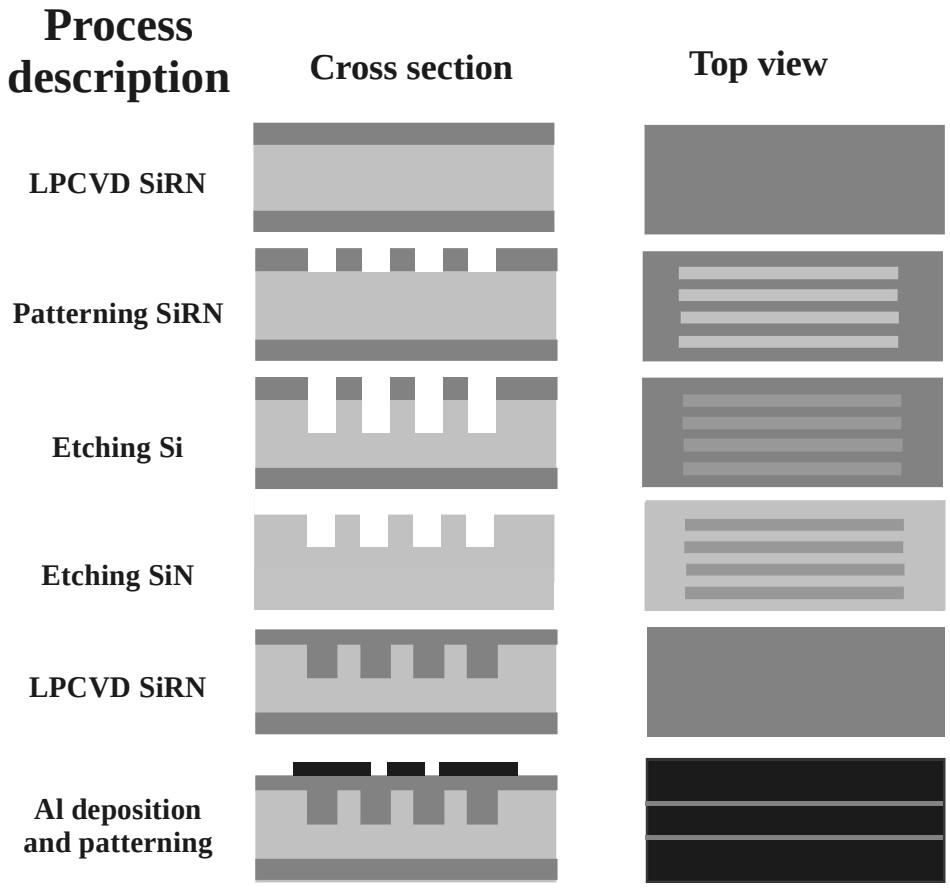

Figure 6.2: Fabrication process scheme for Si/SiRN blocks embedded in silicon substrates.

Due to the excellent conformal step coverage during LPCVD deposition, the trenches are completely filled by a deposition of 1 μm of silicon nitride. Then, a 1 μm thick aluminum layer was deposited by sputtering and patterned in order to build a 1 mm long CPW which will be used for characterizing the RF properties of the treated substrate. The dimensions of the CPW are shown in Figure 6.1.
Three different parameters of the fabrication process were tuned in order to study their influence on the RF characteristics on the treated substrate area and be able to optimize it. First of all, two different relative orientations of the plates with respect to the CPW lines were fabricated: parallel and perpendicular. SEM pictures showing the fabrication results for both designs are presented in Figure 6.3. A better understanding of the loss mechanisms is expected from analyzing the measurement results obtained from these designs.

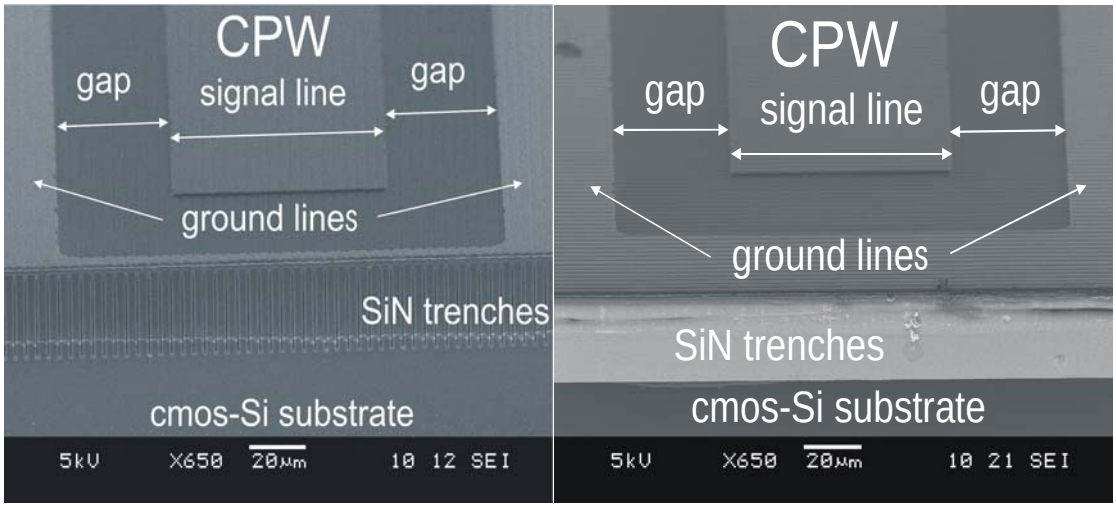

(a) (b)

Figure 6.3: SEM pictures showing the cross section and surface of two different plates orientations with respect to the CPW lines : a) parallel, b) perpendicular.

The second fabrication parameter studied was the ratio in the width dimension between SiRN and Si plates for a certain block thickness. Figure 6.4(a) shows a Si/SiN block with 2.2 µm wide Si and 1.8 µm wide SiRN plates. Figure 6.4(b) shows a block with 1.5 µm wide Si and 2.5 µm wide SiRN plates.

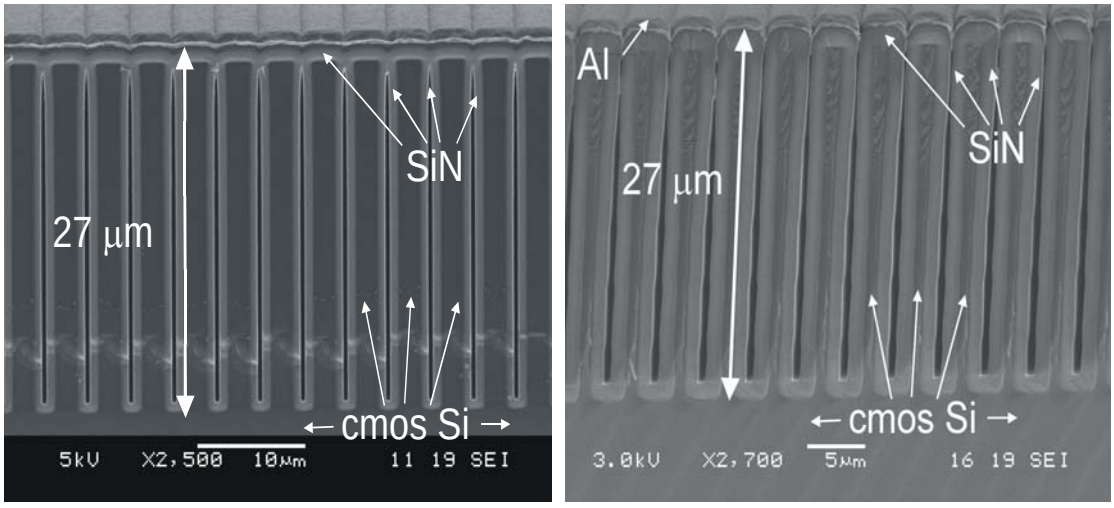

(a) (b)

Figure 6.4: Cross section SEM pictures of two different plate widths: a) 1.8/2.2 µm-Si/SiRN, b) 1.5/2.5 µm-Si/SiRN.

In both cases the total thickness of the block is constant (27 μm). In this way, the relation between the amount of substrate material replaced by SiRN and the transmission losses can be studied.
It can be observed from the pictures shown in Figure 6.4 that, due to a slightly negative profile on the anisotropic etching of the silicon, the trenches are wider at the bottom than at the top. This resulted in vacuum cavities at the bottom of the trenches (see figure 6.5(b)), since the top level was closed by silicon nitride first (see Figure 6.5(a)), blocking the deposition for the rest of the trench. Nevertheless, no negative effects are expected from this on the mechanical or RF performances, since the final result is completely stable and vacuum has perfect RF properties.

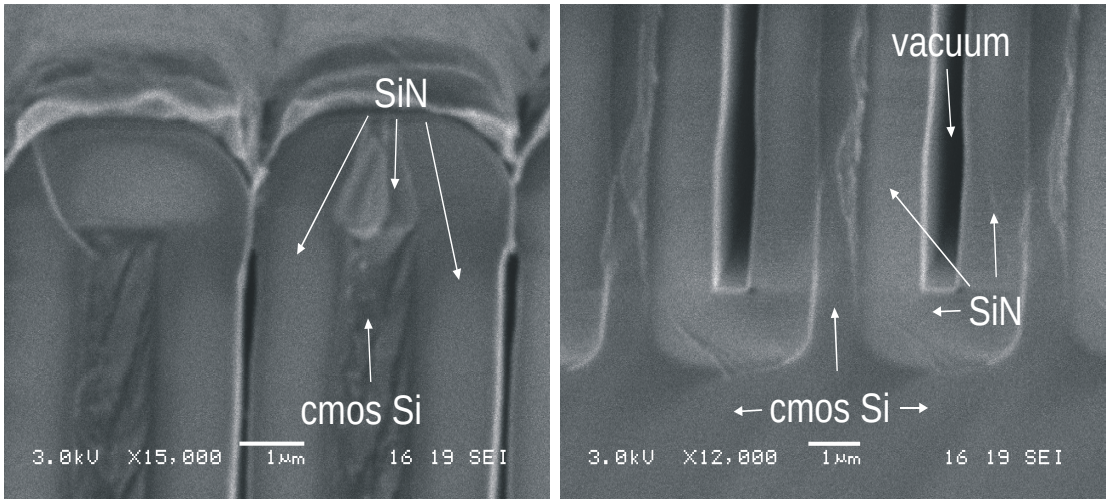

(a) (b)

Figure 6.5: SEM pictures showing the zoom in on the cross section of a 1.8/2.2 μm-Si/SiRN block: a) surface, b) bottom of the block.

Finally, 37 μm thick blocks for the case of 2.5 μm wide SiRN and 1.5 μm wide Si plates were fabricated. The fabrication result is shown in Figure 6.6. The comparison of measurement results of this block with respect to the one shown in Figure 6.4(b), where the thickness was 27 μm, will allow us to study the relation between losses and block thickness.

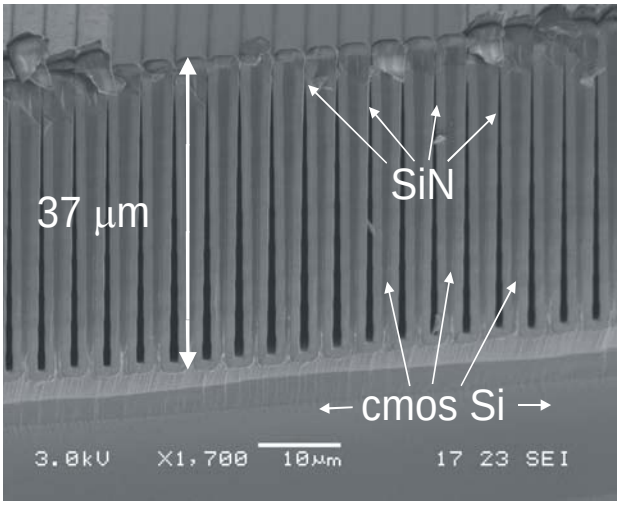

Figure 6.6: SEM picture of a cross section of a 1.5/2.5 μm-Si/SiRN block 37 μm thick.

6.3.2 Complete SiRN block

A further improvement in the RF performance of the substrate could be obtained by a complete replacement of the substrate material. As a result, a complete SiRN block is created. The fabrication process starts from a Si/SiRN block as shown in Figure 6.7.
First, patterning of the top silicon nitride layer by DRIE is performed in order to gain access to the silicon that is still located between the refilled trenches. This silicon is then removed, creating trenches separated by SiRN walls. In the case of <110> wafers, silicon etching is done by wet chemical etching, although DRIE would also be possible. For <100> wafers two options are possible, namely DRIE of silicon, and wet chemical etching, provided that the trenches have the correct alignment to the crystal orientation, i.e. at an angle of 45 degrees with respect to the wafer-flat. In this case, due to the silicon crystal orientation, deep trenches are possible thanks to the silicon nitride walls in between the silicon. We used this option for our <100> test samples because of its simplicity and its very high selectivity with respect to silicon nitride. Figure 6.8 shows SEM pictures of the result obtained at this point, where silicon nitride columns 2 μm wide stand freely with a space in between of 2 μm. As can be observed in the pictures, the silicon nitride columns are not attacked thanks to the excellent selectivity during the wet etching step.

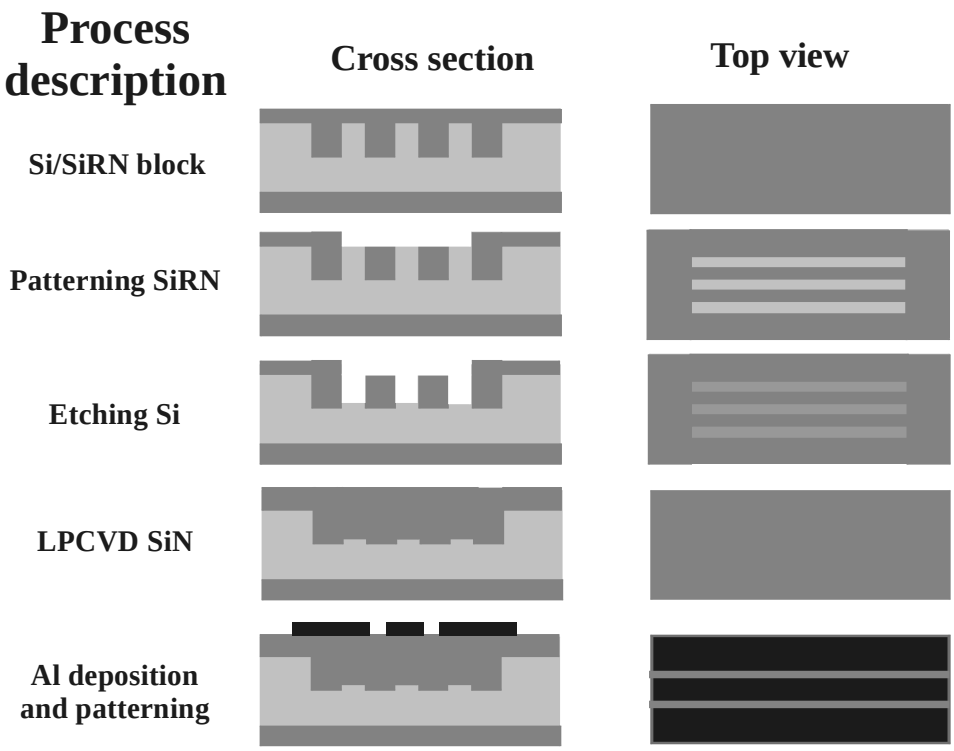

Figure 6.7: Fabrication process scheme for complete SiRN blocks embedded in silicon substrates from a Si/SiRN block.

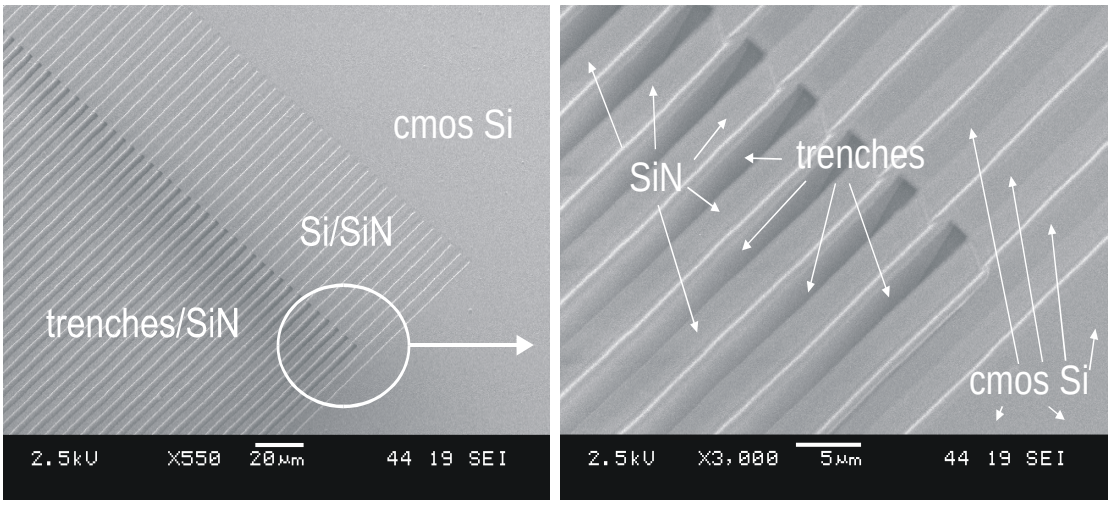

a) b)

Figure 6.8: SEM pictures showing the top view of 2 µm wide free standing SiRN plates.

Trenches are then refilled again by silicon-rich nitride using LPCVD, resulting in a so-called "complete silicon nitride block". Different widths of the treated area ('b' in Figure 6.1) were performed. Once the silicon nitride block is finished, a CPW was fabricated on top with the dimensions shown in Figure 6.1. A SEM picture showing the cross section of a 15 μm thick complete SiRN block is presented in Figure 6.9. As can be observed, no silicon remains inside of the treated area, resulting on a region where a silicon nitride layer is embedded in the wafer with a thickness determined by the depth of the trenches created in the substrate. We can also see how the vacuum cavities inside the refilled trenches are smaller thanks to the second refilling step, since when the silicon nitride is etched before performing the second silicon etching, the vacuum cavities are also reached. Therefore, an extra layer of silicon nitride fills the cavities making them slightly narrower.

A 45 μm thick complete SiRN block was fabricated in order to study the effect of total thickness on the RF performance of the substrate. The pictures shown in Figure 6.10 show the fabrication results. As can be observed from Figure 6.10(a), a few trenches could only be refilled for a very short time, most probably due to sticktion problems between the free standing SiRN free plates. The close-up in Figure 6.10(b) shows that a tiny Si column still remains in between the refilled trenches. This could be caused by too short etching during the patterning of the SiRN at the beginning of the process, leaving small amount of SiRN at the corners of the Si plates which would act as a mask during the anisotropic etching. Nevertheless, due to the very small amount of Si left in the block, no significant effects are expected and it is considered still as a complete SiRN block.

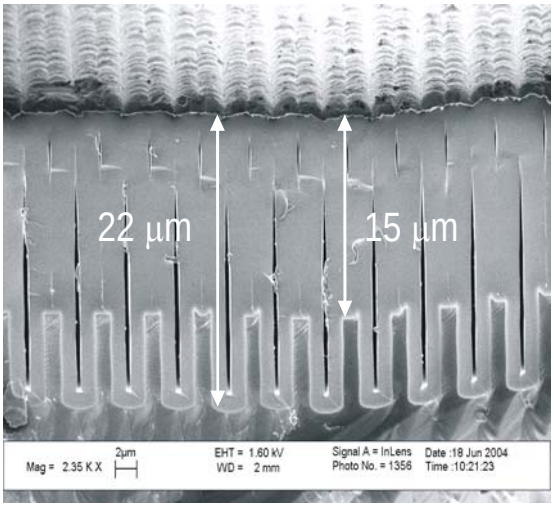

Figure 6.9: SEM picture showing the cross section of a complete SiRN block 15 μm thick.

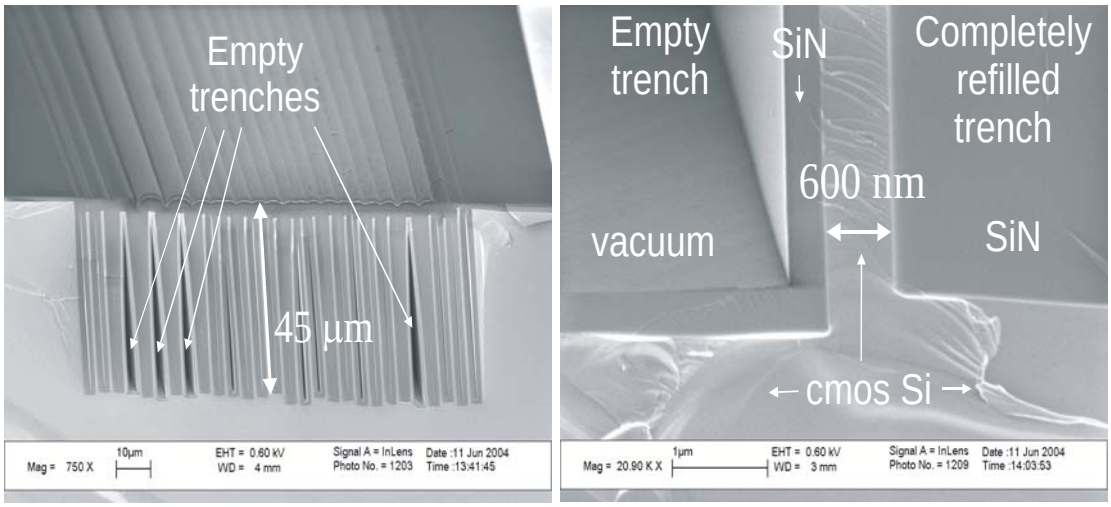

a) b)

Figure 6.10: SEM pictures showing the cross section of a 45 µm thick complete SiRN block: a) overview of the SiRN block, b) close-up at the bottom of the SiRN block.

6.4 RF characterization

In order to characterize the RF behavior of the SiRN blocks, *S*-parameter measurements up to 4 GHz were performed using a vector network analyzer (RF source: HP83651B, test-set: HP8517B, controller: HP8510C). Since aluminum was used for the realization of the CPW, measurements were realized using RF probes with a sharp needle profile (see Chapter 5). Due to the good matching obtained on the aluminum CPW, the transmission losses of the SiRN blocks can be studied by the measurement results obtained on the S_{21} parameter.

6.4.1 Si/SiRN block

Three different parameters of the Si/SiRN block design were varied as explained in Section 6.3. The dependence observed in the RF performance of the block as a function of every design parameter will be presented and interpreted separately.

Relative orientation of the plates with respect to the CPW lines

Figure 6.11 show the insertion loss measured on 1.8/2.2 µm-Si/SiRN for two different plate orientations with respect to the CPW lines, parallel and perpendicular (see SEM pictures in Figure 6.3). The block thickness for both configurations was 27 µm. Measurement results on silicon wafers without any treatment and AF45 wafer (dedicated glass for RF applications) are added in the graph for reference.

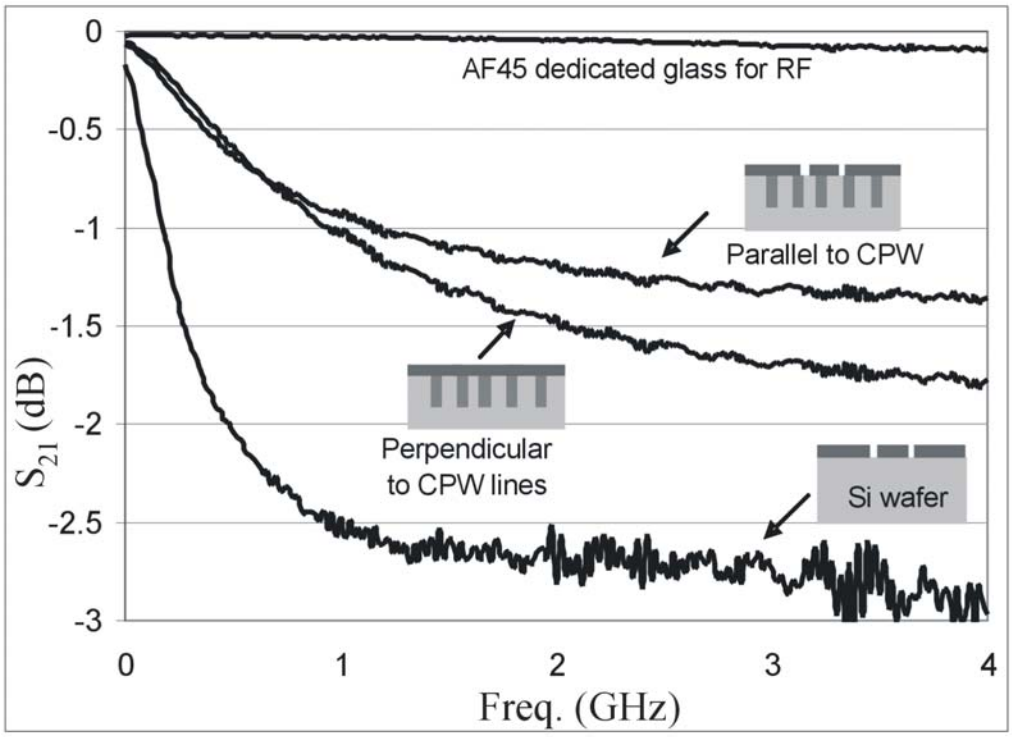

Figure 6.11: S_{21} magnitude measurement results on 1.8/2.2 μm-Si/SiRN block with two different relative orientations with respect to the CPW lines (parallel and perpendicular) low resistivity silicon wafer and dedicated glass for RF (AF45).

As can be seen from Figure 6.11, for the case of Si/SiRN blocks plates perpendicular to the CPW lines, transmission losses are reduced approximately 1 dB at 4 GHz with respect to the low resistivity silicon. Furthermore, when the orientation of the plates formed by the Si/SiRN blocks is rotated 90 degrees with respect to the transmission line (parallel to the CPW lines), a further reduction by 0.5 dB is obtained, resulting in total transmission losses of -1.3 dB at 4 GHz. The reducing of the losses is obtained although the amount of silicon removed under the transmission is the same in both cases. Therefore, a strong relation between the relative orientation of the trenches and the transmission line is found.
The difference in the transmission losses due to the orientation can be explained by looking at the direction of the electric field created by the RF signal on the CPW lines, see Figure 6.12. When plates are perpendicular to the CPW lines, there are paths where electric field is allowed to travel from the signal to the ground line of the CPW through the conducting silicon, ending with high transmission losses. But when trenches are parallel to the transmission line, the electric field needs to cross alternatively silicon and silicon nitride, which is an isolating material, or travel all the way down from the central line to the untreated part of the silicon wafer and up again at the ground lines. Therefore, the conductivity of the substrate

below the transmission line is reduced significantly reducing the electrically-induced current losses.

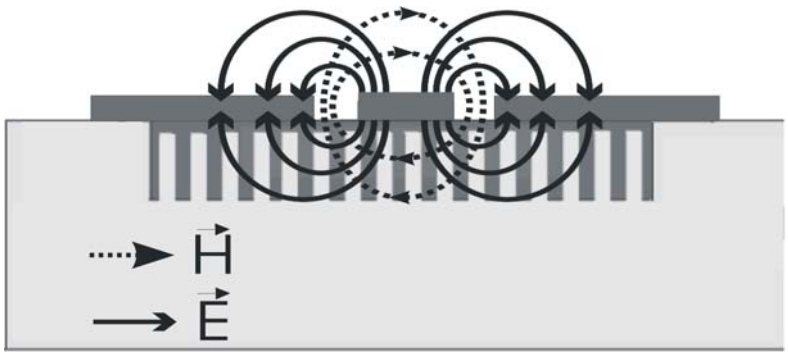

Figure 6.12: Illustration of electrical and magnetic fields created on a Si/SiRN block due to the presence of a CPW on top carrying a RF signal.

As a consequence of the measurement results, it was concluded that the parallel orientation of the plates on a Si/SiRN block was the optimum situation regarding substrate losses. Therefore, the parallel orientation used for all subsequent Si/SiRN blocks presented in this chapter.

Width ratio between Si and SiRN plates

The ratio between the width of the SiRN and silicon plates represents the percentage of silicon material replaced. Therefore, a strong relation between this parameter and the substrate losses measured on the CPW is expected. Figure 6.13 shows the measurement results on Si/SiRN blocks with two different relative widths, but the same thickness (27 μm) and orientation with respect to the CPW lines (parallel). The measurement results obtained on untreated low resistivity silicon and AF45 dedicated glass substrate are again included for reference.

As can be observed from Figure 6.13, lower losses are obtained for the case where higher amount of silicon is replaced by SiRN. While -1.3 dB/mm losses are obtained at 4 GHz for a 2.2/1.8 μm Si/SiRN block, a further improvement by 0.5 dB/mm was measured on 1.5/2.5 μm Si/SiRN, reaching a value of -0.8 dB/mm. Although the losses are still considerably higher than on dedicated glass substrates, a very large improvement with respect to the untreated low resistivity silicon is already achieved.

Further increasing of the SiRN width was not possible, since the silicon plates left would become too weak and would collapse to each other, making the deposition of the SiRN impossible.

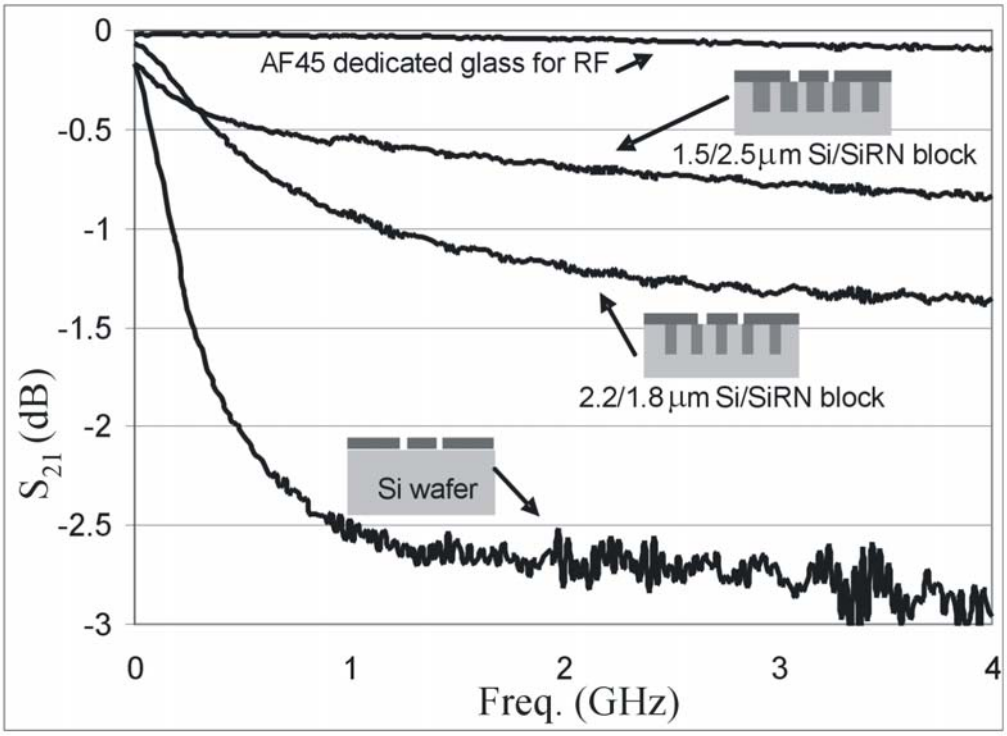

Figure 6.13: S_{21} magnitude measurement results on 2.2/1.8 μm and 1.5/2.5 Si/SiRN block, low resistivity silicon wafer and dedicated glass for RF (AF45).

Thickness of the Si/SiRN blocks

Since the total thickness of the Si/SiRN block is similar to the gap of the CPW, still considerably high amount of the electric field from the RF signal is expected to cross the untreated silicon below the Si/SiRN block. Therefore, Si/SiRN blocks with larger thickness were fabricated and measured.

Figure 6.14 show the measurement results of two Si/SiRN blocks with different thicknesses, 27 and 37 μm. As can be observed, only a slightly better result is obtained for the thicker Si/SiRN block, reducing the transmission losses at 4 GHz from the -0.8 dB/mm obtained on the 27 μm thick block, to -0.7 dB/mm measured for the case of 37 μm. It can be then concluded that the thickness does not have the expected influence on the total transmission losses for a Si/SiRN block. Most probably the dominant loss mechanism is not due to the untreated silicon below the Si/SiRN block, but due to the remaining silicon in between the SiRN plates. Nevertheless, reasonably good RF properties are reported at this point, which may already be acceptable for many applications.

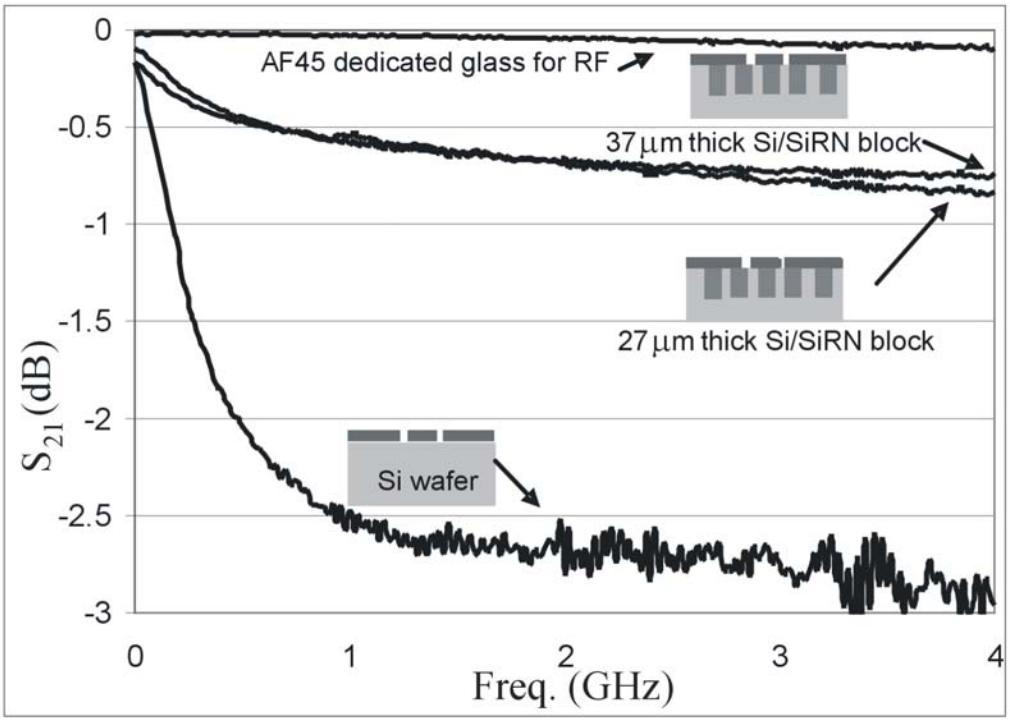

Figure 6.14: S_{21} magnitude measurement results on 27 and 37 μm thick Si/SiRN blocks, a low resistivity silicon wafer and a dedicated AF45 glass wafer.

6.4.2 Complete SiRN block

Figure 6.15 shows the measurement results for the two different thicknesses of complete SiRN blocks which were fabricated, 15 and 45 μm. Measurement results show transmission losses at 4 GHz of -0.45 dB/mm for the case of a 15 μm thick SiRN block and only -0.2 dB/mm when the thickness is increased to 45 μm. Therefore, it can be concluded that, contrary to what we observed for the Si/SiRN blocks, a very strong relation between thickness of complete SiRN blocks and losses is found. This confirms the assumption in the previous section that in the case of the Si/SiRN blocks of Figure 6.14 the dominant loss is caused by the silicon plates inside the blocks and not by the silicon substrate underneath the blocks. For solid SiRN blocks the losses must come from the substrate under the block. Therefore, better performance is expected for thicker SiRN blocks, especially since the thickness of the blocks is still in the order of the gap distance between signal and ground lines of the CPW. Although further improvement of the RF properties of the substrate could be expected for even thicker SiRN blocks, the problems already encountered in the fabrication of the 45 μm thick blocks require a further development of the etching process first. Nevertheless, the losses reported in Figure 6.15 are already very close to the dedicated glass substrate. The

RF properties are good enough for most of RF applications, with the advantage of using a much cheaper substrate that allows much more freedom in processing, easier packaging, and even monolithic integration with CMOS electronics.

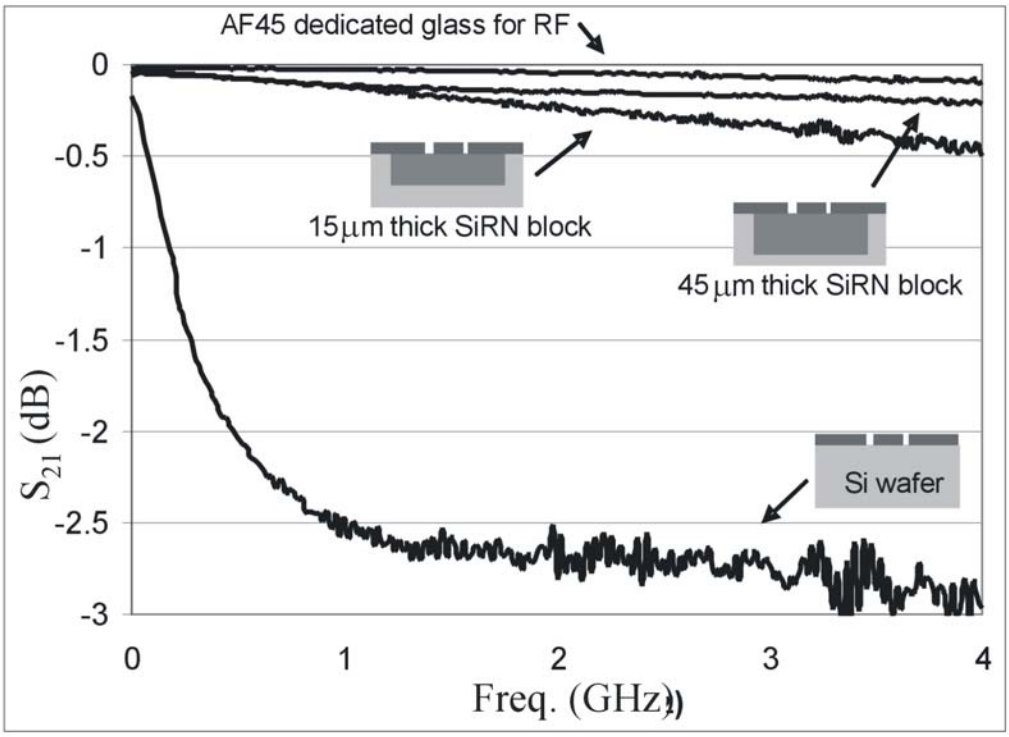

Figure 6.15: S_{21} magnitude measurement results on 15 and 45 μm thick complete SiRN blocks, a low resistivity silicon wafer and a dedicated AF45 glass wafer.

To study the improvement of the RF properties of a CPW in relation to the area where the silicon is replaced by SiRN, blocks 15 μm thick with different total widths were fabricated and measured (see Figure 6.16). Measurement results obtained for three different total widths of the blocks, 50, 100 and 900 μm, are shown in Figure 6.17. As could be expected, losses decrease with the increasing width of the silicon nitride block. However, the large improvement obtained by increasing the width from 50 to 100 μm, which is still only slightly larger than the width of the signal line, is remarkable. Compared to this, the further increase to 900 μm only gives a marginal improvement. Apparently, having a good dielectric at the edge of the signal line, where the electric field is the strongest, has the most influence.

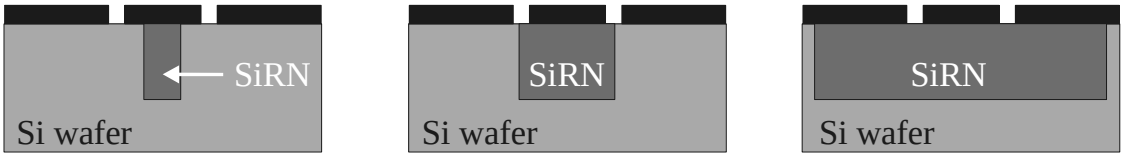

(a) (b) (c)

Figure 6.16: Illustration of three different total widths of complete SiRN block designs: a) 50 μm, b) 100 μm, c) 900 μm.

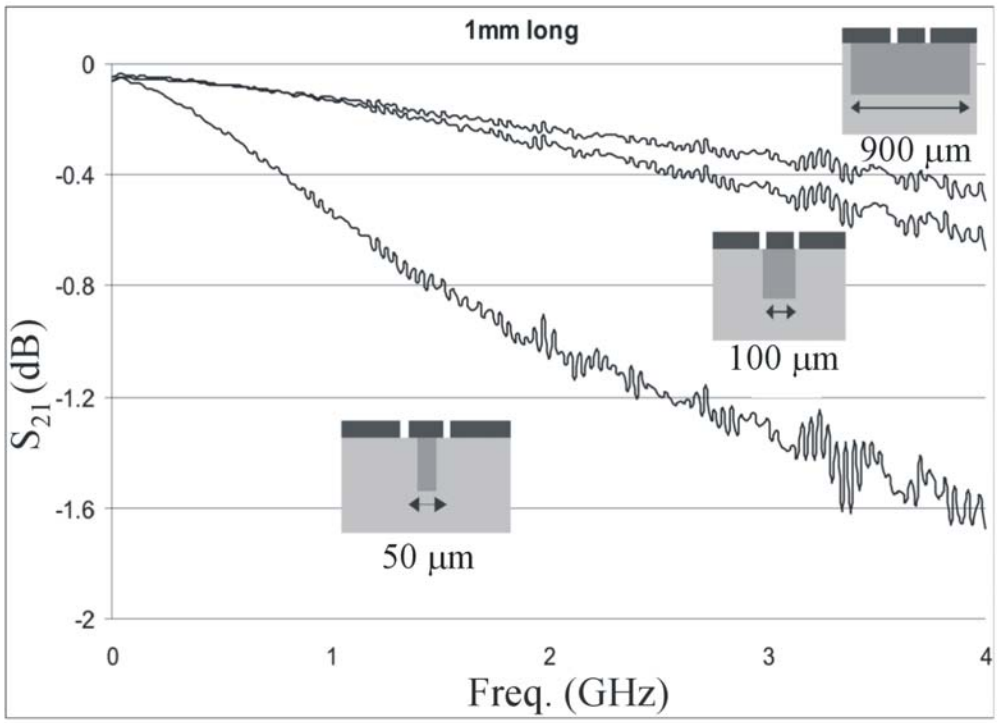

Figure 6.17: S_{21} magnitude measurement results on 50, 100 and 900 μm wide complete SiRN block.

6.4.3 Summary

Figure 6.18 shows an overview of the measurement results obtained for the different designs analyzed in this chapter. All of them are based on the use of low resistivity silicon wafers with the exception of the AF45 dedicated glass used as a reference.

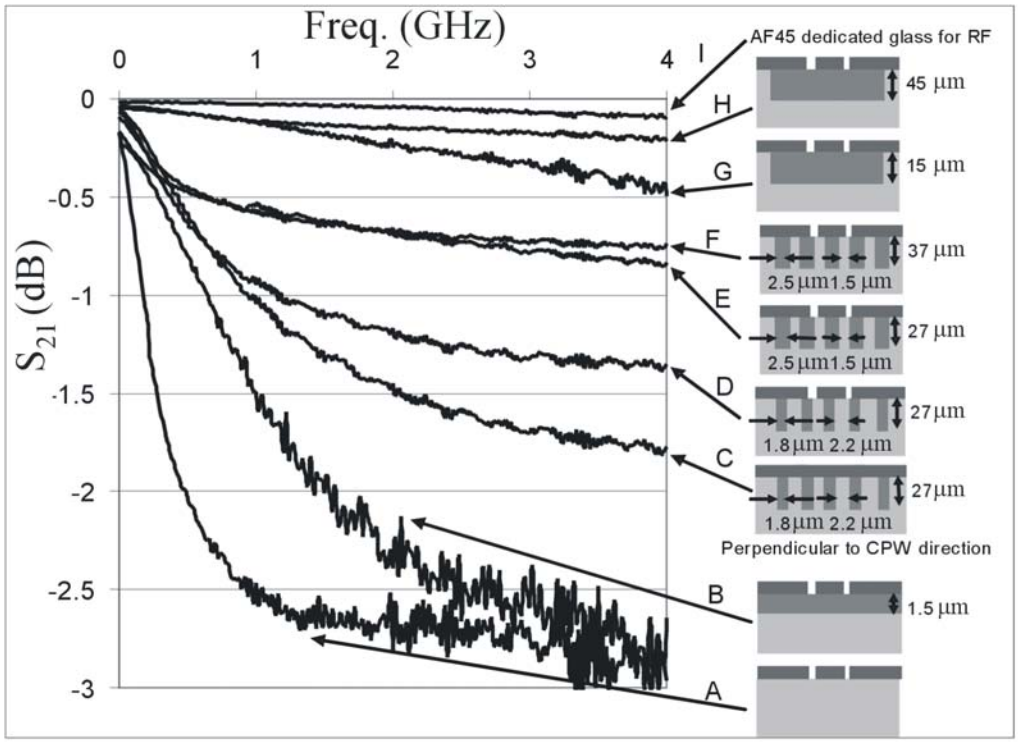

Figure 6.18: S_{21} magnitude measurement results overview on AF45 glass (I), low resistivity silicon wafer (A) and all different SiRN blocks presented in this chapter: 1.5 thick SiRN layer (B), perpendicular 2.2/1.8-Si/SiRN block 27 µm thick (C), parallel 2.2/1.8-Si/SiRN block 27 µm thick (D), parallel 1.5/2.5-Si/SiRN block 27 µm thick (E), parallel 1.5/2.5-Si/SiRN block 37 µm thick (F), complete SiRN block 15 mm thick (G) and complete SiRN block 45 mm thick (H).

From Figure 6.18, it can be observed that compared to a standard low resistivity silicon wafer a relevant improvement of the RF properties is already obtained with the Si/SiRN blocks. Remarkable is the wide scope of results that can be achieved by optimization of two design parameters: the orientation of the plates with respect to the CPW and the width ratio between the Si and SiRN plates. The best result obtained for Si/SiRN blocks was a S_{21} of -0.7 dB/mm at 4 GHz. Even better results are obtained with complete SiRN blocks. For complete blocks, the main design parameter in order to optimize the RF properties is the thickness of the block. The -0.2 dB/mm value obtained for the magnitude of the S_{21} parameter represents a remarkable achievement, proving that transmission losses can be obtained that are very close to those obtained on dedicated glass substrates. It must be noted that this 'best' SiRN block still contained some narrow plates of silicon as discussed in Section 6.3.2. Therefore, a slightly better result may be possible by further optimization of the fabrication process.

6.5 Conclusions

A technique to improve the RF properties of low-resistivity silicon wafers based on the refilling of deep trenches with SiRN has been presented. Using this technique, areas can be created in the silicon wafer where the RF signals do not suffer from the high losses normally associated with standard low-resistivity silicon substrates.
Two different approaches have been proposed, Si/SiRN blocks and complete SiRN blocks. In the case of Si/SiRN blocks, the bulk silicon of the wafer is replaced only partially, creating alternating plates of Si and SiRN. Nevertheless, by optimization of design parameters such as the orientation of the block with respect to the CPW and the width ratio between the Si and SiRN plates, CPW transmission losses S_{21} were measured of only of -0.7 dB/mm at 4 GHz. The best results were obtained for complete SiRN blocks, where the silicon material is completely replaced by SiRN. In this case, the magnitude of the S_{21} was reduced to -0.2 dB/mm at 4 GHz, which is very similar to the -0.1 dB/mm measured on a dedicated AF45 glass.
It can be concluded that with the proposed Si/SiRN and complete SiRN blocks it is possible to realize low-loss RF devices on standard silicon substrates. This means that a wide variety of fabrication processes (e.g. bulk micromachining by DRIE and anisotropic wet etching, surface micromachining using poly-Si or SiRN structural layers) is now available for RF MEMS devices, whereas for example on AF45 substrates only low-temperature surface micromachining is possible. Furthermore, it must be noted that the realization of the nitride blocks could be done as a pre-CMOS process, i.e. before performing the regular CMOS process. This would allow monolithic integration of low-loss RF components with CMOS electronics. For the RF power sensor discussed in this thesis this could significantly improve the resolution due to the absence of parasitic capacitance related to interconnecting (bond) wires.

6.6 References

[1] M.C. Elwenspoek, H.V. Jansen, *Silicon micromachining*, United Kingdom: Cambridge University Press, ISBN: 0-521-59054-X.

[2] H.A.C. Tilmans, W. De Raedt and E. Beyne, "MEMS for wireless communications: 'from RF-MEMS components to RF-MEMS-SiP'," *J. Micromech. Microeng.*, 13, 2003, S139–S163.

[3] L.J. Fernandez, E. Visser, J. Sese, R.J. Wiegerink, J. Flokstra, H.V. Jansen, M. Elwenspoek, "Radio frequency power sensor based on MEMS technology", *IEEE sensors conference*, Toronto, Canada, October 22-24, 2003.

[4] J.B. Rizk, G.M. Rebeiz, "W-band CPW RF MEMS circuits on quartz substrates," *IEEE Trans. on Microwave Theory and Techniques*, 51 (7), 2003, 1857-1862.

[5] G.E. Ponchak and A.N. Downey, "Characterization of thin film microstrip lines on polyimide," *IEEE Trans. Component Packaging Manufac. Technologies B*, 12, 1998, 171-176.

[6] L.L.W. Leung, K.J. Chen, X. Huo, P.C.H. Chan, "Low-loss microwave filters on CMOS-grade standard silicon substrate with low-k BCB dielectric," *Microwave and Optical Techn. Letters*, 40 (1), 2004, 9-11.

[7] C.P. Yue, S.S. Wong, "On-chip spiral inductors with patterned ground shields for Si-based RF IC's," *IEEE J. Solid-State Circuits*, 33 (5), 1998, 743-752.

[8] J.Y.-C. Chang, A.A. Abidi, M. Gaitan, "Large suspended inductors on silicon and their use in a 2-µm CMOS RF amplifier," *IEEE Electron Device Letters*, 14, 1993, 246-248.

[9] Y. Sun, J.L. Tauritz, R.G.F. Baets, "Micromachined RF passive components and their applications in MMICs," *Int. J. RF and Microwave CAE*, 9, 1999, 310-325.

[10] A. Muller, G. Constantinidis, F. Giaccomozzi, et al., "Micromachined filters for 38 and 77 GHz supported on thin membranes," *J. Micromech. Microeng.*, 11 (4), 2001, 301-305.

[11] J.-B. Yoon, B.-I. Kim, Y.-S. Choi, E. Yoon, "3-D construction of monolithic passive components for RF and microwave Ics using thick-metal surface micromachining technology," *IEEE Trans. Microwave Theory and Techniques*, 51 (1), 2003, 279-288.

[12] G.W. Dahlmann, E.M. Yeatman, P. Young, I.D. Robertson, S. Lucyszyn, "High Q achieved in microwave inductors fabricated by parallel self-assembly," *Proc. Transducers '01*, Munich, Germany, June 10-14, 2001, 1098-1101.

[13] L.J. Fernandez, E. Berenschot, J. Sesé, R.J. Wiegerink, J. Flokstra, H.V. Jansen, and M. Elwenspoek, "Fabrication of thick silicon nitride blocks for integration of RF devices," *Electronics Letters*, 41, 3, 2005, p.124.

[14] J.G.E. Gardeniers, H.A.C. Tilmans, C.C.G. Visser, "LPCVD silicon-rich silicon nitride films for applications in micromechanics, studied with statistical experimental design," *J. Vac. Sci. Technol. A*, 14 (5), 1996.

[15] E. Sarajlic, E. Berenschot, G. Krijnen, M. Elwenspoek, "Versatile trench isolation technology for the fabrication of microactuators," *Microelectronic Engineering*, 67–68, 2003, 430–437.

Chapter 7

Conclusions

7.1 Introduction

In this thesis the research leading towards an RF MEMS power sensor has been presented. Various aspects of such a sensor have been addressed: starting with the basic theory in Chapter 2, the design in Chapter 3, fabrication issues in Chapter 4 and measurement results in Chapter 5. In Chapter 6 a promising alternative substrate was discussed. In this final chapter some conclusions will be presented.
Section 7.2 provides a summary of the thesis. Next, in Section 7.3 the most significant original contributions of this thesis are discussed. Finally, Section 7.4 gives some suggestions for future research.

7.2 Summary

Existing power sensors for RF signals are based on thermistors, diodes and thermocouples. These power sensors are used as terminating devices and therefore they dissipate the complete incoming signal. Furthermore, new telecommunication systems require low weight, volume and power consumption and a high level of integration with electronics. These requirements are expected to be fulfilled by RF MEMS devices. The design and fabrication of a power sensor for RF signals based on MEMS technology was the main objective of this thesis. The operation principle of the sensor is based on sensing the attractive force between the two plates of a charged capacitor, where one of the plates is moveable. Using this principle, fabrication of an RF power sensor with a large bandwidth (50 kHz - 40 GHz), large dynamic range (-60 dBm - +10 dBm) and very low transmission losses (<0.1 dB) is theoretically feasible. The research was performed in the

context of the European project “EMMA” (Electro Mechanical Microcomponents for precision Applications).

In Chapter 2, the impossibility to create a capacitive RF MEMS power sensor in a completely matched circuit was illustrated by proving the zero resulting force on a parallel-plate transmission line. Therefore, an RF power sensor based on the fabrication of a ‘bridge’ on top of a CPW was proposed. As a consequence, a capacitance discontinuity small enough to be treated as a lump element is created, where it can be considered that only the electrical force is felt. The ‘bridge’ is attracted towards the CPW placed below by a force proportional to the rms voltage of the RF signal squared. Thus, the power of the RF signal can be deduced by measuring the deflection of the beam capacitively. The increasing reflection losses as a function of the increasing sensor capacitance result in an inevitable trade-off between bandwidth and sensitivity. Nevertheless, a technique based on the redesign of the CPW dimensions can be used in order to retune the total impedance of the circuit and therefore increase its bandwidth.

In Chapter 3, the design of two different RF power sensors was presented: a) grounded sensor, b) floating sensor. The main difference between the two sensors (apart from the ‘bridge’ dimensions) is the electrical connection of the ‘bridge’, being directly connected to the ground lines of the CPW (grounded sensor) or completely floating, extending the ‘bridge’ over the entire CPW (floating sensor). Theoretical RF behavior of the sensor is calculated by modeling it by a shunt capacitor which capacitance is deduced by the geometrical dimensions of the ‘bridge’. It was found that sensor capacitance values lower than 80 fF are needed in order to fulfill the target specifications of the project (-26 dB reflection loss). Sensor designs with higher capacitance than required were chosen to ensure RF power detection for the case of grounded sensors. Nevertheless, better resolution for the deflection measurement of the ‘bridge’ can be obtained when a floating ‘bridge’ is used. Therefore, floating RF power sensors with capacitance low enough to fulfill target specifications were proposed. Furthermore, simulation results where CPW dimensions are changed in order to retune the circuit impedance show that the frequency range can be further extended, relieving the theoretical trade-off between RF and sensitivity performances.
The RF power sensitivity of the different sensors was also estimated by the calculation of the different spring constants of the ‘bridge’. A strong dependence between stress in the structural layer of the ‘bridge’ and sensitivity of the sensor was observed. Furthermore, capacitance change for each sensor at the maximum power level available on the setup used (0.08 Watt) was calculated, showing that lower stress values than 40 MPa are required.

The fabrication of the two different RF power sensors was described in Chapter 4. Aluminum surface micromachining on top of a glass substrate with photoresist as

a sacrificial layer was used for the fabrication of the sensors. The use of aluminum ensures good electrical properties for the fabrication of the CPW lines, while good mechanical properties can also be expected for the fabrication of the free standing 'bridge', since very small displacements are required (nm range). The glass substrate was chosen because of its good RF performance, and photoresist because of its round edges ensuring mechanical stability of the aluminum 'bridge'. Successful fabrication results of 300 μm long grounded bridges were reported, with a residual stress of 35 MPa. Nevertheless, a pattern on the structural layer of the 'bridge' was obtained, caused by the presence of the CPW lines below the sacrificial layer. Although no physical connection between the 'bridge' and the CPW was observed, the longer and more challenging designs of the floating 'bridge' required the development of a new process flow. In the new process, the transmission line is embedded into the wafer, and therefore, the 'bridge' fabrication is performed over a flat surface. Furthermore, no additional masks are needed because etching of the substrate is combined with the lift-off of the CPW lines. As a result of the news fabrication flow, the successful fabrication of very flat (200 nm height difference) 900 μm long aluminum bridges was reported

The characterization of the RF power sensors was presented in Chapter 5. The *S*-parameters measurement results on the grounded bridge sensor showed good agreement with respect to the theoretical expectations shown in Chapter 3. In the case of the floating bridge sensor, higher reflection losses than expected were measured due to the decrease of the gap distance between the bridge and the CPW lines (600 nm). Nevertheless, the use of different dimensions for the CPW in order to perform impedance compensation showed an improvement in the RF performance of the sensor. As a result, lower reflection losses than required from the target specifications (<-30 dB), and very low insertion losses (<0.14 dB) were obtained up to 4 GHz.
The power detection of an RF signal using a capacitive MEMS sensor is reported, creating for the first time a 'through' RF power sensor. Successful sensing of RF signals using the different RF MEMS power sensors was presented. Sensitivity in agreement with the theoretical expectations calculated in chapter 3 is found. The best sensitivity and resolution characteristics were obtained for the case of the 220x900 μm floating 'bridge', being 180.6 fF/W and 1 mWatt respectively.

A comparison of the measurement results obtained with the RF MEMS sensor (110x900 μm floating bridge with partly removed ground lines) with the target specifications and two different commercially available power sensors is presented in Table 7.1. As can be observed, the obtained power range is in the same order of magnitude as for commercially available RF power sensors, while the obtained frequency range is somewhat larger. The 'through' mode of sensing represents an important advantage with respect to the existing technologies. The price of the MEMS device is expected to be slightly higher than the commercial devices,

mostly because of the costs of packaging and the costs of the required readout electronics.

Parameter		**Target Specs.**	**Thesis Results**	**AD8361**	**Barry 16540**
Power	**Min.**	- 60 dBm	0 dBm	-20 dBm	+8 dBm
	Max.	+10 dBm	+24 dBm	+10 dBm	+33 dBm
	Range	70 dB	24 dB	30 dB	25 dB
Frequency Range		LF Device: 50 kHz – 4 GHz HF Device: 50 kHz – 40 GHz	>4 GHz	2.5 GHz	3 GHz
Insertion Loss		0.1 dB	0.14 dB (4GHz)	RF power lost during measurement	
Return Loss		26 dB (VSWR = 1.1)	30 dB (4GHz)		
Technology		MEMS 'Through' sensor	MEMS 'Through' sensor	HF RMS converted IC	Thick-film RMS sensor
Component Price			$9-11 end user (packaged)	$4	$5-10

Table 7.1: Comparison between target specifications stated at the beginning of the EMMA project, the measurement results from the RF MEMS power sensor presented in this thesis, and two commercially available RF power sensors.

In Chapter 6, the successful fabrication of two types of thick (tens of micrometers) SiRN blocks in highly-doped silicon wafers was presented: a) blocks with alternating plates of SiRN and Si, b) blocks completely made of SiRN. All different SiRN blocks were characterized by measuring the *S*-parameters of a CPW fabricated on top. Optimization of the RF performance for the case of alternating plates of SiRN and Si was obtained by increasing the SiRN plate width, and varying orientation of the plates with respect the CPW lines. As a result, 0.7 dB/mm insertion loss was measured at 4 GHz, which represent a large improvement in comparison to the 3.5 dB/mm measured for the case of low-resistivity silicon substrate. The best RF characteristics were obtained for the case of a 45 μm thick complete SiRN block, where 0.2 dB/mm insertion loss at 4 GHz was obtained, reaching very similar performances as dedicated glass substrates (0.1 dB/mm at 4 GHz).

7.3 Original contributions of this thesis

The original contributions presented by this thesis are summarized below:

- For the first time, a capacitive RF power sensor was designed and fabricated. The sensing is based on the detection of the Coulomb force acting on a moveable electrode due to the RF signal. The result is a 'through' RF power sensor which has not been reported earlier.

- Two techniques to improve the impedance matching of a CPW with sensor capacitance were successfully implemented. The techniques are based on changing the dimensions of the transmission line just before and after the sensor capacitance.

- A new fabrication process was proposed and tested for the fabrication of very flat aluminum membranes (200 nm height difference) suspended above a CPW. The process is based on embedding the CPW in the substrate, however no additional mask are needed because etching of the substrate is combined with the lift-off of the CPW lines.

- Thick (tens of micrometers) SiRN blocks were successfully fabricated in standard highly-doped silicon wafers making them suitable for use as low-loss RF substrates. The fabrication is based on two consecutive trench refilling steps by LPCVD SiRN.

- The performance of thick SiRN blocks as RF substrate was characterized by measuring the magnitude of the S_{11} and S_{21} parameters of CPW structures. It was shown that a performance very close to dedicated glass substrates (such an AF45) can be obtained.

7.3 Recommendations for future research

Another important aspect which needs further research is the implementation of a counter electrode for the bridge in order to be able to maintain it at the initial position. Typically, an additional electrode is realized at the other side of the moveable membrane. The voltage at this electrode is adjusted in a feedback loop in order to keep the membrane in its rest position. The required feedback voltage becomes a measure for the RF signal power. For the current prototype sensors, the additional electrode could be integrated on a separate wafer, which is bonded on top of the sensor wafer. A wafer bonding step is needed anyway for adequate packaging of the device.

Another way to realize feedback in the sensor is the inclusion of a piezoelectric material in the bridge in between two metal layers. In this way, the voltage applied between the metals would be used to keep the bridge at the initial position. A sensor design with piezoelectric layer in the bridge has already been made and fabrication has started. Nevertheless, due to fabrication delays, the results could not be presented in this thesis.

The good results obtained with SiRN blocks in highly doped silicon wafers as presented in Chapter 6 give some interesting possibilities for further research. First of all, the use of a silicon wafer instead of glass allows the possibility of using high temperature process steps, and therefore the use of better materials for the fabrication of the bridge, allowing lower stress values and the fabrication of weaker springs. Furthermore, the possibility of realizing CMOS electronics in the same wafer, and therefore, very close to the sensor, allows a significant improvement in resolution for the capacitance readout. Changes in the order of aF (10^{-18} F) could become detectable, improving the total resolution of the sensor by more than two orders of magnitude. Therefore, using a capacitive read-out, a resolution in the order of 10 μW should be feasible.

In order to push the power readout of the sensor to the theoretical limit, the detection of displacements in the order of pico-meters (10^{-12} m) will be needed. Transducers based on electron tunneling have already demonstrated the feasibility of resolutions in the order of 10^{-5} nm. Therefore, such readouts deserve further investigation. Furthermore, a readout based on electron tunneling does not exert an additional electrostatic force on the membrane, which is a fundamental drawback of capacitive readouts, especially in combination with low spring constants. However, the problems associated with the integration of an electron tunneling tip in a sensor structure should not be underestimated.

Any improvement in the detection of the bridge deflection can not only result in an improved sensor resolution, but it can also reduce the required sensor capacitance, which results in an increased frequency range.

APENDIX A: TARGET SPECIFICATIONS

The research presented in this thesis was performed within the EMMA (Electro Mechanical Micro-components for precision Applications) European project (http://www.vtt.fi/tte/research/tte7/research/emma/index.html). Although the fabrication of an RF power sensor is based on a completely new approach with respect to the existing technology, very ambitious target specifications were stated at the beginning of the project. Table A.1 presents the comparison between the target specifications stated in the EMMA project and two commercially available RF power sensors. As can be observed, it is requested to obtain very low losses (0.1 dB), and high frequency range (4 and 40 GHz) with respect to the existing devices. Furthermore, a huge increase in the power range is solicited, increasing from the 30 dB exhibited by the commercially available sensors up to 70 dB (10 mW nominal). In fact, the targets shown in table A.1 are based on the theoretical limits for the case of a MEMS based RF power sensor, and therefore, it could not surprise that those could not be reached during a 3 years project. Nevertheless, the target specifications give a very good illustration on what could be expected from this new approach for measuring RF power.

Parameter		**Target Specs.**	**AD8361**	**Barry 16540**
Power	**Min.**	- 60 dBm	-20 dBm	+8 dBm
	Max.	+10 dBm	+10 dBm	+33 dBm
	Range	70 dB	30 dB	25 dB
Frequency Range		LF Device: 50 kHz – 4 GHz HF Device: 50 kHz – 40 GHz	2.5 GHz	3 GHz
Insertion Loss		0.1 dB	RF power dissipated during measurement	
Return Loss		26 dB (VSWR = 1.1)		
Technology		MEMS ‘Through’ sensor	HF RMS converted IC	Thick-film RMS sensor
Component Price			$4	$5-10

Table A.1: Comparison between target specifications stated at the beginning of the EMMA project, compared to the specifications of two commercially available RF power sensors (AD8361 from ‘Analog Devices’, and Barry 16540 from ‘Barry industries’).

APENDIX B: DIELECTRIC LOSSES

When an electric field $\vec{E}$ is applied to a dielectric media, the polarization of the atoms or molecules of the material create electric dipole moments that augment the total displacement flux, $\vec{D}$. Therefore:

$$\vec{D} = \varepsilon_0 \vec{E} + \vec{P}_e \qquad (1)$$

Where $\vec{P}_e$ denotes the increase of the displacement flux by the polarization of the dielectric material. If we assume a linear medium, we can relate linearly the electric polarization with respect to the electric field applied:

$$\vec{P}_e = \varepsilon_0 \chi_e \vec{E} \qquad (2)$$

where χ_e is called the electric susceptibility, and might be a complex magnitude. In this way, total displacement flux can be written as:

$$\vec{D} = \varepsilon_0 \vec{E} + \vec{P}_e = \varepsilon_0 (1 + \chi_e)\vec{E} = \varepsilon \vec{E} \qquad (3)$$

where

$$\varepsilon = \varepsilon' - j\varepsilon'' = \varepsilon_0 (1 + \chi_e) \qquad (4)$$

is the complex permittivity of the medium. The imaginary part of ε represents the loss produced by the medium due to damping of the vibrating dipole moments. The loss of a dielectric material may also be considered as an equivalent conductor loss. In a material with conductivity σ, a conduction current density will exist:

$$\vec{J} = \sigma \vec{E} \qquad (5)$$

Now, Maxwell's curl equation for $\vec{H}$ can be transform is the following way:

$$\vec{\nabla} \times \vec{H} = j\omega \vec{D} + \vec{J} = j\omega \varepsilon \vec{E} + \sigma \vec{E} = j\omega \varepsilon' \vec{E} + (\omega \varepsilon'' + \sigma)\vec{E} = j\omega \left(\varepsilon' - j\varepsilon'' - j\frac{\sigma}{\omega} \right) \vec{E} \qquad (6)$$

Where it is seen that the loss due to dielectric damping ($\omega \varepsilon''$) is indistinguishable from conductivity loss (σ). The term $\omega \varepsilon'' + \sigma$ can then be considered as the total effective conductivity. A related quantity of interest is the loss tangent, defined as

$$\tan\delta = \frac{\omega\varepsilon'' + \sigma}{\omega\varepsilon'} \qquad (7)$$

The loss tangent can be seen as the ratio between the real and the imaginary part of the total displacement current. Microwave materials are usually characterized by specifying the real permittivity, $\varepsilon' = \varepsilon_r \varepsilon_0$, and the loss tangent at a certain frequency. It is useful to note that, after a problem has been solved assuming a lossless dielectric, loss can easily be introduced by replacing the real ε with a complex magnitude given by,

$$\varepsilon = \varepsilon' - j\varepsilon'' = \varepsilon'\left(1 - j\tan\delta\right) = \varepsilon_0\varepsilon_r\left(1 - j\tan\delta\right) \qquad (8)$$

SUMMARY

Existing power sensors for RF signals are based on thermistors, diodes and thermocouples. These power sensors are used as terminating devices and therefore they dissipate the complete incoming signal. Furthermore, new telecommunication systems require low weight, volume and power consumption and a high level of integration with electronics. These requirements are expected to be fulfilled by RF MEMS devices. The design and fabrication of a power sensor for RF signals based on MEMS technology was the main objective of this thesis. The research was performed in the context of the European project “EMMA” (Electro Mechanical Microcomponents for precision Applications).

In Chapter 2, the impossibility to create a capacitive RF MEMS power sensor in a completely matched circuit was illustrated by proving the zero resulting force on a parallel-plate transmission line. Therefore, an RF power sensor based on the fabrication of a ‘bridge’ on top of a CPW was proposed. The ‘bridge’ is attracted towards the CPW placed below by a force proportional to the rms voltage of the RF signal squared. Thus, the power of the RF signal can be deduced by measuring the deflection of the beam capacitively. The increasing reflection losses as a function of the increasing sensor capacitance result in an inevitable trade-off between bandwidth and sensitivity. Nevertheless, a technique based on the redesign of the CPW dimensions can be used in order to retune the total impedance of the circuit and therefore increase its bandwidth.

In Chapter 3, the design of two different RF power sensors was presented: a) grounded sensor, b) floating sensor. Theoretical RF behavior of the sensor is calculated by modeling it to a shunt capacitor. It was found that sensor capacitance values lower than 80 fF are needed in order to fulfill the target specifications of the project (-26 dB reflection loss). Furthermore, simulation results where CPW dimensions are changed in order to retune the circuit impedance show that the frequency range can be further extended, releasing the theoretical trade-off between RF and sensitivity performances.
The RF power sensitivity of the different sensors was also estimated by the calculation of the different spring constants of the ‘bridge’. A strong dependence between stress in the structural layer of the ‘bridge’ and sensitivity of the sensor was observed.

The fabrication of the two different RF power sensors was described in Chapter 4. Aluminum surface micromachining on top of a glass substrate with photoresist as a sacrificial layer was used for the fabrication of the sensors. The use of aluminum ensures good electrical properties for the fabrication of the CPW lines, while good mechanical properties can also be expected for the fabrication of the free standing

‘bridge’, since the strain is very small. The glass substrate was chosen because of its good RF performance, and photoresist because of its round edges ensuring mechanical stability of the aluminum ‘bridge’. Successful fabrication results of 300 μm long grounded bridges and 900 μm long floating bridges with embedded CPW lines were reported, with a residual stress of 35 MPa.

The characterization of the RF power sensors was presented in Chapter 5. The *S*-parameters measurement results on the grounded and floating bridge sensors showed good agreement with respect to the theoretical expectations shown in Chapter 3. The use of different dimensions for the CPW in order to perform impedance compensation showed an improvement in the RF performance of the sensor. As a result, lower reflection losses than required from the target specifications (<-30 dB), and very low insertion losses (<0.14 dB) were obtained up to 4 GHz.
The power detection of an RF signal using a capacitive MEMS sensor is reported, creating for the first time a ‘through’ RF power sensor. The best sensitivity and resolution characteristics were obtained for the case of the 220x900 μm floating ‘bridge’, being 180.6 fF/W and 1 mWatt respectively.

In Chapter 6, the successful fabrication of two types of thick (tens of micrometers) SiRN blocks in highly-doped silicon wafers was presented: a) blocks with alternating plates of SiRN and Si, b) blocks completely made of SiRN. All different SiRN blocks were characterized by measuring the *S*-parameters of a CPW fabricated on top. Optimization of the RF performance for the case of alternating plates of SiRN and Si was obtained by increasing the SiRN plate width, and varying orientation of the plates with respect the CPW lines. As a result, 0.7 dB/mm insertion loss was measured at 4 GHz, which represent a large improvement in comparison to the 3.5 dB/mm measured for the case of low-resistivity silicon substrate. The best RF characteristics were obtained for the case of a 45 μm thick complete SiRN block, where 0.2 dB/mm insertion loss at 4 GHz was obtained, reaching very similar performances as dedicated glass substrates (0.1 dB/mm at 4 GHz).

ACKNOWLEDGEMENTS

There are many people to thank for their support and encouragement, without which my Ph.D. at the University of Twente would have not been possible.

First and foremost I would like to thank my supervisors Jaap Flokstra and Remco Wiegerink for their enthusiastic guidance, insights and critical reviewing of my manuscripts and thesis. I am grateful to them for their encouragement and support during the thesis research and the granted freedom in conducting this work. Moreover, I would like to thank them for answering always with a 'yes' to my most common question: 'Do you have five minutes?'

I would like to acknowledge my promotor, Professor Miko Elwenspoek, for giving me the chance to join his group as a Ph.D. student, and for creating an inspiring and creative atmosphere within the group. I thank him for his confidence and trust.

I thank Henri Jansen for his brainstorm conversations, Erwin Berenschot, Meint de Boer and Rik de Boer for helping me with the technical development and microfabrication methods during my Ph.D. research, and Henk van Wolferen, Remco Sanders and Henk de Vries for their support during the building of different measuring set-ups.

A special thanks to Javier Sese, any challenge in the lab seems trivial when he is around. He was the perfect teacher, and I only hope I was a good learner.

Thanks to the staff in MESA + Lab, Eddy Ruiter, Peter Linders, Marion Groen, Huib van Vossen, Gerard Roefols, Samantha Geerdink, Hans Mertens, Bert Otter and Mark Smithers, who were very helpful during the fabrication.

A very important part of the research presented in this thesis was performed within the IST European project 'EMMA'. I would like to thank all participants: VTT, MIKES, PTB, VTI Hamlin and FLUKE. Special thanks to the coordinator, Heikki Seppä, who was the precursor of such ambitious research, to Anu Kärkkäinen for organizing and managing the EMMA project, and to Paul Roberts and Simon Hollingworth for helping with the packaging and interfacing of the sensor.

Part of the research realized during this period was performed at IMEC. I would like to thank Harrie Tilmans for giving me the opportunity to join his group during nine months. I would like to thank all the MCP division, and especially to Xavier Rottenberg for his help and friendship. I would also like to thank Gerg, Mikel, Bert, Raquel, Jose and Steve for the nice time we spent together in Leuven.

I thank all my colleges in the MICMEC group for a pleasant and enjoyable working environment: Alex, Boudewijn, Dannis, Deladi, Dennis, Dick, Doekle, Duy, Edin, Eelke, Edwin, Florian, Fran, Gijs, Hanh, Hans, Henk van Wolferen, Henk Wensink, Hien, Imran, Ingrid, Jeroen, John, Joost, Judith, Kees, Laura, Liesbeth, Marcel (who made the nice drawings for the front cover), Marco, Niels, Philip, Remco, Rik, Roald, Sandeep, Saravanan, Shanmugavel, Srinivas, Staya, Sim, Theo, Vitaly and Winfred. I would also like to thank the Low Temperature Group, and especially to Martin Van Essen.

I would like to thank Volker and Ellen for their friendship during these years. Gracias a toda la gente española que he conocido en Enschede: Adelio, Ana, Anuska, Astrid, Elena, Elisa, Fran, Gabriel, Gabrielle, Isabel, Javier O, Javier S, Jordi, Juan, Luis P, Maria, Miguel, Rogelio, Seve (te echamos de menos), Sheila, Sonia, Verena y Victor. Habeis sido como mi familia en Holanda, siempre dispuestos a una charla, a una fiesta de disfraces, a una cena, a un mus o lo que hiciera falta. Quiero agradecer de manera especial a Adelio, con quien pase momentos inolvidables. Gran parte de lo que aprendi durante este tiempo, y no esta escrito en este libro, lo aprendi a su lado.

Muchas gracias a los de Tarazona por recargarme las pilas en los veranos, y por ir a cenar al Visconti siempre que lo he pedido.

I wish to express my gratitude to my family-in-law, Antonio, Pili, Toño, Rosana, Manolo y Jana, for their understanding and support when we decided to come to Holland. “Gracias familia de Maella por hacerme sentir siempre a gusto en mis vacaciones, y por las chuletas de cordero y las longanizas”.

My most thanks words are for my parents, Luis y Maria Jose, my sister, Mariajo, my brother-in-law, Luis, my grandfather, Mariano and my grandmother, Josefina (te echo muchisimo de menos). “Gracias por vuestra paciencia y por estas siempre a mi lado dandome vuestro apoyo y cariño”. “Gracias Mariano por todas las cartas que me escribiste. Eres y seras siempre mi mejor amigo”.

Por ultimo, quiero agradecer a Marta su apoyo incondicional, que ha requerido sacrificios por su parte que siempre ofrecio sin dudar. Sin ti nunca hubiera podido afrontar estos años, a ti te lo debo y a ti te lo dedico. TE QUIERO.

BIOGRAPHY

Luis J. Fernandez received his M.Sc. degree in Physics in June 2001 from the University of Zaragoza, Spain. In October 2001 he got a scholarship for 6 months in the Low Temperature Group, MESA+ Institute for Nanotechnology, University of Twente, The Netherlands. In February 2002, he joined the Transducer Science Technology Group, MESA+ Research Institute, University of Twente, The Netherlands as Ph.D. student, working on the EU project EMMA (Electro Mechanical Microcomponents for precision Applications). From September 2004 to May 2005 he continued his work in IMEC, Belgium. Since November 2005 he is working in the Microsystems Group, Ikerlan, Spain.

LIST OF PUBLICATIONS

1) Luis J. Fernandez, Javier Sesé, Jaap Flokstra and Remco Wiegerink, "Capacitive MEMS application for high-frequency power sensor," *Proceedings of MME conference*, Sinaia, Romania, October 6-8, 2002.

2) L.J. Fernandez, E. Visser, J. Sesé, R.J. Wiegerink, H.V. Jansen, J. Flokstra, and M. Elwenspoek, "High frequency power sensor based on MEMS technology," *IEEE Sensors Conference*, Toronto, October 22-24, 2003.

3) Luis J. Fernández, Eelke Visser, Javier Sesé, Henry Jansen, Remco Wiegerink and Jaap Flokstra, "Novel rf power sensor based on capacitive MEMS technology," *Proceedings of MME conference*, Delft, The Netherlands, November 2-4, 2003.

4) J. Sese, L.J. Fernández, J.M. Reintsema, M.C. van Essen, R.J. Wiegerink, J. Flokstra, J.T.M. Beek, Th.G.S.M. Rijks, P.G. Steeneken, "Physics for stable capacitive MEMS-based devices," *FOM wetenschappelijke vergadering*, Veldhoven, The Netherlands, 2003.

5) L.J. Fernandez et al., "Development of a capacitive MEMS RF power sensor without dissipative losses: towards a new philosophy of RF power sensing," *CPEM 2004*, London, UK, June 27 - July 2, 2004.

6) L.J. Fernandez, J. Sesé, H.V. Jansen, R.J. Wiegerink, and J. Flokstra, "Optimization of a capacitive MEMS power sensor for radio frequency applications," *MME 2004*, Leuven, Belgium, September 5-7, 2004.3

7) M.C. van Essen, J. Sese, L.J. Fernández, J.M. Reintsema, R.J. Wiegerink, J. Flokstra, "Characterization of Capacitive MEMS at Cryogenic

Temperatures" *WOLTE-6 Sixth European Workshop on Low Temperature Electronics*, ESTEC, Noordwijk, The Netherlands, June 23-25, 2004.

8) M.C. van Essen, J. Sese, L.J. Fernández, J.M. Reintsema, R.J. Wiegerink, J. Flokstra, "Characterization of Capacitive MEMS at Cryogenic Temperatures," *MME 2004*, Leuven, Belgium, September 5-7, 2004.

9) L.J. Fernandez, J. Sesé, R.J. Wiegerink, J. Flokstra, H.V. Jansen, and M. Elwenspoek, "Radio frequency power sensor based on MEMS technology with ultra low losses," *MEMS-05*, Miami, Florida, Jan. 30 - Feb. 3, 2005.

10) L.J. Fernandez, E. Berenschot, J. Sesé, R.J. Wiegerink, J. Flokstra, H.V. Jansen, and M. Elwenspoek, "Fabrication of thick silicon nitride blocks for integration of RF devices," *Electronics Letters*, 41, 3, 2005, p.124.

11) L.J. Fernandez, U. Arz, D. Schubert, E. Berenschot, R. Wiegerink, J. Flookstra, ”A CMOS Compatible Process for Improved RF Performance on Highly Doped Subtrates,” *9th IEEE Workshop on Signal Propagation on Interconnects*, Proc.pp.167–170, May 10-13, 2005.

12) U. Arz, L.J. Fernandez, D. Schubert, E. Berenschot, R. Wiegerink, J. Flookstra, "Wideband Properties of Silicon Rich Nitride (SiRN)-based Transmission Lines," *in preparation for IEEE Microwave and Wireless Components Letters*.

13) L.J. Fernández, E. Berenschot, R. J. Wiegerink, J. Flokstra, H. V. Jansen and M. Elwenspoek, “Fabrication of thick silicon nitride blocks embedded in low-resistivity silicon substrates for radio frequency applications”, submitted to Journal of Micromechanics and Microengineering.

14) L.J. Fernández, J. Sesé, R. J. Wiegerink, J. Flokstra, H. V. Jansen and M. Elwenspoek, “A capacitive RF power sensor based on MEMS technology”, submitted to Journal of Micromechanics and Microengineering.